Changes of Fe precipitates by wire drawing in dilute Cu-Fe alloys

Kazuhiro Goto

Changes of Fe precipitates by wire drawing in dilute Cu-Fe alloys

（希薄 Cu-Fe 合金の線引き加工によって生じる Fe 析出物の変化）

Kazuhiro Goto

後藤　和宏

2023 年

CONTENTS

Chapter 1 Introduction

1.1. Research background

Copper is the most widely used element as a material for electrical wiring conductors and electrical connection terminals, and these industrial products are a necessary infrastructure for daily life that is utilized worldwide as power supply cables and information communication networks. Compared to other metallic elements, copper as a single element is the best in terms of strength, electrical resistivity, and manufacturing cost, which is the reason why copper is the most widely industrially used electrical wiring material.

In recent years, automatic door opening or closing, electric parking brake, and transmission shifters (so-called shift by wire) etc., have become increasingly computerized in order to improve the convenience of everyone using automobiles [1]. As the number of digitally operated electronic devices has increased, the corresponding number of switches and electronic sensors has also increased. Even if internal fuel combustion engines are replaced by fuel cells and rechargeable batteries, it is clear that the number of electronic devices will continue to increase in the future. For example, electric motors are essential for both electric and fuel cell vehicles, and electronic control sensors for them are also essential.

As the number of these vehicle-mounted electric wires, called wiring harnesses, increases, their volume and weight cannot be ignored. Figure 1.1 shows an example of an automotive wiring harness which is a complex assembly of very many parts such as metal wires, resin terminals and insulation coating of electric wires. Therefore, it is important to slim down the materials of wiring harness and reduce their weight for the future computerization of cars and improved comfort in human life. To slim them down, it is effective to make the cross-sectional area of the conductor material and the insulation coating as small as possible. Since electric wires account for 70% of the weight of the wiring harnesses [1], slimming down the conductor material is expected to have a significant effect not only on space saving but also on weight reduction. However, as the conductors become thinner, their load-bearing capacity decreases in proportion to their cross-sectional area. It is essential to develop the copper wires to achieve higher strength per unit area, since copper is the most popular conductor material. When increasing the strength of pure copper used for household indoor wiring, some well-known control methods of metallurgical structure, e.g. grain size refinement, optimization of crystal orientation and surface smoothness, are effective and have been already used for industrially mass-produced products. Although it is easy to increase the strength of pure copper up to about 500 MPa by work-hardening, the strength of pure copper is unsatisfactory for the future demand for wiring harnesses with thinner diameters and higher strength. The wiring harnesses

for automobiles come in a variety of shapes depending on the installation location [1], and accordingly, the specifications required for materials vary widely. If higher strength is required, the copper alloy with added elements may often easily achieve that goal. Figure 1.2 shows the properties of copper materials used in common wire and terminal products [2, 3, 4, 5]. The horizontal axis in Figure 1.2 is shown in unit of %IACS as an index of electrical conductivity to make the comparison with pure copper easier to understand. This unit named %IACS is the percentage of each material to pure copper (so-called International Annealed Copper Standard, of which electrical resistivity is 1.7241×10^{-8} Ωm). Cu-Sn, Cu-Mg and Cu-Ag alloys are mass-produced as train trolley wires. Cu-Zn, Cu-Ni_2Si, Cu-Fe-P and Cu-Be alloys are commercially available as thin sheet materials for electrical connection terminals. Including these, a large number of dilute copper alloys have been developed as materials for high-strength conductors. Generally, conductivity is tended to be sacrificed to achieve high strength in conductors for electrical connection terminals, but the balance of conductivity and strength is important in conductors for electric wires. By developing high-performance copper alloys, we can satisfy the growing demand for copper-based ultrafine wires required not only for wiring harnesses but also drones and wearable devices.

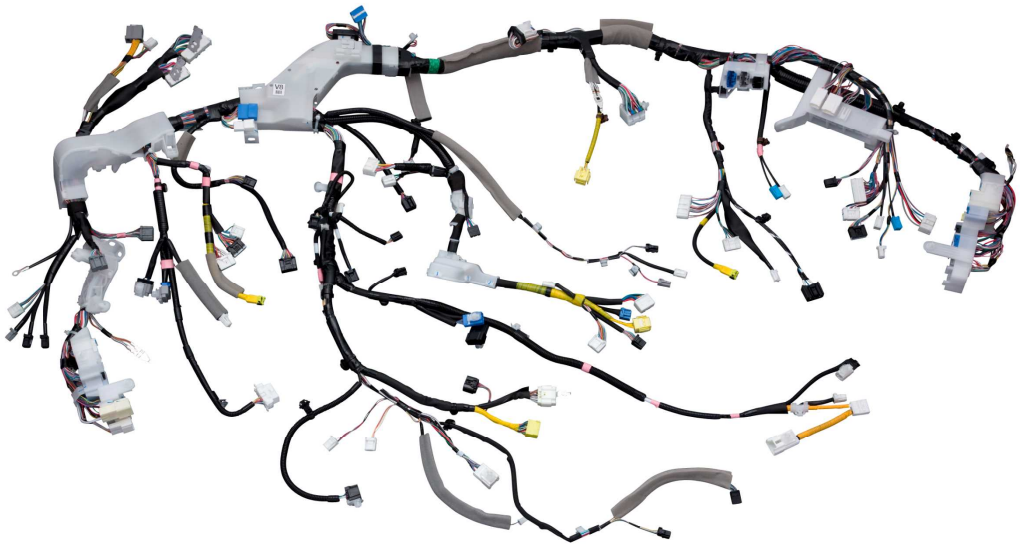

Figure 1.1 Example of an automotive wiring harness.

A wiring harness consists of electric wires, terminals, connectors, and cable ties.

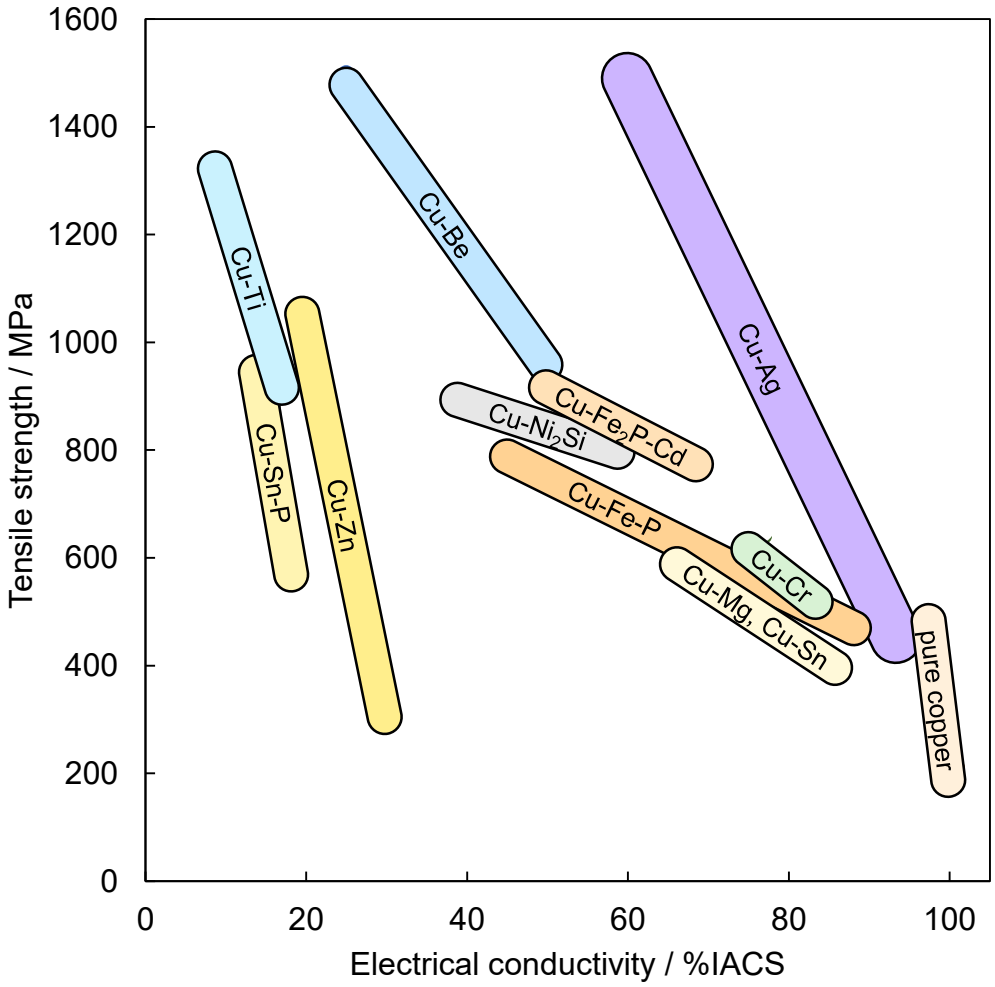

Figure 1.2 Typical copper alloys used for electric wires and electrical connection terminals. Horizontal axis is shown in unit of "%IACS" as an index of electrical conductivity. "%IACS" is the percentage of each material to pure copper (so-called International Annealed Copper Standard, of which electrical resistivity is 1.7241×10^{-8} Ωm).

1.2. Wire drawing as an essential process for electric wire manufacturing

A common and economical method suitable for the industrial mass production of copper alloy electric wires [6, 7] is shown in Figure 1.3. First, the base material with or without additive element is melted to obtain a large quantity and thickness of base metal by continuous casting. Next, plastic deformation is performed to the desired size, and once heat-treated to homogenize the metallic structure, further plastic deformation is performed to obtain the required diameter and shape as a product. Since the cross-sectional shape of almost all electric wire products is a circle, deforming methods that can produce a round cross-sectional shape are often employed. The most famous method is wire drawing using a cemented carbide die, which gradually thins the wire repeatedly through the die repeatedly, as shown in Figure 1.4. In the general wire drawing process, the cross-sectional area is reduced by 10% to 20% with each pass through the die, and the desired cross-sectional area is finally achieved by very many repeated passes through the dies. So, wire drawing is a historical method that has been used for centuries as the best method for making wire products, and in recent years there have been many reports of its application in materials research such as a method for generating severe plastic deformation [8, 9]. For example, it is easy to deform a pure copper wire from a diameter of 8 mm or more to a diameter of 0.1 mm or less without fracturing [10]. However, it has been reported for a very long time that there is a large increase in electrical resistivity [11, 12] when certain copper alloys are subjected to plastic deformation.

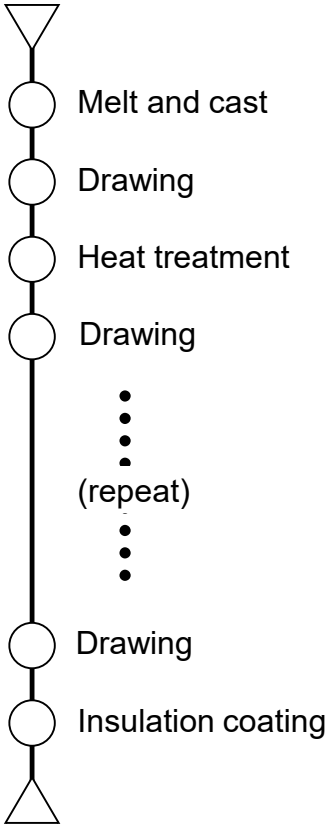

Figure 1.3 Typical wire manufacturing process flow.

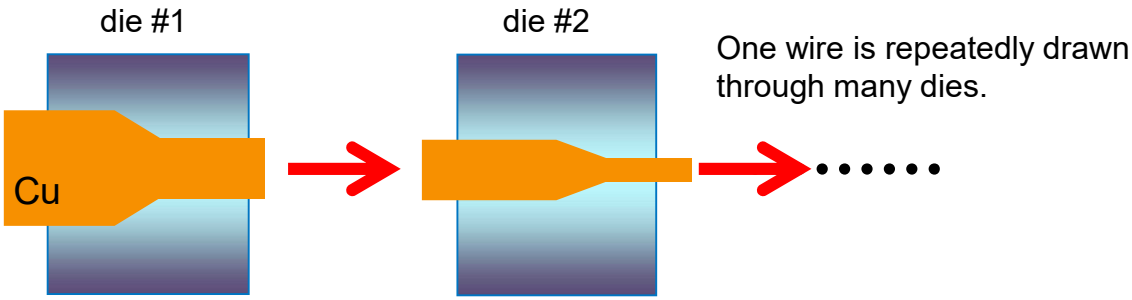

Figure 1.4 Schematic illustration of wire drawing by several dies.

1.3. Material property changes of Cu-Fe alloys by aging precipitation and deformation

Although Cu-Fe binary alloys are minor for wire applications, there have been many studies on this alloy for a long time, and Boltax had pointed out the anomalous increase [12] in electrical resistivity of the Cu-1.5 at% Fe alloys which had been subjected to plastic deformation by cold working. To lower the electrical resistivity is very important for electric wire products, and since such a large plastic deformation is unavoidable during the wire drawing as industrially common-used manufacturing process, it is very important to understand the reason why such electrical resistivity changes occur and to obtain guidelines for optimizing wire manufacturing conditions.

Historically, many works have been reported on characterization of dilute Cu-Fe alloys to reveal the behavior of aging precipitation after annealing [13, 14, 15]. Although the Cu-Fe alloys did not harden as intensely as the Al-Cu alloys known as duralumin [16, 17, 18], several earlier research reports have focused discussions on changes in magnetic properties before and after plastic deforming [13, 19, 20]. There were few reports on electrical resistivity changes[12, 21], and many of the studies newer than the 1950s were concerned with the size and phase transformation of Fe precipitates or the interface consistency between Fe and the Cu matrix phase [22, 23, 24]. Several analytical methods such as transmission electron microscopy (TEM) [25, 26, 27, 28], X-Ray diffraction (XRD) [29, 30, 31] and ^{57}Fe-Mössbauer spectroscopy [32, 33, 34, 35] were used to characterize Fe precipitates. Depending on annealing conditions, both α-Fe (BCC) and γ-Fe (FCC) precipitates were found to appear, and γ-Fe precipitates were usually formed coherently to the Cu-matrix. Magnetic property measurements and in-situ TEM observations revealed that γ-Fe precipitates undergo martensitic transformation to α-Fe phase by cold working [36]. In the dilute Cu-Fe alloys after aging heat treatment, Fe atoms are present in three types of states, i.e., substitutional solute in Cu (FCC) as denoted by Cu(Fe) in this thesis, α-Fe and γ-Fe. There are several factors affecting electrical resistivity, such as plastic strain, amount of added elements, and the amount of Cu(Fe). Although it is generally known that the effect of solid solution on electrical resistivity in pure copper is much larger than other factors, there are few reports that focus on the amount of Cu(Fe). In a prior research report, efforts have been made to extract precipitated Fe particles and estimate the amount of Cu(Fe) [37, 38]. As far as the author has been able to find, there are no studies reporting a causal relationship between the amount of wire drawing and the amount of Cu(Fe). In the past, there have already been experimental methods available to analyze Fe solid solubility in Cu, and in the last two decades, state-of-the-art analytical methods have become accessible. For example, a three-dimensional atom probe tomography (3D-APT),

which is an instrument for visualizing atomic-level information, is now widely available. And also even either of experimental facilities using neutron beams and synchrotron radiation facilities are becoming increasingly easily accessible to private sector in Japan. Furthermore, there are several private companies building and operating beamlines in synchrotron radiation facilities [39, 40, 41]. Recent years, X-ray absorption fine structure (XAFS) performed by synchrotron radiation have been used to identify the local environment of the precipitates in metallic alloys [42, 43, 44]. For example, Yaguchi *et al*. reported the presence of two types (FCC and BCC) of Cu in Fe matrix by XAFS measurement and theoretical calculation [42]. However, to the authors' best knowledge, there have been no XAFS studies of Fe in Cu matrix considering Cu(Fe), α-Fe and γ-Fe. Thus, I thought now would be a good time to use these advanced analytical methods, as well as conventional ones, to clarify the relationship between electrical resistivity and the degree of plastic deformation by the wire drawing process.

1.4. Purpose of this research

With these backgrounds, the author of this thesis first made a prototype of a dilute Cu-Fe alloy to investigate the large increase in electrical resistivity caused by wire drawing. Besides electrical resistivity, mechanical and magnetic properties were also investigated to study age hardening and martensitic transformation. Next, several analytical methods were subjected to find out the factors that caused such an anomalous change in electrical resistivity. Along with laboratory instruments that provide a narrow analytical field of view with high spatial resolution, other analytical methods using neutron beams and synchrotron radiation X-rays with a wide analytical field of view have been applied. Finally, first-principles calculations were performed to consider about theoretical support for the experimental XANES.

1.5. Structure of this thesis

This thesis consists of five chapters.

In chapter 1 (this chapter), the background and objectives of this research is described.

In chapter 2, the details of finding critical aging and wire drawing conditions for dilute Cu-Fe alloys to cause a large increase in electrical resistivity is investigated. In addition to the electrical properties, mechanical and magnetic properties were also evaluated.

In chapter 3, the results of five different analytical methods performed to characterize Fe precipitates in Cu-Fe ultrafine wires are described. XRD measurements and TEM observations were performed to determine whether the α-Fe phase can be detected or not, focusing on the Cu-Fe wires whose electrical resistivity has increased after aging followed by wire drawing. The shape of the Fe precipitates and the distribution of Fe concentration after wire drawing was confirmed using 3D-APT analysis at the atomic level. The size of the Fe precipitates was investigated using Small Angle Neutron Scattering (SANS) techniques comparing with the result of TEM observation. In addition, the author attempted to clarify the causal relationship between the amount of substituted solute Fe in Cu (namely Cu(Fe) in this thesis) and the degree of wire drawing by using XAFS.

In chapter 4, the author attempted to simulate the XAFS spectra using the Density Functional Theory (DFT) calculations and then compared the calculated transition energies with the measured photon energies.

In chapter 5, the given insight through this research will be summarized.

References

[1] *Materia Japan,* **60** (12), 769 (2021).

[2] K. Nomura, *Kobe Steel Eng. Rep*., **71** (2), 29 (2022).

[3] Y. Aruga *et al., Materia Japan*, **47**(1), 33 (2008).

[4] Y. Sakai *et al., Acta Metall. Mater*., **43** (4), (1995).

[5] T. Kuroyanagi *J. JILM*, **37** (4), 313 (1987).

[6] K. Murata and K. Sawada, *J. Japan Inst. Metals*, **21** (12), 980 (1982).

[7] S. Aoyama *et al., J. Japan Inst. Metals*, **51** (9), 858 (1987).

[8] G. Faraji and H. Torabzadeh, *Mater. Trans*., **60** (7), 1316 (2019).

[9] A. Zavdoveev *et al., Steel Res. Int*., **92** (3), 2000482 (2020).

[10] S. Aoyama, *Materia Japan,* **51** (6), 251 (2012).

[11] O. Izumi, *J. Japan Inst. Metals*, **4** (2), 101 (1965).

[12] A. Boltax, *Trans. Met. Soc. AIME,* **224**, 281 (1962).

[13] F. Bitter and A. R. Kaufmann, *Phys. Rev*., **56**, 1044 (1939).

[14] J. Reekie *et al., Proc. Phys. Soc. B,* **66**, 1101 (1953).

[15] A. Boltax, *Trans. Met. Soc. AIME,* **218**, 812 (1960).

[16] M. Cohen, *Trans. AIME,* **95**, 133 (1939).

[17] R. B. Gordon and M. Cohen*, ASM Symposium on Age Hardening of Metals*, 161 (1940).

[18] C. S. Smith, *Progress in Metal Physics,* **1**, 175 (1949).

[19] C. S. Smith, *Phys. Rev.,* **57**, 337 (1940).

[20] C. S. Smith, *Progress in Metal Physics,* **1**, 212 (1949).

[21] S. Nishikawa *et al., Seisan-Kenkyu*, **18** (11), 312 (1966).

[22] K. E. Easterling and H. M. Miekk-Oja, *Acta Metall.,* **15** (7), 1133 (1967).

[23] K. E. Easterling and G. C. Weatherly, *Acta Metall.,* **17** (7), 845 (1969).

[24] Y. Watanabe *et al., J. Mater. Sci.,* **26**, 4307 (1991).

[25] G. Mima *et al., J. Japan Inst. Metals*, 33, 521 (1969).

[26] S. Saji *et al., Trans. JIM,* **14** (1), 82 (1973).

[27] H. Kubo *et al., Met. Sci*., **9** (1), 61 (1975).

[28] M. Kato *et al., J. Japan Inst. Metals*, **56** (8), 865 (1992).

[29] J. M. Denney, *Acta Metall.,* **4** (6), 586 (1956).

[30] J. Eckert *et al., J. Appl. Phys*., **73** (1), 131 (1993).

[31] O. E. Aguero *et al., J. metastable nanocryst. mater*., **20-21**, 648 (2004).

[32] T. J. Panek and J. Kansy, *J. Phys. F,* **12**, 269 (1982).

[33] K. Sumiyama *et al., Trans. JIM*., **26** (4), 217 (1985).

[34] K. Sumiyama *et al., Nucl. Instrum. Methods Phys. Res. B,* **76** (1), 33 (1993).

[35] E. A. Shafranovsky *et al., J. Nanopart. Res.,* **13**, 4913 (2011).

[36] N. Ishikawa and A. Sato, *Philos. Mag. A*, **64** (2), 387 (1991).

[37] Y. Aruga *et al., Journal of Japan Research Institute for Advanced Copper-base Materials and Technologies,* **43**, 74 (2004).

[38] Y. Aruga *et al., Materia Japan,* **45** (1), 51 (2006).

[39] Y. Hirose *et al., SPring-8/SACLA Res. Rep.,* **14** (1), 40 (2009).

[40] M. Hosaka *et al., Kasokuki,* **13** (1), 18 (2016).

[41] K. Yamaguchi *et al., SEI Tech. Rev.,* **86**, 131 (2018).

[42] H. Yaguchi *et al., TETSU TO HAGANE,* **94** (3), 86 (2008).

[43] M. Nagoshi *et al., ISIJ Int.,* **53** (12), 2197 (2013).

[44] M. Tada *et al., TETSU TO HAGANE,* **100** (12), 1530 (2014).

Chapter 2 Property changes in dilute Cu-Fe alloys by wire drawing

2.1. Introduction

In this chapter, we focus on dilute Cu-Fe alloys and investigate the conditions under which a large increase in electrical resistivity was caused by wire drawing after aging heat treatment, and how the mechanical and magnetic properties change at different degrees of plastic deformation.

The Fe composition was 0.53 at%, which is equal to 0.60 mass%.

First, a prototype Cu-Fe alloy was tested with a focus on whether this alloy could exceed 500 MPa, i.e. over the upper limit of pure copper, and whether it would not fracture even when drawn to ultrafine wires with a diameter of 0.05 mm. Next, the property changes that occur when the wires had been drawn down to 0.05 mm after intermediate heat treatment at 5.8 mm were investigated.

It was expected that aging precipitation of Fe might undergo during intermediate heat treatment and that Fe precipitates would change after wire drawing. Therefore, three types of property evaluations were conducted with wire diameters ranging from 5.8 mm to 0.05 mm. Since wire drawing process requires the use of many dies, as shown in Figure 1.4, the same dies were used to reduce variation among the prototype samples. All dies were made according to the American Wire Gauge (AWG) standard.

Although it has already been reported that dilute copper alloys such as Cu-Co [1, 2, 3, 4] or Cu-Cr [5, 6, 7, 8, 9, 10, 11] , as well as Cu-Fe [12, 13, 14, 15, 16] alloys, may exhibit various property changes by aging precipitation and cold working, only Cu-Fe alloy was investigated in this study. Since iron is more abundant and lower manufacturing costs than cobalt and chromium, this copper-iron alloy would be suitable for future mass production.

2.2. Experimental procedure

Dilute Cu-Fe alloys were prepared according to the flow shown in Figure 2.1. First, the raw materials (Cu and Fe) were melted down and their composition was adjusted, and then a continuous melting and casting process was used to form rods with a diameter of 12.5 mm. The diameter was then reduced to 5.8 mm, followed by heat treatment and further deformed to obtain ultrafine wire with a minimum diameter of 0.05 mm. There are several methods of plastic deforming, including wire drawing, swaging, rolling, and extrusion. If the wire drawing methods were different, there is a concern that material properties would be affected due to the radial distribution change of dislocations accumulation and crystal orientations (these are so-called "deformation texture"). Therefore, in this study, we designed the wire drawing conditions to be the same, such as ambient temperature, lubricant, die, and drawing speed, after aging heat treatment at 5.8 mm in diameter. However, rotary swaging was applied when the diameter was larger than 5.8 mm. When the diameter was smaller than 5.8 mm, the dies according to the AWG standard were used to make the Cu-Fe wires thinner. The drawn wires to be investigated were chosen as the gauge numbers of AWG3, AWG10, AWG19, AWG28, AWG38 and AWG 44. These six dies are corresponding to approximately 5.8 mm, 2.6 mm, 0.9 mm, 0.32 mm, 0.10 mm and 0.05 mm in the wire diameter.

In this thesis, working ratio η is used for convenience. The working ratio η is defined according to the following equation (2.1), where assuming that the cross-sectional area of the as-cast or annealed wire is defined as S_0 and the cross-sectional area of a drawn wire is defined as S_1.

$$\eta = \ln\left(\frac{S_0}{S_1}\right) \qquad \text{Equation (2.1)}$$

For example, an aging heat-treated wire was drawn from a maximum diameter of 5.8 mm (η = 0.0) to a minimum diameter of 0.05 mm (η = 9.5). On the other hand, the non-aged one was swaged and drawn from a diameter of 12.5 mm (η = 0.0) to a diameter of 0.05 mm (η = 11). Table 2.1 shows the sample information including the aging temperature and the working ratio η, with showing three methods for material characterization which was performed in order to reveal the property changes caused by aging or wire drawing.

The composition of the Cu-Fe alloy was examined by inductively coupled plasma atomic emission spectroscopy (ICP-AES). As shown in Table 2.2, the amount of Fe was confirmed to be 0.53 at%, and the other three elements P, S and C which should be checked as impurities, were estimated to be less than 0.01 at%.

A double-bridge instrument was used to measure electrical resistivity at 293 K. The length of each sample was 350 mm or longer. As shown in Figure 2.2, current was applied from both ends of each sample, and two knife-edge tips connected to ohmmeter were placed inside them. The length between the knife-edge electrodes was set to be 300 mm.

The tensile strength of each Cu-Fe wire were tested at 293 K using a universal testing machine Autograph AG-5000D (Shimadzu, Japan). The gauge length of the tensile test sample was 250 mm, and the strain rate was 2.5 mm/s.

Magnetic properties were measured using a vibrating sample magnetometer (VSM), BHV-50H (Riken Denshi, Japan) and B-H curves were obtained. Each Cu-Fe wire was cut to a weight between 0.1 g and 0.3 g, electrolytic Ni (saturation magnetization of 0.61 T) weighing 0.1 g was measured as a standard sample, and the magnetization of each sample was calculated. As shown in Figure 2.3, the measurement was performed so that the direction of the applied magnetic field and the longitudinal direction of each Cu-Fe wire were parallel.

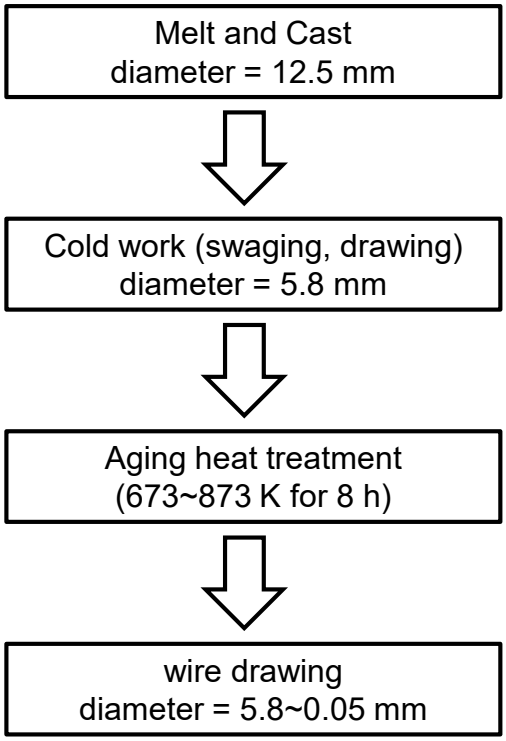

Figure 2.1 Sample preparation flow.

Table 2.1 List of sample information and examined properties.

Sample and process information				Material properties (○ : examined, - : not examined)		
Sample name	Wire diameter	Aging temperature	Working ratio η	Tensile strength	Electrical resistivity	Magnetization
A0	12.5 mm	not aged	0.0	-	-	-
A1	5.8 mm	not aged	1.5	○	○	○
A2	2.6 mm	not aged	3.2	○	○	○
A3	0.90 mm	not aged	5.3	○	○	○
A4	0.32 mm	not aged	7.3	○	○	○
A5	0.10 mm	not aged	9.7	○	○	-
A6	0.05 mm	not aged	11	○	○	-
B0	5.8 mm	673 K	0.0	○	○	○
B1	2.6 mm	673 K	1.6	○	○	○
B2	0.90 mm	673 K	3.7	○	○	○
B3	0.32 mm	673 K	5.8	○	○	○
B4	0.10 mm	673 K	8.1	○	○	-
B5	0.05 mm	673 K	9.5	○	○	-
C0	5.8 mm	773 K	0.0	○	○	○
C1	2.6 mm	773 K	1.6	○	○	○
C2	0.90 mm	773 K	3.7	○	○	○
C3	0.32 mm	773 K	5.8	○	○	○
C4	0.10 mm	773 K	8.1	○	○	-
C5	0.05 mm	773 K	9.5	○	○	-
D0	5.8 mm	873 K	0.0	○	○	○
D1	2.6 mm	873 K	1.6	○	○	○
D2	0.90 mm	873 K	3.7	○	○	○
D3	0.32 mm	873 K	5.8	○	○	○
D4	0.10 mm	873 K	8.1	○	○	-
D5	0.05 mm	873 K	9.5	○	○	-
E0	5.8 mm	723 K	0.0	○	○	-
F0	5.8 mm	823 K	0.0	○	○	-

Table 2.2 Composition of prepared Cu-Fe alloy by ICP-AES.

Element	Composition (at%)
Fe	0.53
P	< 0.01
S	< 0.01
C	< 0.01
Cu	Bal.

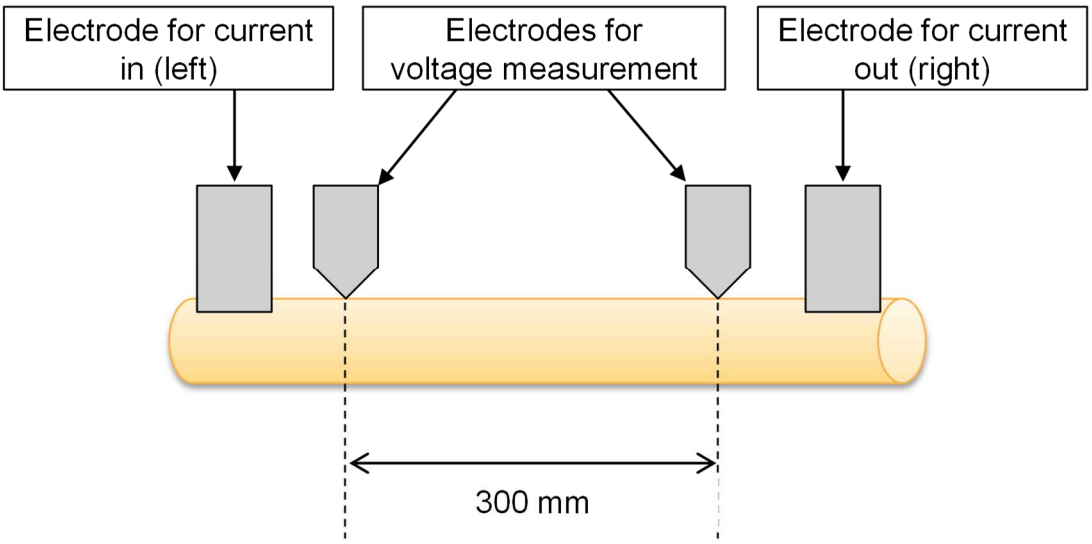

Figure 2.2 Schematic diagram of electric resistivity measurement.

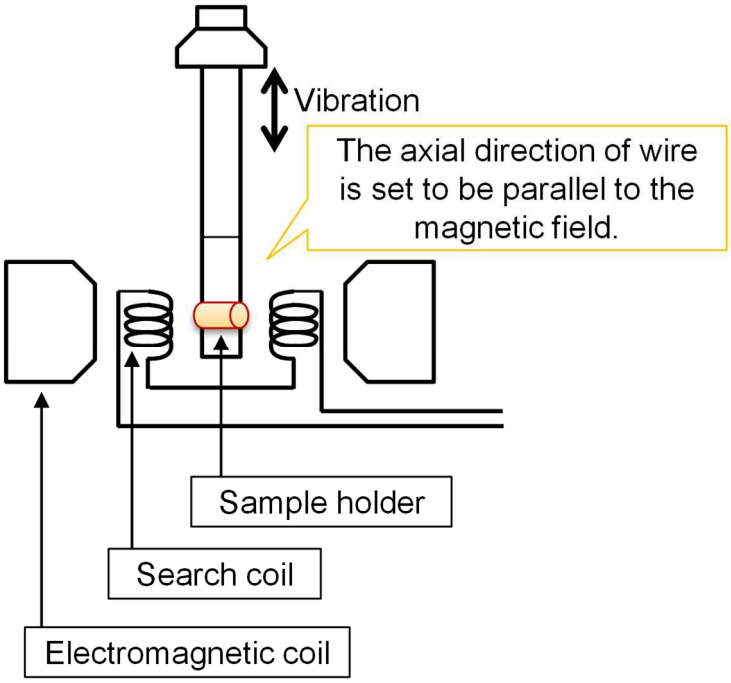

Figure 2.3 Schematic diagram of VSM measurement system. [17]

2.3. Results and discussion

2.3.1. Electrical and mechanical properties of Cu-Fe alloys before wire drawing

Figure 2.4 shows the electrical resistivity and mechanical properties of a heat-treated wire with a diameter of 5.8 mm. After annealing for 8 hours, electrical resistivity reached a minimum value at 773 K, and Both tensile strength and yield strength gradually decreased from 673 K to 873 K. Sample C0 (773 K) with the lowest electrical resistivity, sample D0 (873 K) with the lowest tensile strength, and sample B0 (673 K) with the highest tensile strength were selected as the starting materials for wire drawing from 5.8 mm to 0.05 mm diameter.

By examining how the electrical resistivity of these three samples increases before and after wire drawing, it should be possible to determine the conditions under which a large electrical resistivity increase occurs. The changes in mechanical or magnetic properties as well as the increase in electrical resistivity due to the wire drawing process will be discussed in the next and subsequent sections.

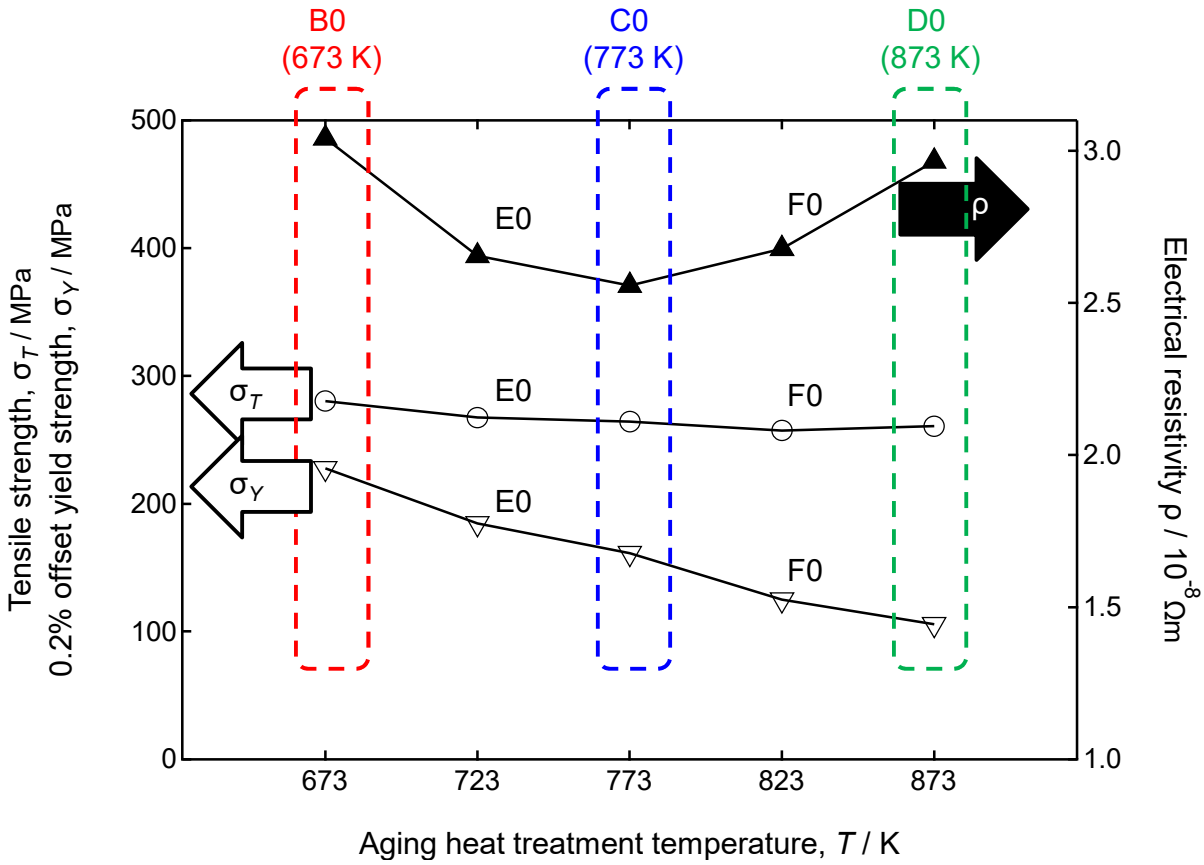

Figure 2.4 Mechanical properties and electrical resistivity of Cu-Fe wires after aging heat treatment for 8h at 5.8 mm diameter.

2.3.2. Mechanical properties of Cu-Fe alloys after wire drawing

Figure 2.5(a) and (b) show the results of tensile strength and electric resistivity, respectively .The non-aged wires (A1~A6) and the aged wires (B0~B5, C0~C5, and D0~D5) showed clearly different trend in the correlation between the tensile strength and the working ratio η. One possible reason for this difference is that the forging process is included in addition to the wire drawing process when deforming from A0 (η = 0.0) to A1 (η = 1.5). Then, in terms of work hardening, the forging process is considered to have a lower effect than the wire drawing process. In contrast, there was little difference among the B, C, and D series, and the tensile strength increased monotonically with the same trend from η of 1.6 to 9.5. This indicates that the tensile strength of this Cu-0.53 at% Fe alloy after only wire drawing is dominated by work hardening, which is proportional to the working ratio η. In other words, it is indicated that the mechanical properties of this alloy are dominantly affected by the effect of grain refinement, known as the Hall-Petch relationship, and the effect of increased crystal defects, such as dislocations. Wires aged at 873 K showed slightly higher tensile strength in the η range of 1.6~5.8 than the others, suggesting that this slight difference is due to the weak precipitation strengthening effect of Fe, since Cu-Fe alloy were known to have a little age-hardenability in a previous study [18]. Whereas, there was little discrepancy in tensile strength between the different aging temperatures in the range of η above 8.1. Therefore, it is possible that Fe precipitates have become smaller by wire drawing, and the effect of precipitation strengthening has disappeared. Nevertheless, the tensile strength of the ultrafine wire still reached around 700 MPa.

In addition to the results above, it has also been found that this Cu-0.53 at% Fe alloy could be easily obtained ultrafine wire in a diameter of 0.05 mm (named A6 in Figure 2.5(a)) without fracturing. This wire drawability is as good as that of pure copper ultrafine wire [19] described in the section 1.2 The fact that a dilute Cu-Fe alloy wire can be drawn to ultrafine wire with a small number of intermediate heat treatment is a very significant advantage in terms of mass production capability.

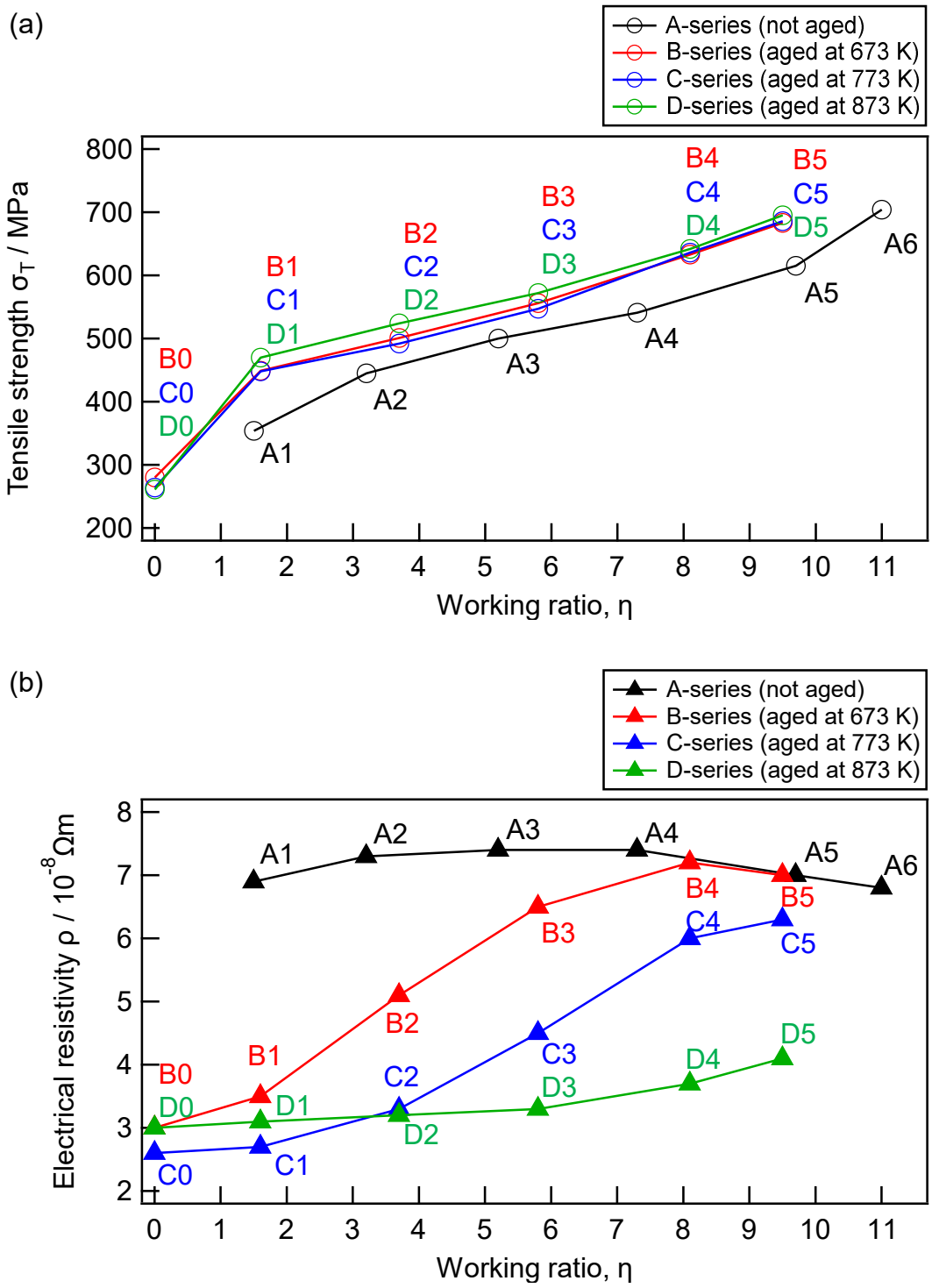

Figure 2.5 Mechanical properties and electrical resistivity of Cu-Fe wires before and after wire drawing.

(a) Tensile strength of Cu-Fe wires. (b) Electrical resistivity of Cu-Fe wires.

2.3.3. Electrical resistivity evaluation of Cu-Fe alloys after wire drawing

As already shown in Figure 2.5(b), a large difference in electrical resistivity due to wire drawing was observed depending on aging heat treatment temperature. In particular, the comparison between the wires C0 and C5 showed a huge increase in electric resistivity by a factor of 2.5. Not only the wires C0~C5 (aged at 773 K) but also the wires B0~B5 (aged at 673 K) showed a large increase in resistivity as the working ratio η increased by a factor of 2.3. In contrast, the wires D0~D5 (aged at 873 K) showed only a slight increase in electrical resistivity by a factor of 1.4. This difference in the degree of increase in electrical resistivity is very similar to the phenomenon pointed out in the early studies [16, 20, 21] in 1960s.

A comparison of the B, C, and D series shows that there is a fairly large increase in electrical resistivity despite the little difference in tensile strength. First, considering the relationship between the working ratio η and tensile strength, as discussed in section 2.3.2, the work hardening of the Cu matrix including Fe as solute atom may be dominant, and the solid solution Fe amount or Fe precipitates themselves have little effect on tensile strength. Next, considering the relationship between the working ratio η and electrical resistivity, old studies have shown that a very small amount of solid solution Fe can significantly increase electrical resistivity of Cu matrix. If the solute atoms are homogeneously distributed in the matrix, the amount of solid solution Fe can be estimated according to a known experimental equations. Specifically, the following equation (2.2) with an experimental constant parameter Δρ [22] is useful for estimation, where ρ_{expt} is the measured electrical resistivity, ρ_0 is the electrical resistivity of pure Cu and C_{sol} is the amount of solid solution Fe.

$$\rho_{expt} = \rho_0 + C_{sol} \cdot \Delta\rho \qquad \text{Equation (2.2)}$$

Note, that this equation (2.2) is an experimental equation for the range of C_{sol} from 0.075 to 0.87 at%, and the Cu-0.53 at% Fe in this case is within this range. A linear relationship between the mass of solute atom and electrical resistivity has been reported for many types of solute atoms [22].

Table 2.3 shows the obtained C_{sol} of Cu-Fe wires according to the equation (2.2), and C_{sol} increases up to around 0.53 at% together with working ratio η in B and C series. The phenomenon of increased solid solution due to cold working had been predicted in the previous study of Boltax [16] who proposed the hypothesis that coherent Fe particles on the Cu slip plane could be fragmented and reduced in size by dislocation migration. It was also argued that the fragmented Fe atoms could become too small and behave like solute atoms to be able to induce anomalous scattering of electrons, resulting in an increase in the electrical resistivity.

Similar phenomena to this previous study can be assumed to have occurred inside the Cu-Fe wire when the isothermal aging temperatures were 673 K and 773 K, but quite different behavior was observed when the wire was aged at 873 K. Although there have been old experimental reports focusing on the effect of aging temperature on electrical resistivity after cold working [16, 20, 21], no report has clarified the phenomenon using an analytical method with atomic-level spatial resolution, and the details are still unknown. From a different point of view, several earlier reports based on magnetic property [23] and TEM observation [24, 25] confirmed that the γ-Fe precipitates coarsened by aging heat treatment might undergo martensitic transformation to α-Fe by plastic deformation at low temperature. Additional discussion is provided in the next section based on magnetic properties since the amount of α-Fe cannot be predicted based on strength and electrical resistivity on their own.

Table 2.3 Measured electrical resistivity and calculated concentration of solid solution.

Sample and process information				Results of characterization	
Sample name	Wire diameter	Aging temperature	Working ratio η	Measured resistivity ρ_{expt} ($\times 10^{-8}$ Ωm)	Concentration of solute , C_{sol} (at%)
A1	5.8 mm	not aged	1.5	6.9	0.49
A2	2.6 mm	not aged	3.2	7.3	0.53
A3	0.90 mm	not aged	5.3	7.4	0.54
A4	0.32 mm	not aged	7.3	7.4	0.54
A5	0.10 mm	not aged	9.7	7.0	0.50
A6	0.05 mm	not aged	11	6.8	0.48
B0	5.8 mm	673 K	0.0	3.0	0.12
B1	2.6 mm	673 K	1.6	3.5	0.17
B2	0.90 mm	673 K	3.7	5.1	0.32
B3	0.32 mm	673 K	5.8	6.5	0.45
B4	0.10 mm	673 K	8.1	7.2	0.52
B5	0.05 mm	673 K	9.5	7.0	0.50
C0	5.8 mm	773 K	0.0	2.6	0.08
C1	2.6 mm	773 K	1.6	2.7	0.09
C2	0.90 mm	773 K	3.7	3.3	0.15
C3	0.32 mm	773 K	5.8	4.5	0.26
C4	0.10 mm	773 K	8.1	6.0	0.40
C5	0.05 mm	773 K	9.5	6.3	0.43
D0	5.8 mm	873 K	0.0	3.0	0.12
D1	2.6 mm	873 K	1.6	3.1	0.13
D2	0.90 mm	873 K	3.7	3.2	0.14
D3	0.32 mm	873 K	5.8	3.3	0.15
D4	0.10 mm	873 K	8.1	3.7	0.19
D5	0.05 mm	873 K	9.5	4.1	0.22

2.3.4. Change in magnetization after wire drawing

Figure 2.6 shows the changes in magnetic properties obtained by VSM for the Cu-Fe alloys, which is indicating that the magnetization increased as η increased from 0 to 1.6. Since Cu is a nonmagnetic element, the increase in magnetization indicates that α-Fe precipitates increased by the wire drawing from 5.8 mm (η = 0.0) to 2.6 mm (η = 1.6) in a diameter. In addition to that, there is a relatively large discrepancy in the magnetization between D0 and D1. Assuming that all changes in magnetization are derived from α-Fe with the saturation magnetization of 2.16 T [26], 62% of the total Fe in the Cu-Fe wire D1 can be considered as α-Fe. These results was consistent with the fact that martensitic transformation from γ-Fe to α-Fe are induced by deformation, as previously confirmed [13, 23, 27, 28, 29, 30, 31]. However, since the magnetization of α-Fe becomes smaller after deformation, only a rough estimate was given here. Note that there is a difference between the previous study and this study in terms of whether the processing method is rolling or drawing, but it can be said that this difference is not critical.

The results of the VSM measurement revealed that the amount of α-Fe in the Cu-Fe wires undergoes a non-monotonic change with increasing working ratio η, and is also greatly affected by the aging temperature. Specifically, the increase in α-Fe, which was greater at higher aging temperature, was observed for η range from 0 to 1.6, but the α-Fe tended to decrease as η increased more than 1.6. Since γ-Fe and solid solution Fe, which have been suggested to be present in addition to α-Fe, have been found to have no magnetization at room temperature throughout the detailed studies by magnetic property measurement and the ^{57}Fe-Mössbauer spectroscopy by Shiga *et al*. [32, 33, 34, 35], other evaluations were needed to distinguish these two FCC phases at room temperature. This is described in chapter 3, where the results of several material analysis are discussed.

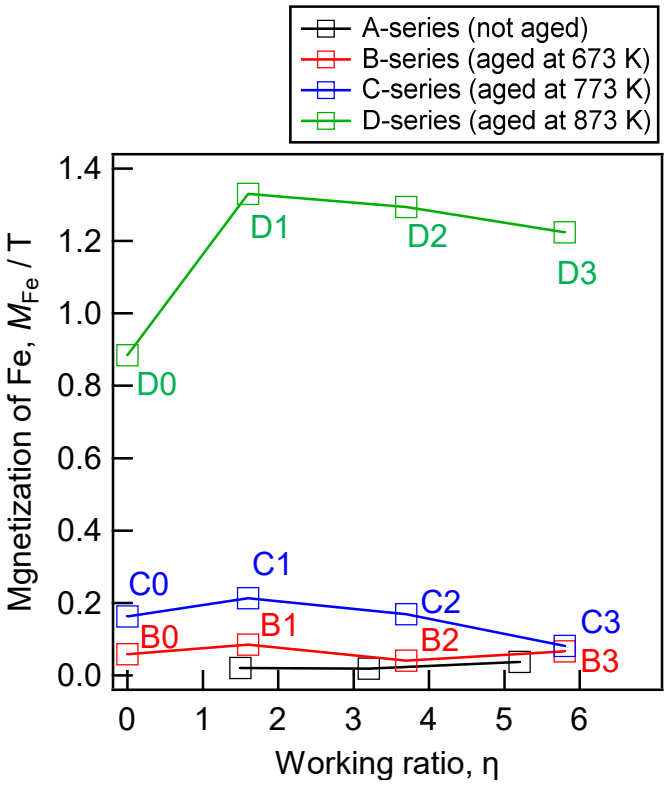

Figure 2.6 Magnetization of Cu-Fe wires before and after wire drawing.

2.4. Summary

The tensile strength of Cu-0.53 at% Fe wires increased monotonically after aging heat treatment at 673 K, 773 K, and 873 K for 8 h followed by wire drawing. Comparison of these three conditions of aging temperature showed that Cu-Fe wires that experienced aging heat treatment at 873 K had slightly higher strength than the other heat treatment temperatures, as long as the working ratio η ranging from 1.6 to 5.8. This suggests that precipitation strengthening has occurred due to aging treatment at 873K. Whereas, for η ranges above 8.1, little difference in tensile strength was observed. Assuming that the Fe particles were finely fragmented by wire drawing together with the matrix Cu crystal grains, it can be considered that the effect of precipitation strengthening has disappeared.

It was also shown that Cu-0.53 at% Fe may be a better conductor material for high-strength electric wires rather than pure copper. In other words, the tensile strength can be much greater than 500MPa, the upper limit of pure copper. Furthermore, it was shown that the rod of Cu-0.53 at% Fe cast to a diameter of 12.5 mm could also be drawn to an ultrafine wire of 0.05 mm without fragmentation. This excellent capability of plastic deformation is very useful industrially.

After aging heat treatment, electrical resistivity increased monotonically by wire drawing. The behavior of this increase was quite different for the three aging conditions. At an aging temperature of 673 K, the electrical resistivity began to increase drastically when the range of η exceeded 0. In the case of aging at 773 K, the electrical resistivity began to increase rapidly when the range of η exceeded 1.6, but remained almost unchanged in the range of η from 0 to 1.6. At an aging temperature of 873 K, the electrical resistivity clearly began to increase only when the η range exceeded 5.8.

Given that there were only slight differences in tensile strength, the effect of Cu matrix strain on electron conduction is not considered to be significantly different, and the electrical resistivity may have increased significantly due to an increase in the solid solution of Fe. Focusing on the samples aged at 873 K, the range of working ratio η where the effect of precipitation strengthening was no longer observed was consistent with the range where the electrical resistivity was clearly increased. Thus, it can be said that the Fe precipitates may have been finely fragmented by the wire drawing process, reproducing the similar results as in the previous studies by Boltax [16] and Nishikawa [21].

VSM measurements showed that magnetization definitely increased in the range of η from 0 to 1.6 for the 5.8 mm diameter wires aged at 773 K and 873 K, suggesting an increase of α-Fe precipitates. This was consistent with the phenomenon reported as martensitic

transformation from γ-Fe to α-Fe due to cold working. Conversely, magnetization decreased when the η range exceeded 1.6, suggesting that the α-Fe particles might have fragmented so finely that they became too small to be magnetized or became less magnetization due to stress.

The results of three different characterizations suggested changes of Fe precipitates by wire drawing. It has been suggested that Fe precipitates may be fragmented by wire drawing, but direct evidence is not yet available. In the following chapter 3, several material analysis were applied to detail the changes of Fe precipitates.

References

[1] J. D. Livingston, *Trans. TMS-AIME,* **215**, 566 (1959).

[2] V. A. Phillips, *Trans. TMS-AIME*, **230**, 967 (1964).

[3] D. Watanabe *et al., Metall. Mat. Trans. A*, **39**, 725 (2008).

[4] A.Bachmaier *et al., Mater. Charact.*, **100**, 178 (2015).

[5] D. W. Borland *et al., Scripta metall.*, **6**, 1201 (1970).

[6] R. W. Knights *et al., Metall. Trans.*, **4**, 2389 (1973).

[7] G.C.Weatherly *et al., Acta Metall.*, **27** (12), 1815 (1979).

[8] K. X. Wei *et al., Mater. Sci. Eng. A,* **528** (3), 1478 (2011).

[9] L. Peng *et al., J. Alloys Compd*., **708**, 1096 (2017).

[10] D. Liang *et al., Materials*, **13** (3), 732 (2020).

[11] Q. Mao *et al., Compos. B.,* **231**, 109567 (2022).

[12] F. Bitter and A. R. Kaufmann, *Phys. Rev*., **56**, 1044 (1939).

[13] C. S. Smith, *Phys. Rev.,* **57**, 337 (1940).

[14] J. Reekie *et al., Proc. Phys. Soc. B,* **66**, 1101 (1953).

[15] A. Boltax, *Trans. Met. Soc. AIME,* **218**, 812 (1960).

[16] A. Boltax, *Trans. Met. Soc. AIME,* **224**, 281 (1962).

[17] M, Shiga, *Jisei Nyuumon (Uchida Rokaku Ho)*, p.9 (2007).

[18] C. S. Smith, *Progress in Metal Physics,* **1**, 175 (1949).

[19] S. Aoyama, *Materia Japan,* **51** (6), 251 (2012).

[20] O. Izumi, *J. Japan Inst. Metals*, **4** (2), 101 (1965).

[21] S. Nishikawa *et al., Seisan-kenkyuu,* **18** (11), 312 (1966).

[22] J. O. Linde, *Ann. D. Phys.,* **407** (2), 219 (1931).

[23] R. E. Cech *et al., JOM*, **6**, 45 (1954).

[24] M. Kato *et al., J. Japan Inst. Metals*, **56** (8), 865 (1992).

[25] N. Ishikawa and A. Sato, *Philos. Mag. A*, **64** (2), 387 (1991).

[26] H. Zijlstra, *Experimental methods in magnetism (North-Holland Publishing Company)*, **1**, 145 (1967).

[27] C. S. Smith, *Progress in Metal Physics,* **1**, 212 (1949).

[28] K. E. Easterling and H. M. Miekk-Oja, *Acta Metall.,* **15** (7), 1133 (1967).

[29] S. Fukui *et al., Denki Seiko,* **44** (3), 193 (1973).

[30] M. Kato *et al., Acta Metall.,* **26** (4), 605 (1978).

[31] M. Kato *et al., J. Japan Inst. Metals*, **56** (8), 865 (1992).

[32] M. Shiga*, JPSJ*, **22** (2), 539 (1967).

[33] M. Shiga *et al., JPSJ*, **37** (2), 363 (1974).

[34] K. Sumiyama *et al., Trans. JIM*., **26** (4), 217 (1985).

[35] K. Sumiyama *et al., Nucl. Instrum. Methods Phys. Res. B,* **76** (1), 33 (1993).

Chapter 3 Characterization of precipitates in dilute Cu-Fe alloys

3.1. Introduction

In this chapter, dilute Cu-Fe alloys were examined using several analytical methods, both laboratory analytical instruments and quantum beam analysis technologies. First of all, XRD measurements were performed to determine whether the 0.05 mm diameter ultrafine wire contained α-Fe phase or not when it had been drawn from the diameter of 5.8 mm to 0.05 mm. Since it is hard to detect by using normal laboratory XRD due to the very small amount of Fe content (0.53 at%), synchrotron radiation XRD was applied. Incident X-rays obtained by synchrotron radiation have much higher photon flux than those obtained by the normal X-ray tube and are therefore very suitable for the analysis of ultrafine wires. High spatial resolution analysis was then performed on two ultrafine wires, one with α-Fe phase and one without α-Fe phase. TEM and 3D-APT analysis were applied for this purpose and find out the position and the shape of Fe precipitates and the concentration distribution of Fe atoms. Each specimen of these laboratory instruments (XRD, TEM, and 3D-APT) was prepared from the wire diameter of 0.05 mm, respectively. Finally, by applying two types of quantum beam analysis, Cu-Fe wires with the same or larger diameters than these ultrafine wires were also analyzed. The size of Fe precipitates in Cu was investigated by small-angle neutron scattering (SANS) with sufficient transmission capacity of the neutron beam for thick Cu wire. And three kinds of Fe were investigated X-ray absorption fine structure (XAFS) performed at synchrotron radiation facilities. XAFS measurements were applied to samples with a wide range of diameters, from a maximum diameter of 12.5 mm to a minimum of 0.05 mm. A list of measured Cu-Fe wires to which each analytical method was applied is shown in Table 3.1.

The Fe-Cu alloys are well known as an analogy for the Cu-Fe alloys studied in this work. Due to their age-hardenability, Fe-Cu alloys have been widely studied as industrial materials or materials for nuclear reactors [1, 2, 3, 4] using pioneering theoretical calculations [5, 6] as well as advanced analytical methods such as TEM [7, 8, 9], atom-probe [10, 11, 12, 13, 14], SANS [15, 16] and XAFS [17, 18, 19]. The Cu precipitation behavior in Fe was analyzed thoroughly using SANS by Osamura *et al* [15, 16]. Not only SANS but also SAXS was used. For example, the interfacial segregation of a minor element added to Fe-Cu alloys can be detected by anomalous small-angle X-ray scattering (ASAXS) [20, 21] using X-rays near its absorption edge, as reported by Okuda *et al*.

Since these analytical methods are already known to be powerful for investigating the aging precipitates, the author attempted to verify that the results of each analytical method are consistent with each other and with the material characterization results in the chapter 2.

Because TEM and 3D-APT have high spatial resolution and a narrow analytical field of view, ultrafine wires with a relatively homogeneous microstructure are used as the specimens. Since SANS with its high transmission capacity requires a large specimen volume, a relatively thick wires were selected to be analyzed. Although all wire diameters were analyzed by XAFS, it was not yet clear whether XAFS could be used to analyze the amount of solid solution element which is one of the focus of this thesis. So Fe-K XANES study was performed with the combination of experimental and theoretical calculations. Experimental XANES and EXAFS analysis is described in this chapter and then theoretical XANES calculation is described in the following chapter 4.

Table 3.1 List of analytical methods applied to Cu-0.53 at% Fe wires at each diameter.

Sample and process information				Analytical methods (○ : performed, - : not performed)				
Sample name	Wire diameter	Aging temperature	Working ratio η	XRD	TEM	3D-APT	SANS	XAFS
A0	12.5 mm	not aged	0.0	-	-	-	-	○
A1	5.8 mm	not aged	1.5	-	-	-	○	○
A2	2.6 mm	not aged	3.2	-	-	-	-	○
A3	0.90 mm	not aged	5.3	-	-	-	-	○
A4	0.32 mm	not aged	7.3	-	-	-	-	○
A5	0.10 mm	not aged	9.7	-	-	-	-	○
A6	0.05 mm	not aged	11	○	-	-	-	○
B0	5.8 mm	673 K	0.0	-	-	-	○	○
B1	2.6 mm	673 K	1.6	-	-	-	-	○
B2	0.90 mm	673 K	3.7	-	-	-	○	○
B3	0.32 mm	673 K	5.8	-	-	-	○	○
B4	0.10 mm	673 K	8.1	-	-	-	-	○
B5	0.05 mm	673 K	9.5	○	-	-	-	○
C0	5.8 mm	773 K	0.0	-	-	-	○	○
C1	2.6 mm	773 K	1.6	-	-	-	-	○
C2	0.90 mm	773 K	3.7	-	-	-	○	○
C3	0.32 mm	773 K	5.8	-	-	-	○	○
C4	0.10 mm	773 K	8.1	-	-	-	-	○
C5	0.05 mm	773 K	9.5	○	○	○	-	○
D0	5.8 mm	873 K	0.0	-	○	-	○	○
D1	2.6 mm	873 K	1.6	-	-	-	-	○
D2	0.90 mm	873 K	3.7	-	-	-	○	○
D3	0.32 mm	873 K	5.8	-	-	-	○	○
D4	0.10 mm	873 K	8.1	-	-	-	-	○
D5	0.05 mm	873 K	9.5	○	○	○	-	○

3.2. Experimental procedure

3.2.1 Specimen preparation and measuring condition of XRD

XRD measurements were performed at BL19B2 of SPring-8 in a transmission mode known as Debye-Scherrer type arrangement [22, 23, 24]. The photon energy of the incident X-ray, monochromatized using a Si (111) double crystal monochromator, was 24.99 keV (0.04961 nm in X-ray wavelength). XRD profiles were obtained from the four of Cu-0.53 at% Fe ultrafine wires (A6, B5, C5 and D5) and from the CeO_2 powder (NIST SRM674a) as a standard sample. Since these ultrafine wires were only 0.05 mm in a diameter and could not support their own weight, each of them was fixed in a glass capillary of 0.10 mm diameter and then fixed on the sample holder for diffractometer. The standard CeO_2 powder was sealed in a 0.10 mm diameter glass capillary. All samples were rotated 18° per second during the measurement and exposed four times each with an exposure time of 20 seconds. Sample holders for the capillaries and other details of this high-throughput diffractometer for industrial use [25] are recently reported by Osaka *et al*.

3.2.2 Specimen preparation and measuring condition of TEM

The thin specimens for TEM observations were prepared by a focused ion beam (FIB) method using a Ga ion beam. The FIB machining technique is essential to obtain TEM images at the desired area for a copper ultrafine wire, because the longitudinal cross section along the wire drawing direction and the transverse section perpendicular to it may often exhibit different microstructures, as shown in Figure 3.1(a). In this study, the coordinate system for the Cu-Fe ultrafine wire is defined so that the axial direction (AD) is parallel to the wire drawing direction, as shown in Figure 3.1(b). The radial direction (RD) is also shown in this Figure, and the electron beam was injected to be perpendicular to the AD-RD plane when TEM observation was performed. The STEM observation was performed to investigate nanometer-sized Fe precipitates in Cu matrix using a JEM-2100F (JEOL, Japan) equipped with a field emission gun and operated at 200 kV. Both of the bright field (BF) STEM images and high-angle scattering dark field (DF) STEM images were taken and the abbreviations (BF and DF) were noted in the upper left corner of the STEM images. Elemental analysis was performed using energy dispersive X-ray analysis (EDX) attached to the TEM instrument. Three specimens were prepared for this study, as already shown in Table 3.1, two of them are ultrafine wires with a diameter of 0.05 mm, namely C5 and D5, and the other is a thick wire with a diameter of 5.8 mm named D0.

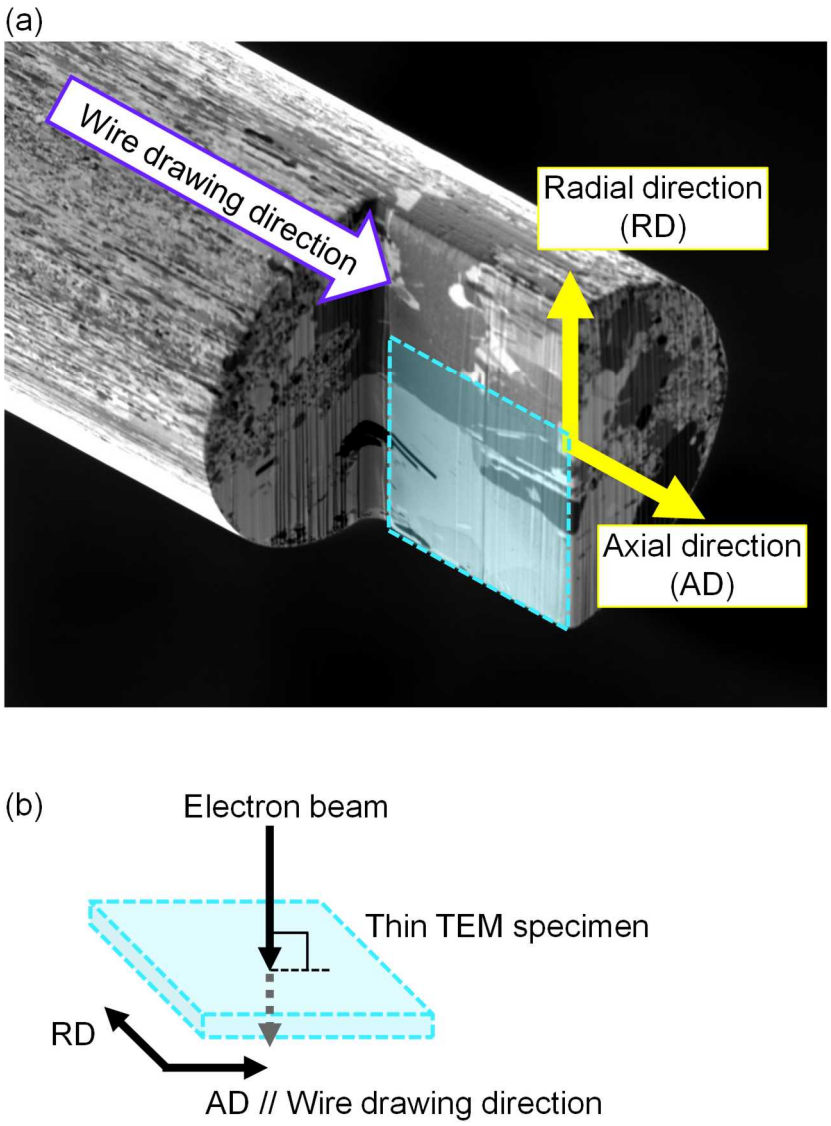

Figure 3.1 The metallurgy of an ultrafine wire and the corresponding coordinate system.

(a) SEM image of Cu-Fe ultrafine wire in a diameter of 0.05 mm.

Axial direction (AD) is parallel to the wire drawing direction.

(b) Electron beam is injected perpendicular to the AD-RD plane in TEM instrument.

3.2.3 Needle-shaped specimen preparation and measuring condition of 3D-APT

3D-APT analysis was performed to characterize Fe precipitates at atomic resolution after wire drawing. Instead of having a very narrow field of view, 3D-APT has extremely high spatial resolution and high elemental detection sensitivity of any laboratory analytical technique. Commonly, a needle-shaped specimen is only 100 nm long and 30 nm in diameter, and the spatial resolution of its data is less than 1 nm along the longitudinal direction and less than 2 nm along the radial direction [26]. The reconstructed atom map data of Cu-Fe alloys were analyzed to determine the distribution of Fe atoms and the concentration gradient at the interface between the Fe precipitates and the Cu matrix.

Figure 3.2 shows the schematic diagram of specimen preparation and 3D-APT measurement. A needle-shaped specimen preparation for 3D-APT measurements were performed by FIB method using a Ga ion beam. The FIB machining was suitable for microfabrication, so that the axial direction of the needle-shaped specimen was successfully made parallel to the wire drawing direction. The FIB machining was essential for this purpose although the electrochemical polishing method is often used for needle-shaped specimen preparation of the metallic materials.

To compare ultrafine wires C5 and D5 of 0.05 mm diameter, which are the same ones for STEM observation, both of them were selected as the base material of needle-shaped specimens to be fabricated. Figure 3.3 shows specifically how the specimens were made and how to make the axis direction of needle-shaped specimen and wire drawing direction of base material parallel to each other. The location where the needle-shaped sample was finally taken was intended to be approximately 0.025 mm inside the wire's outer circumference, as shown in Figure 3.3 (b) and (e). The longitudinal direction of the needle was fabricated to be parallel to that of the each ultrafine wire and the needle-shaped specimens were obtained near the center of transverse section. Figure 3.3 (c) and (f) shows the needle-shaped specimens fabricated from them. Two specimens were successfully prepared for each of C5 (aged at 773 K) and D5 (aged at 873 K), and 3D-APT measurements and data analysis were also performed for each. Therefore, the sub-numbers of the data set were appended to the name of the base material as C5_574, C5_573, D5_605 and D5_607, which are also noted on the SEM images. Two needle-shaped specimens prepared for each of C5 and D5 were field-evaporated in the instrument, and a resulting data set, four in total, were reconstructed in three dimensions with atomic configurations. 3D-APT measurement by electric field evaporation and data collection were performed using a Local Electrode Atom Probe, LEAP4000XSi (Cameca, USA) by laser-pulsing acquisition method with a laser wavelength of 355 nm. Although the voltage-

pulsing method has been conventionally used for the analysis of metallic materials [27, 28, 29], the laser-pulsing method was adopted for this study, which has advantages such as a wide field of view for analysis due to small electric field stress [30]. The collected data were analyzed using the software IVAS (Cameca, USA) to visualize the three dimensional atomic configurations which is known as the atom map. The needle-shaped specimen shown in Figure 3.3 (c) and (f) is long enough (about 500 nm), but the electric field stress applied to specimens during the measurement causes them to crack before the entire volume is field-evaporated. Therefore, the longitudinal length of the needle-shaped specimen was only 100 nm to a maximum of 200 nm in the reconstructed atom arrangement shown later.

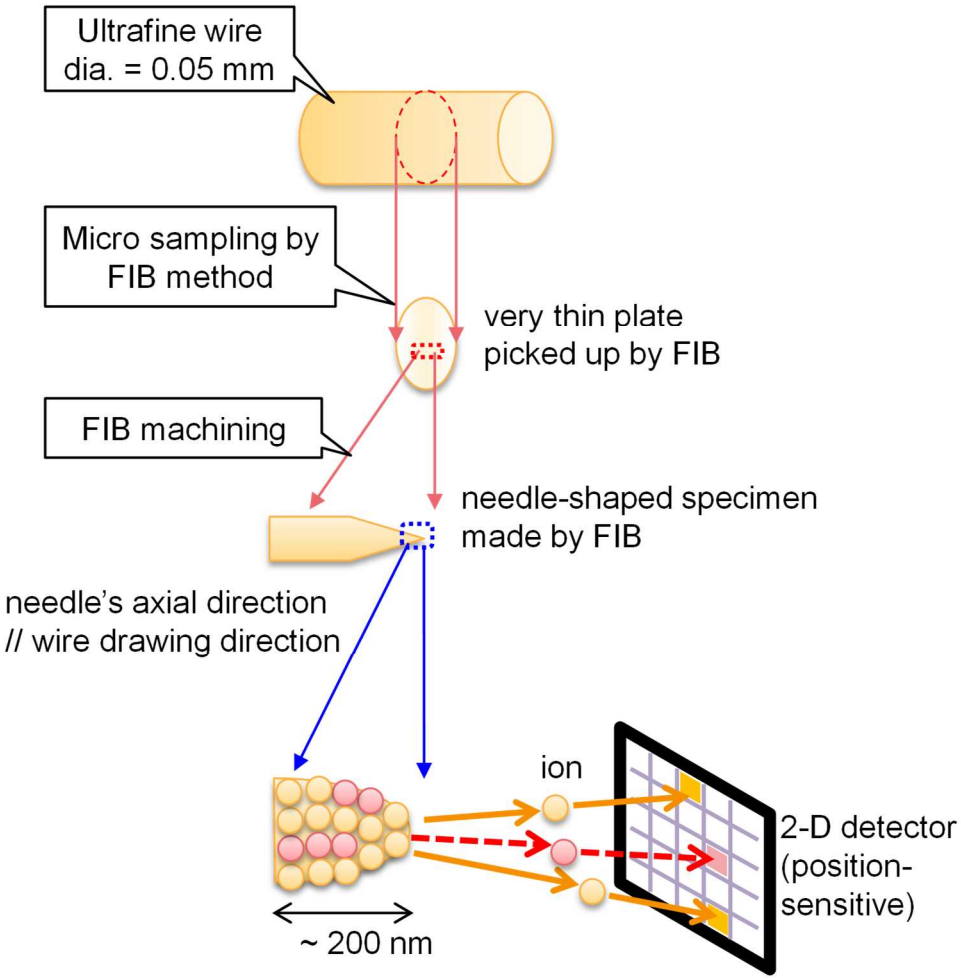

Figure 3.2 Schematic illustration of specimen preparation and 3D-APT measurement.

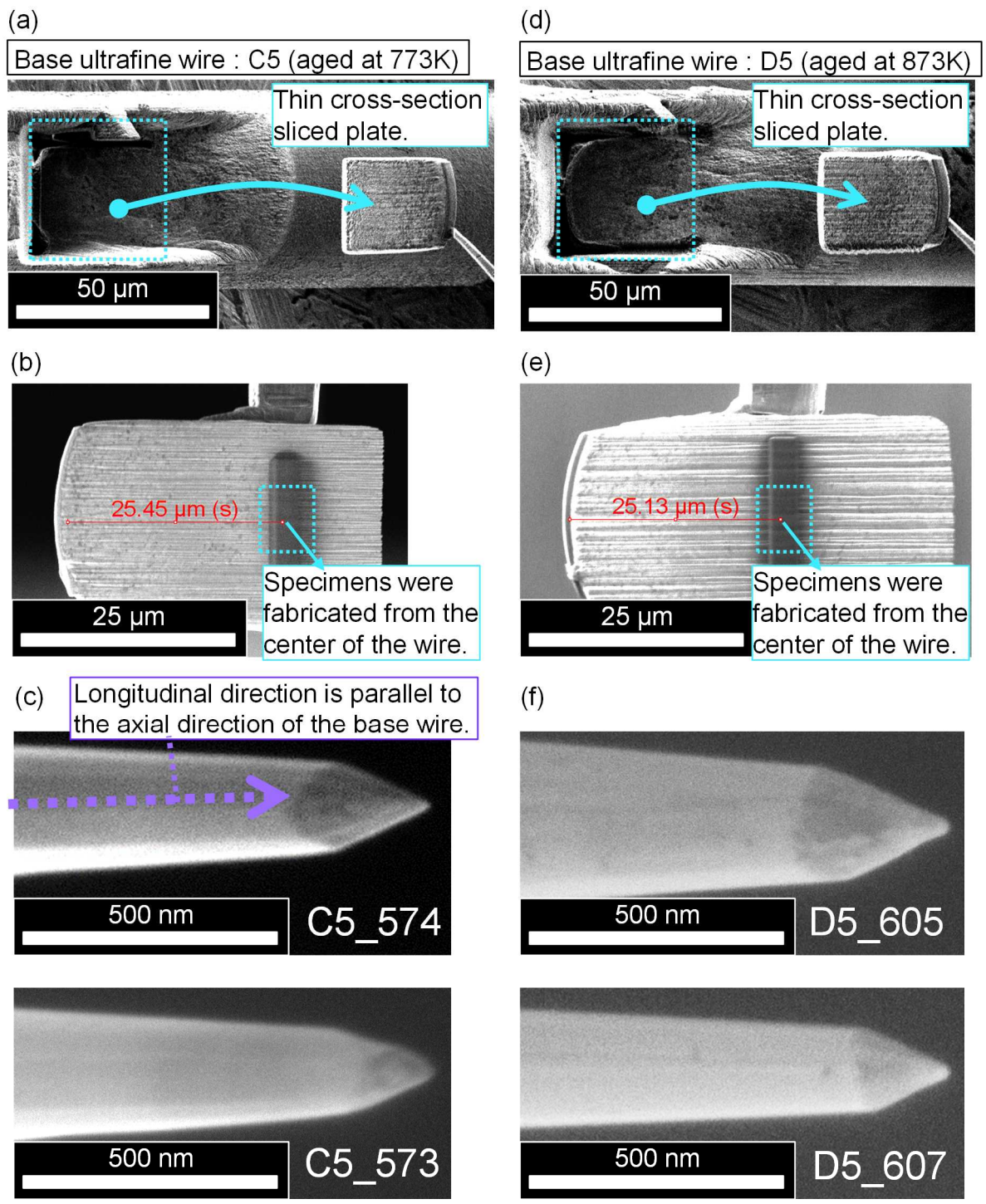

Figure 3.3 SEM images of specimens for 3D-APT taken from base ultrafine wires.

(a, d) SEM images of FIB lift-out thin plates from 0.05 mm dia. ultrafine wires.

(b, e) Aimed positions of FIB machining from the cross-sectional thin plate.

(c, f) SEM images of needle-shaped specimens. Two needles were made for each C5 and D5.

3.2.4 Specimen preparation and measuring condition of SANS

Since it is difficult to comprehensively examine thick wires by either STEM or 3D-APT, other attempts were made to obtain complementary information. One method is SANS described in this section, which is useful to find the size of precipitates. The other method is XAFS described in the following section, which is sensitive to the local environment of Fe at atomic-level.

Although many reports about precipitation in some kinds of metallic alloys have found that Small Angle X-ray Scattering (SAXS) is suitable to find out the size distribution of the precipitates [31, 32], SAXS was not always the best method for this study because the expected scattering intensity of Fe in Cu is weak and X-ray transparency is low. For example, the transmission capability of 25 keV incident X-ray for copper with a thickness of 0.32 mm is less than 1%, so SAXS is not suitable for thick copper materials unless very thin specimen is successfully prepared. In order to investigate copper wires of various diameters in this study, it was not easy to make all of them to the optimum thickness for SAXS. As another example, a neutron beam with a wavelength of 1 Å has a transmission capability higher than 50% through a 5.8 mm thick copper, which is suitable for measurements in this study. Both SAXS and SANS are considered to be able to detect differences in scattering contrast between Cu and Fe, but SANS was better in this study due to its permeability. From the perspective of scattering contrast alone, the difference is not decisive, since Cu is 10% larger than Fe in the case of X-ray scattering length density (SLD) and Fe is just 20% larger than Cu in the neutron SLDs.

SANS specimens were prepared as follows. The Cu-Fe wires with 5.8 mm diameter (named A1, B0, C0 and D0) were cut into 1-mm-thick coin-shaped discs and provided for the measurement. Other wires with diameters of 0.9 mm or 0.32 mm (B2, B3, C2, C3, D2 and D3) were prepared by laying the wires side by side on each sample holder.

SANS measurements were performed at BL20 iMATERIA at the Japan Proton Accelerator Research Complex (J-PARC). Figure 3.4 shows schematic illustration of SANS measurement. Since the incident neutron beam was injected perpendicular to the sample holder, the beam was irradiated perpendicular to the cross-section of the 5.8 mm diameter wires as shown in Figure 3.4 (a). And the beam was irradiated from the side of the other diameter wires as shown in Figure 3.4 (b). Scattering intensity measured by the detectors installed in the iMATERIA were converted to 1-D profiles after subtracting the contribution of air and background intensity. To obtain the scattering intensity $I(q)$ of the 1-D profile, intensity integrations from 2-D detectors were made in two different directions as shown in Figure 3.4 (c). 1-D SANS

profile of vertically scattered intensity was obtained from the 30° sectors perpendicular to the wire drawing direction and labeled with "_Vertical". The other of horizontally scattered intensity was obtained from 30° sectors parallel to the wire drawing direction and labeled with "_Horizontal". Although both were considered equivalent after aging heat treatment, they gave different intensities in the drawn specimens. Here, the 1-D profile in the horizontal direction, where the scattering was observed to be stronger, was used in this analysis. This corresponds to the direction perpendicular to the wire drawing direction. From the SANS profile one can obtain particle size and its variance with a simple assumption [33, 34]. In this study, the fitting analysis was performed using the results of TEM observations as initial values. Assuming that the Fe precipitate is a simple homogeneous sphere, the fitting function is expressed as following equation (3.1), where S is the scale factor as a variable, V is the volume of the Fe precipitate, r is the radius of the precipitate as a variable, a constant B is the background level and Δb is the difference of the SLDs between the Fe precipitate and the Cu matrix.

$$I(q) = \frac{\mathrm{S}}{V}\left\{3V(\Delta b)\frac{\sin(qr) - qr\cos(qr)}{(qr)^3}\right\}^2 + \mathrm{B} \qquad \text{Equation (3.1)}$$

The shape of Fe precipitates was considered to be the spheres with uniform SLD, and previous atom-probe investigation has revealed that Fe precipitates after aging heat treatment are homogeneously composed of pure Fe [10].

The initial value of the radius r was independently investigated by STEM-EDX. A HAADF STEM image was taken and the elemental analysis was performed using EDX attached to the TEM instrument. These STEM observation was performed using a JEM-2100F (JEOL, Japan) equipped with a field emission gun and operated at 200 kV in the same way as shown in Section 3.2.2.

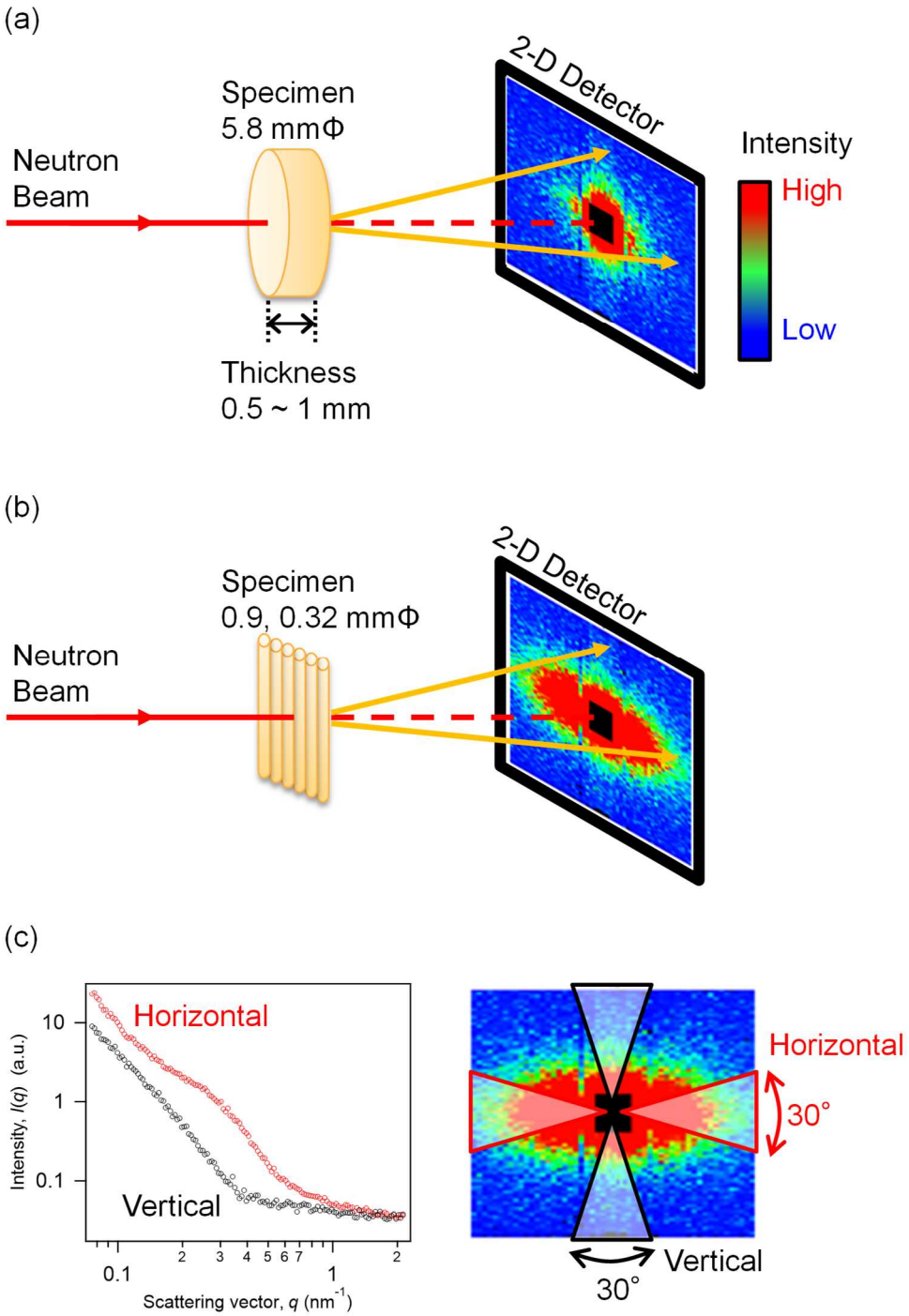

Figure 3.4 Schematic illustration of SANS measurement in this study.

(a) Arrangement for measuring Cu-Fe wire in a diameter of 5.8mm.

(b) Arrangement for measuring Cu-Fe wire in a diameter of 0.9 or 0.32 mm.

(c) 1-D SANS profile integrated horizontally or vertically from 2-D detectors.

3.2.5 Specimen preparation and measuring condition of XAFS

Collected data of XAFS in this study were including both X-ray Absorption Near Edge Structure (XANES) and Extended X-ray Absorption Fine Structure (EXAFS). XANES and EXAFS were analyzed to find out the three types of states, i.e., substitutional solute in Cu (FCC) as denoted by Cu(Fe) in this thesis, α-Fe and γ-Fe. Some of XANES spectra would be compared to calculated XANES spectra in the following chapter 4. The experimental EXAFS and XRD of mechanically alloyed dense Cu-Fe powders has been analyzed by Harris [35] to reveal the local structure of Fe atom when the crystal structure had been BCC or FCC. In the same way, EXAFS was expected to be able to reveal the local environment of Fe atom in dilute Cu-Fe alloys. Since different detection methods might cause slight differences in XAFS spectra, some of Cu-Fe wires were measured by both of transmission method and fluorescent method to confirm the difference between the spectra before and after normalization. And then the normalize condition and the "flatten" condition were also reconsidered as described in following section 3.2.6.

XAFS measurements were performed at synchrotron radiation facilities (SPring-8 BL16B2 and SAGA-LS BL16). Pure iron foil (0.01 mm thickness, Takeuchi Metal Foil & Powder) was used as reference of BCC-Fe. Fe-37 at% Ni alloy foil (0.01 mm thickness, Takeuchi Metal Foil & Powder) and Fe-43 at% Ni alloy foil (0.01 mm thickness, Takeuchi Metal Foil & Powder) were used as reference of FCC-Fe, because pure γ-Fe (FCC) is unstable at room temperature under thermodynamic equilibrium. The effect of Ni will be discussed in the section 3.3.5.

All of the measured Cu-Fe wires were already listed in Table 3.1. The 12.5 mm diameter wire named A0 was annealed at 1173 K for 1hour, followed by quenching into a mixture of ethanol and water before XAFS measurement. Since the solute concentration was within the solubility limit at 1173 K [36], it is natural that the specimen A0 is consist of a single phase of Cu(Fe) in which Fe exists as substitutional solute in Cu. Before the XAFS measurement of the Cu-Fe wires, their surface oxide layer was removed by polishing with an emery paper from #400 to #2000 by hand. Only simple polishing was applied, but no other special pretreatment was required, which means that XAFS requires less pretreatment than other analytical methods such as TEM, 3D-APT, and SAXS (not SANS).

A Si(111) double-crystal monochromator was used to extract monochromatized X-rays from synchrotron orbital radiation and Rh or Pt coated mirror was used to remove unwanted high orders of radiation. A software Athena [37] was employed for analyzing EXAFS and data processing for linear-combination-fitting (LCF) of XANES. In the case of fluorescence method, the Fe-Kα fluorescence X-ray intensity was divided by the incident X-ray intensity to calculate

the raw X-ray absorption intensity at every measured incident photon energy point. As described in the next section, the energy of continuous X-rays emitted from the Cu-Fe wires were selected by the energy dispersive X-ray detector installed in the beamline.

3.2.6 Normalizing condition of XAFS spectra

As described in previous section 3.2.5, XAFS measurements of several Cu-Fe samples were performed by both of transmission and fluorescence method. Ideally, it would be a good choice to measure all Cu-Fe samples by the transmission method as well as standard samples, but considering the wide range of Cu-Fe sample diameters, it becomes necessary to measure them by the fluorescence method. There are two main points to be careful with the fluorescence method: the first is the conditions for setting the "Region Of Interest" (ROI), and the second is the conditions for the normalization.

In this section, Cu-Fe sample A2 was used to compare the differences between the transmission and fluorescence methods. There are relatively few restrictions on sample thickness for the fluorescence method, but the transmission method requires the sample to be thin enough to be measured, so an appropriate thickness was considered at first. Specifically, there is an appropriate thickness because if a sample is too thick, the transmittance is too low to apply the transmission method, while if it is too thin, the signal intensity of iron is too reduced to be measured. After discussing the optimum thickness for the transmission method, a comparison of data from the transmission and fluorescence methods will be presented.

First, a system that can simultaneously measure XAFS by both of transmission and fluorescence methods is described.

The XAFS measurement system used in this study is shown in Figure 3.5. The incident X-ray intensity I_0 was measured with an ionization chamber, the transmitted X-ray intensity I_1 was measured with another ionization chamber, and the fluorescent intensity I_{FY} was measured with an energy-resolved detector. Each signal intensity was measured at the exact same time by a counter timer at each measurement energy of XAFS and measurements were taken at room temperature and in air. The linearity of the X-ray counts collected by the ionization chamber in this measurement system is very important for later discussion and will be supplemented here. In basic study experiments at several Japanese synchrotron radiation facilities, it has been confirmed that the same type of ionization chamber (OYO KOKEN KOGYO, Japan) can ensure sufficient linearity at more than 10,000 cps [38]. The counter timer of the measurement system used in this study also has sufficient linearity in the range of 10,000 to 900,000 cps. Therefore, linearity up to 90 times, namely up to 4.5 times as the natural logarithm, can be guaranteed.

The following is a description about how much thickness of the Cu-0.53 at% Fe specimen is appropriate for transmission method XAFS.

The absorbance μ_{total} measured by the transmission method is calculated by the following equation (3.2), also known as the Lambert-Beer law, where the thickness of the sample is t_{sample}.

$$\mu_{\mathrm{total}} \cdot t_{\mathrm{sample}} = \ln\left(\frac{I_{\mathrm{inc}}}{I_{\mathrm{tr}}}\right) = \mu t \qquad \text{Equation (3.2)}$$

This equation would be correct if the incident X-ray intensity I_{inc} and transmission X-ray intensity I_{tr} were measured with exactly the same detector, but since two different ionization chambers were used as the detectors in this XAFS study as already shown in Figure 3.5, the following must be considered.

The XAFS measurement system in this study enables us to count the incident intensity I_0 and transmission intensity I_1 simultaneously in two ion chambers which are denoted as IC in Figure 3.5. If the linear absorption coefficient is μ_{total}, the following equation (3.3) is obtained. This equation includes the absorption coefficient μ_A due to the Fe element, μ_B due to the matrix element Cu, and μ_C due to other minor environmental effects.

$$\ln\left(\frac{I_0}{I_1}\right) = \mu t = (\mu_{\mathrm{A}} + \mu_{\mathrm{B}} + \mu_{\mathrm{C}}) \cdot t_{\mathrm{sample}} \qquad \text{Equation (3.3)}$$

As long as the measurement is performed under normal atmospheric conditions, μ_C is negligibly small compared to the other two absorption coefficients, so there are three parameters to keep in mind before measuring the XAFS spectra: μ_A, μ_B and t_{sample}. For the XAFS measurement in this study, the $\ln(I_0/I_1)$ that can be measured as a result of including all effects is plotted as absorbance μt.

For Cu-0.53 at% Fe, a sample thickness (t_{sample}) of 0.079 mm is expected to give the best signal-to-noise ratio (S/N) according to the report on how to estimate the optimum thickness considering the S/N for a typical transmission XAFS measurement, which is given by the previous study [39]. And the Japan Synchrotron Radiation Research Institute (JASRI) provides a software that can easily estimate optimal thickness. However, since it is difficult to adjust the thickness to exactly 0.079 mm, the upper limit of the thickness was considered as follows. If t_{sample} is too thick, the difference in μt between the low and high energy sides of the XAFS spectrum will become too large, which will cause problems with the linearity of the X-ray intensity measured by the ionization chamber for I_1. The differential Absorption $\Delta\mu t_{(8000/6800)}$ between μt at 8000 eV and μt at 6800 eV in Cu-0.53 at% Fe is calculated from the X-ray absorption coefficient of each element and is shown in Figure 3.6. If $t_{sample} > 0.18$ mm, it is not appropriate for XAFS measurement in this study because $\Delta\mu t_{(8000/6800)}$ will be > 4.5 which does not guarantee linearity of I_1 as described above. Therefore, the thickness of

the specimen for transmission method were prepared to be 0.18 mm or less, and thickness measured with calipers is marked in Figure 3.6.

The following is a description about normalization of XAFS spectra by transmission method.

Figure 3.7 shows typical data sets measured by the transmission method, as well as the measured μt and the calculated background curves. The analysis software Athena can display the background as a straight line and normalized spectra. For a pure iron foil of 0.010 mm thickness, the normalized intensity near the absorption edge is almost 1, and the intensity gradually decreases at higher photon energy (Figure 3.7 (c)). This is natural, because the X-ray attenuation coefficient of an iron foil in the energy range above the Fe-K absorption edge gradually decreases at higher incident X-ray energies [40, 41, 42]. On the other hand, in the case of Cu-0.53 at% Fe, the normalized intensity near the absorption edge is almost 1, but the normalized intensity at 8000 eV is more than 3 (Figure 3.7 (d)). This is because the effects other than Fe, i.e., the energy dependence of absorption coefficient of Cu matrix as estimated in Figure 3.6, cannot be ignored. For convenience when comparing with the following fluorescence method, the normalized absorbance, which is raised by effects other than Fe, was fitted with a quadratic polynomial and forced to adjust around 1 in order to reduce this effect. Athena implements this data processing, which is called “flatten”, but it is supposed to be applied with caution. How the author "flattened" the normalized absorbance is described in this section after the description of normalizing XAFS spectra.

The following is a description of normalization of XAFS spectra by fluorescence method.

Figure 3.8 shows a typical measurement flow in the fluorescence method. The measured absorbance μt can be approximated by simply dividing the Fe-Kα X-ray fluorescence intensity I_{FY} by I_0 as in the following equation (3.4) due to the dilute Fe concentration and the minor influence of the Cu absorption coefficient.

$$\mu t \sim \frac{I_{FY}}{I_0} \qquad \text{Equation (3.4)}$$

As already shown in Figure 3.5 and Figure 3.8, the MCA collects energy-dispersive data of continuous X-ray intensity emitted from the Cu-0.53 at% Fe specimen and records only a part of it as I_{FY} data. The energy range of I_{FY} as fluorescent X-ray intensity retrieved from the data collected by MCA is commonly called the ROI, and the ROI should be set not to include the scattering of incident X-rays. In this study, I_{FY} must include Fe-Kα line to obtain the Fe-K edge absorption spectra by the fluorescence method.

To consider about the ROI conditions, an contour map of the total continuous X-ray intensity collected at each measured photon energy of incident X-ray is shown in Figure 3.9. In this

figure, incident X-rays scattered from the sample are also observed, and Fe-Kα lines began to be observed in the energy range above 7110 eV. If a ROI is set up that includes even a small amount of incident X-rays, it will have an unnaturally high intensity in the background region (7000~7110 eV in photon energy range), as shown by the blue plot in Figure 3.10. Therefore, if the upper limit of ROI is too high, it creates a suffering that background intensity cannot be subtracted correctly. If the ROI window is too narrow, the S/N will be poor, as shown by the red plot in Figure 3.10; in the case of Cu-0.53 at% Fe, the ROI window is set from 6095 eV to 6495 eV, and the appropriate measurement data can be obtained as shown by the black plot in Figure 3.10.

Figure 3.11 shows an ordinary XAFS spectrum measured by the fluorescence method with a red background line. A slightly rightward rising absorbance μt is observable in Figure 3.11(a). Then, Figure 3.11(b) shows a plot of absorbance normalized per Fe atom indicating that the intensity near the absorption edge is almost 1, but the normalized intensity at 8000 eV is about 1.2. This is due to the absorption of incident X-rays in the air and the attenuation length of the measured specimen. In this measurement system, the air length from the ionization chamber for I_0 to the measured specimen is approximately 200 mm. The attenuation of X-rays in air is 6% less at 8000 eV than at 7200 eV, and the attenuation length into the measured specimen is 29% greater. These effects steadily increase the I_{FY} intensity in the higher photon energy region than the absorption edge energy. The effect of the penetration depth on how much it increases depends on the angle made by the incident X-rays and the detector. In this study, the center of the detector was placed in the same horizontal plane as the X-ray optical axis, and the line connecting the specimen and the detector is positioned orthogonally to the optical axis.

The following is a description about flattening of normalized XAFS spectra by both of transmission method and fluorescence method.

After plotting normalized absorbance vs photon energy, then flattening conditions were set so that the data collected by the transmission method could be compared and displayed in the same manner as the data collected by fluorescence method. This data processing method, named “flattening”, is implemented as a function of the software Athena by default, which displays the EXAFS vibration center as approximately 1 in the energy region higher than the absorption edge energy. Flattening is easily done with the Athena feature and is very useful for analysts to evaluate data at high speed, but careful consideration must be given when applying this function, as mentioned by Bruce, the software producer [37].

Two normalized spectra before and after flattening correction which were measured by both of transmission and fluorescence method are shown in Figure 3.12(a) and (b), respectively. In the photon energy range up to approximately 7170 eV, considered to be XANES, there is no particular change in the flattened or normalized spectra. In the case of XAFS spectra measured by the transmission method (Figure 3.12(a)), the normalized absorbance indicate clearly much higher than the flattened one in the photon energy range above 7150 eV. Similarly, the fluorescence method (Figure 3.12(b)) shows slight differences in the photon energy range above 7170 eV. In the following descriptions of this thesis, the observed X-ray absorbance μt will be displayed as "Normalized absorbance" when it is only normalized, or displayed as "Flattened absorbance" when it is both normalized and flattened. As shown in Figure 3.12(c), "Flattened absorbance" is useful because it makes the transmission and fluorescence spectra look the same. Note that the presence or absence of the flatten correction does not affect the EXAFS analysis at all, as the producer of the analysis software Athena mentions [37]. In the section 3.3.5, these issues are taken into account and then discussed using the results of EXAFS and XANES analysis. Although flattened or not is usually influential in the LCF analysis, the author used the incident photon energy range where no significant difference appears between normalized and flattened spectra. This means that the way of flattening is taken into account in this study so that it does not affect the results of the LCF analysis.

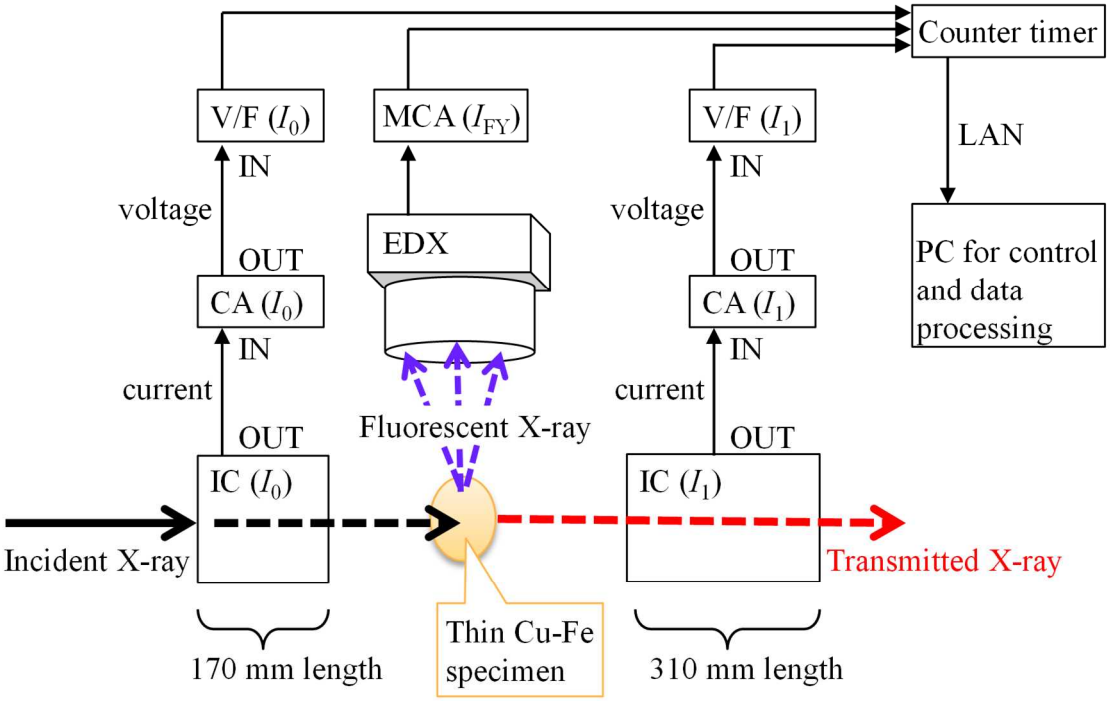

Abbreviation of equipments

V/F : Voltage-to-frequency converter

CA : Current Amplifier

IC : Ionization Chamber

MCA : Multi Channel Analyzer

EDX : Energy Dispersive X-ray Detector (such as Silicon drift detectors and Semiconductor Detectors)

Figure 3.5 Schematic illustration of the XAFS measurement system in this study.

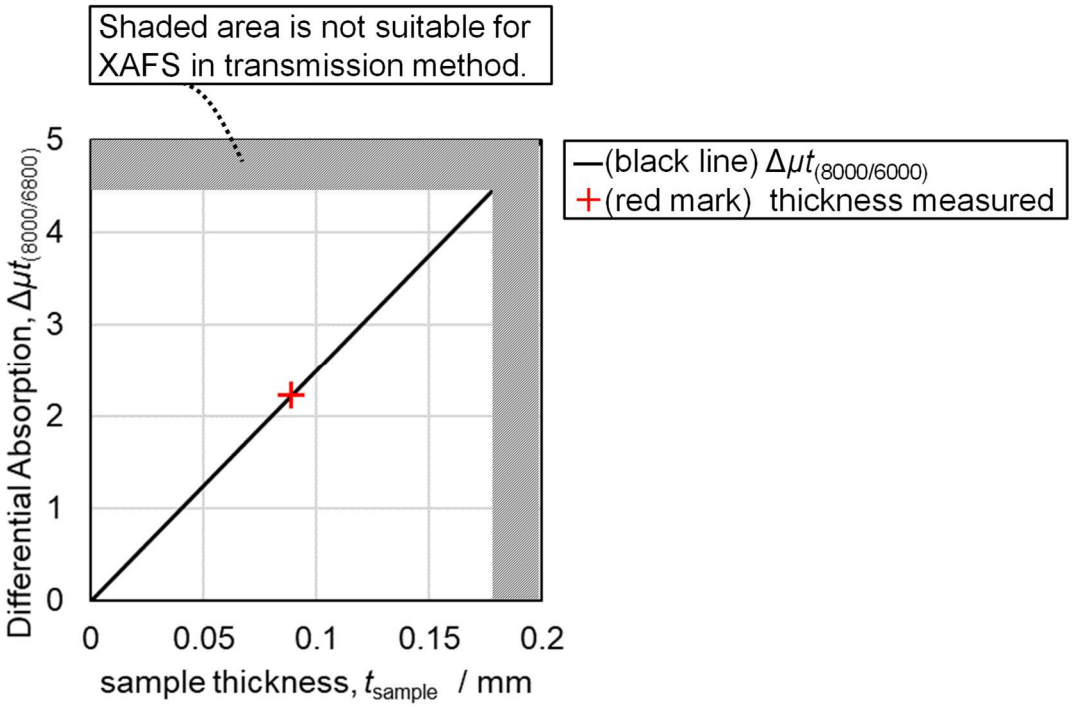

Figure 3.6 Effect of Cu-0.53 at% Fe sample thickness on absorption μt.

Black line shows difference between μt at 8000 eV and μt at 6800 eV.

Shaded area is not suitable for transmission XAFS because of too large $\Delta\mu t_{(8000/6800)}$.

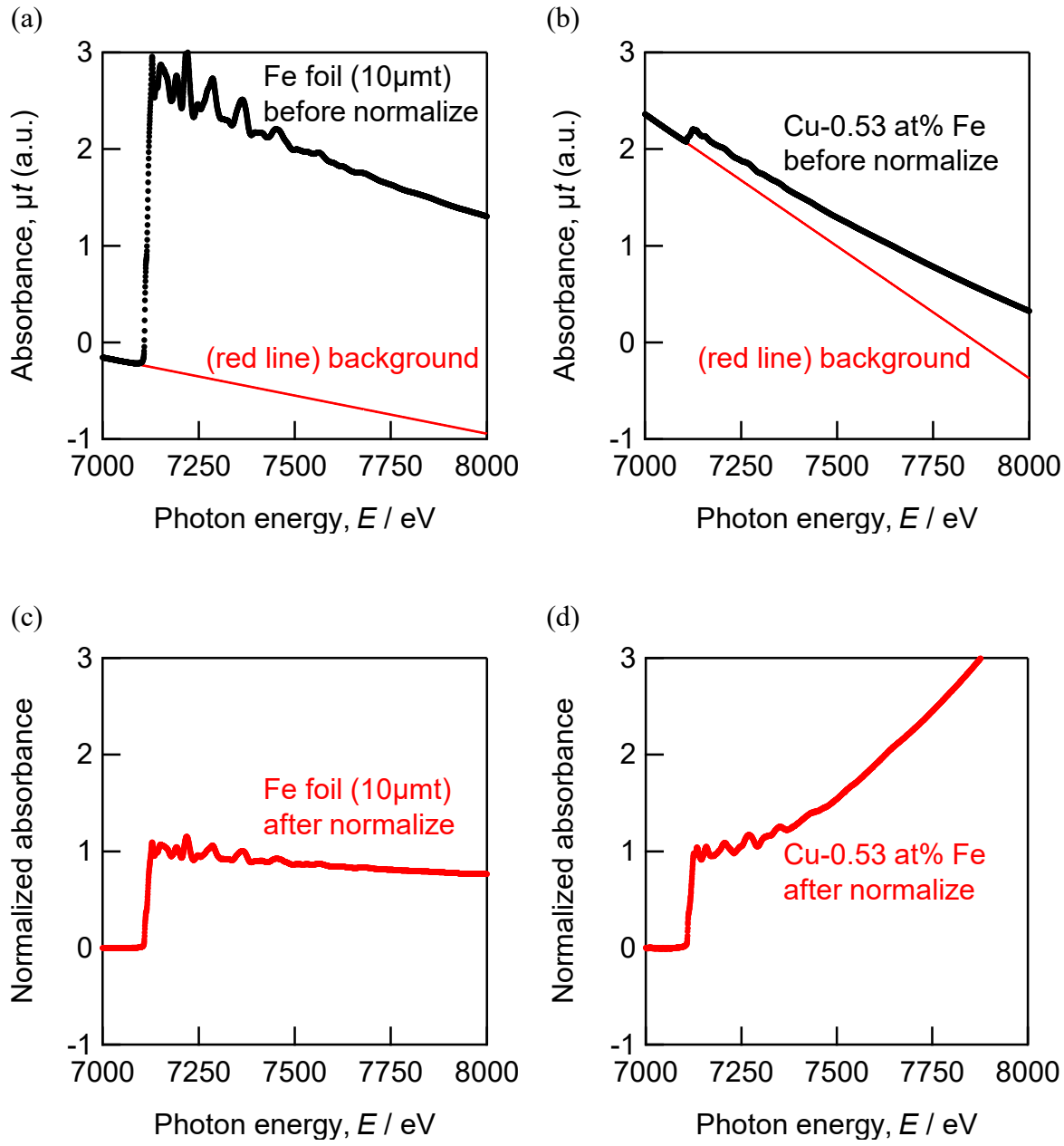

Figure 3.7 Typical Fe-K edge XAFS by the transmission method.

(a) Absorbance μt and background line of Fe foil.

(b) Absorbance μt and background line of Cu-0.53 at% Fe thinned to be 0.089 mm.

(c) Normalized absorbance of the specimen same with (a).

(d) Normalized absorbance of the specimen same with (b)

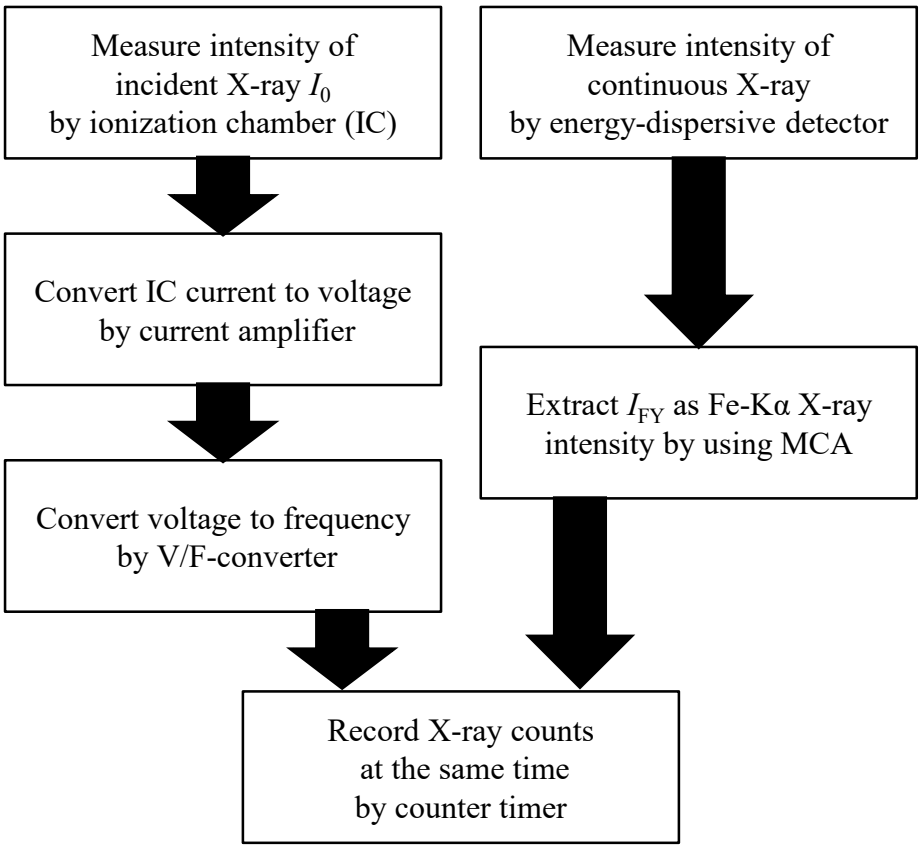

Figure 3.8 Ordinary XAFS measurement flow of the fluorescence method.

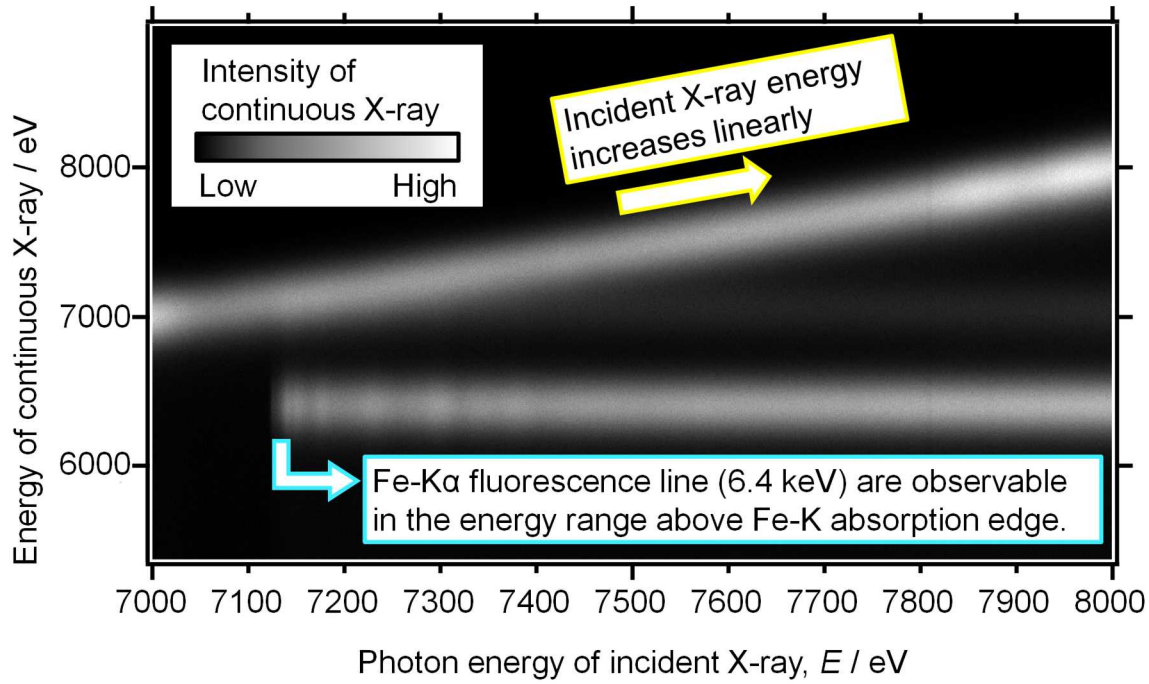

Figure 3.9 Intensity mapping of continuous X-ray emitted from specimen.
Vertical axis is the energy of X-ray emitted from specimen
Horizontal axis is photon energy of the X-rays irradiated to the sample.

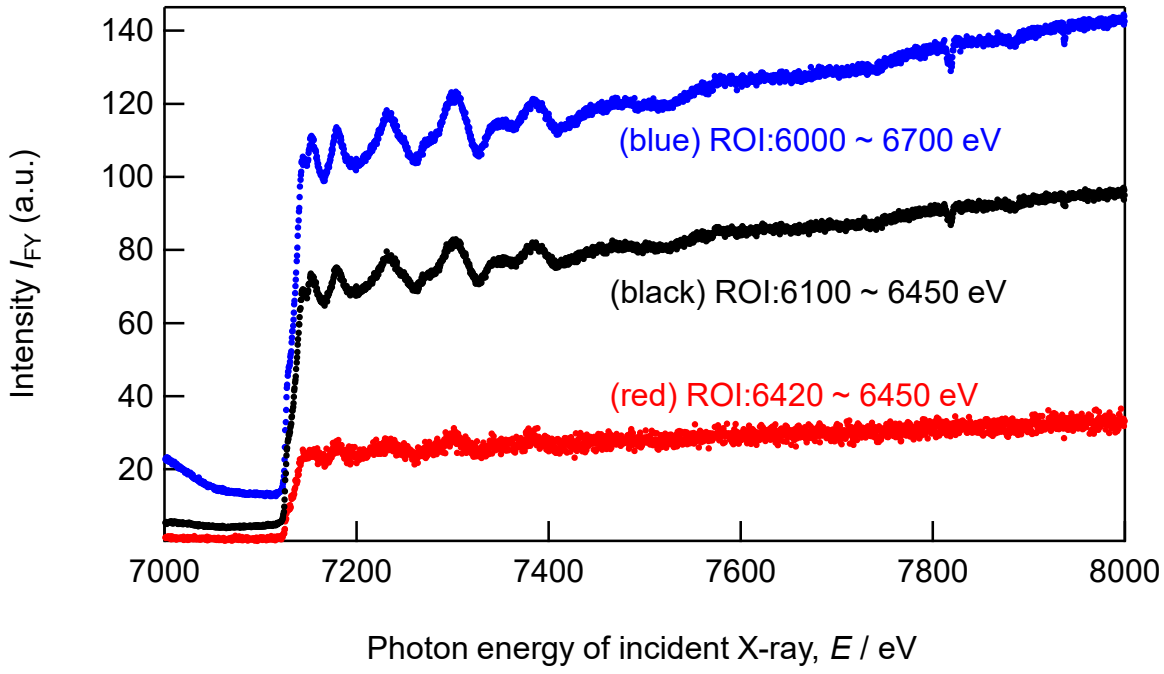

Figure 3.10 Fluorescent X-ray intensity dependence on photon energy of incident X-ray.
Three spectra show different appearance due to different ROI window settings.

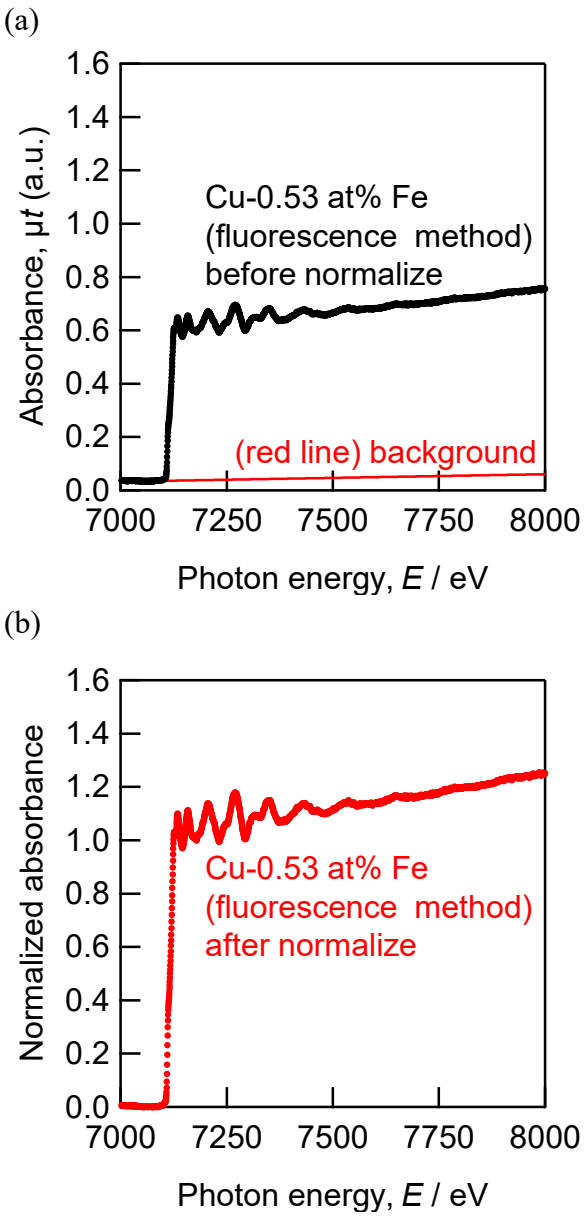

Figure 3.11 Typical Fe-K edge XAFS by the fluorescence method.

(a) Absorbance μt and background line of Cu-0.53 at% Fe.

(b) Normalized absorbance of Cu-0.53 at% Fe per one Fe atom.

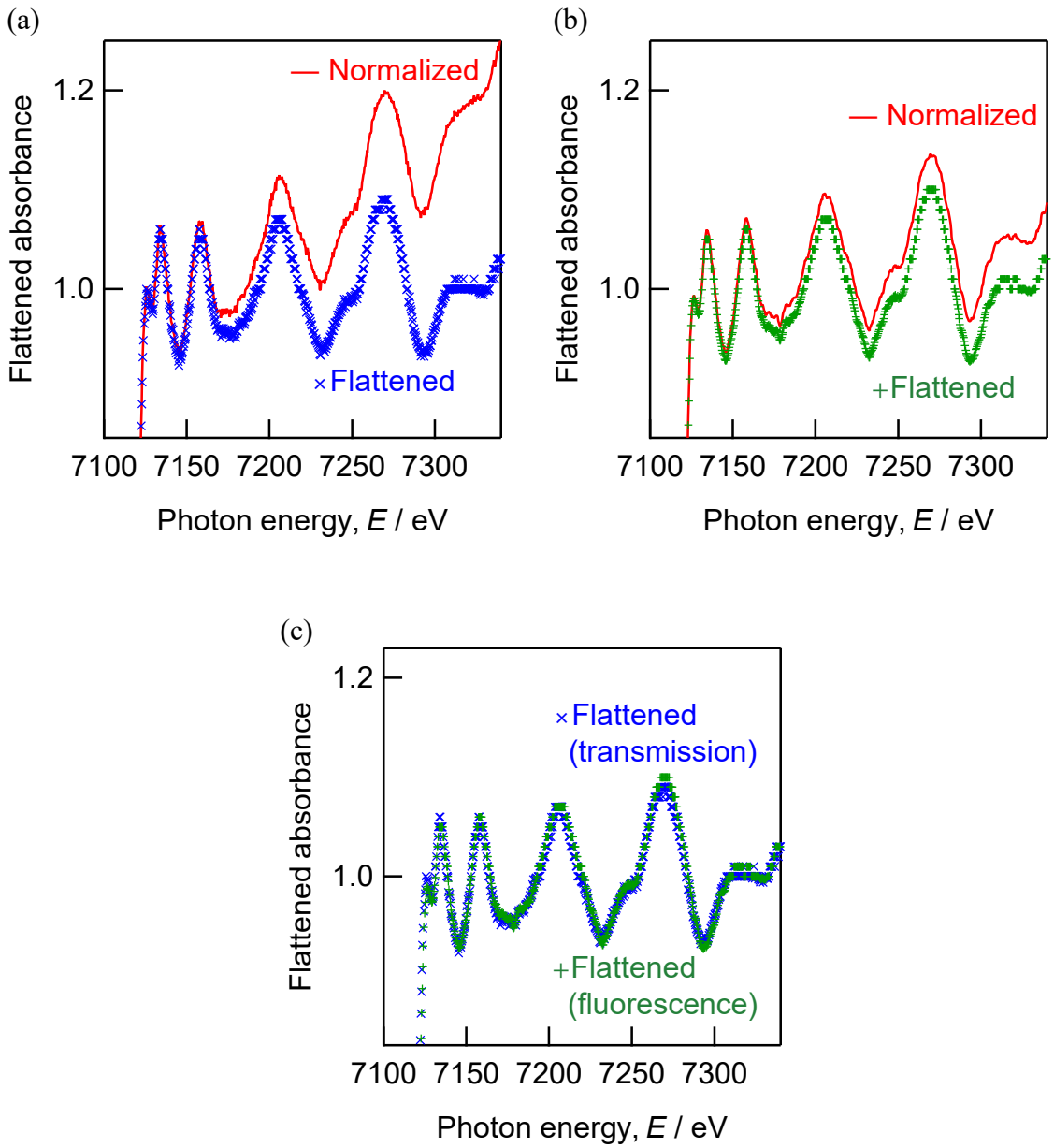

Figure 3.12 Comparison of Fe-K edge XAFS spectra before and after flattened.

(a) XAFS spectra by transmission method.

(b) XAFS spectra by fluorescence method.

(c) Comparison of the flattened absorbance plotted in (a), (b).

3.3. Results and discussion

3.3.1 XRD and crystal structure analysis in Cu-0.53 at% Fe ultrafine wire

Figure 3.13 shows XRD patterns obtained from four ultrafine wires comparing the effect of aging heat treatment. The main diffraction peaks are attributed to FCC-Cu, and aging temperature hardly affected the peak positions. The lattice constant (a) was calculated according to extrapolation functions originated by Nelson and Riley [43]. The function used here is defined as the following equation (3.5), where θ is a bragg angle.

$$a = \frac{1}{2}\left\{\left(\frac{\cos^2\theta}{\sin\theta}\right) + \left(\frac{\cos^2\theta}{\theta}\right)\right\} \qquad \text{Equation (3.5)}$$

Table 3.2 shows calculated lattice constants which were not significantly different from pure copper (0.3615 nm) in the previous studies [44, 45].

The ultrafine wire D5 with the highest aging temperature showed a weak peak attributed to BCC-Fe, with a lattice constant of 0.2863 nm determined from the 110 reflection of Fe, which is slightly smaller than the reported value for pure iron (0.2865 nm) [46]. It is known that the lattice constant follows the Vegard rule for dilute iron alloys, and given reports that solid solution Cu in α-Fe has the effect of expanding the lattice volume [47, 48], the difference in lattice constant was not considered to be owing to solid solution Cu. However, since the wire drawing process introduced significant strain, it is possible that the shift was caused by the internal stress.

The intensity ratios of each hkl indices with the 111 reflection intensity of copper as 100 differ widely from the theoretical intensity ratio as shown in Table 3.3. Comparing the 111&222 peaks with the 200&400 peaks, it can be seen that the intensity ratios of the peaks with parallel crystal planes have a similar relationship to that of the ideally non-oriented case. Based on the results above, this change in reflection intensity ratio could be attributed to the development of a so-called "deformation texture" as a result of the wire drawing process.

The integral breadth, β observed from each peak of all specimens showed only little difference regardless of the isothermal aging temperature. Here, the microstrain in a metal [49, 50], ε can be determined using the observed peak position and the observed integral breadth according to the Williamson-Hall method [51, 52]. It is known by the following equation (3.6), where θ is the Bragg angle, λ is the X-ray wavelength (0.0496 nm) and D is the crystallite size. Note that β is calculated in radians, not degrees.

$$\beta = A\varepsilon\tan\theta + \frac{K\lambda}{D\cos\theta} \qquad \text{Equation (3.6)}$$

Table 3.4 shows calculated ε of each specimen, when the two proportional constants, A and K are set to 4 and 1, respectively. All of the four ultrafine wires indicated almost same in the value of ε, and were consistent with the fact that their tensile strength showed no significant differences as previously discussed in Section 2.3.2. The analysis of XRD profiles using the Williamson-Hall method is known to be very powerful for investigating the change of microstructure due to deforming in FCC metals [53]. In this study, XRD analysis successfully revealed changes in Cu and Fe crystalline phases in Cu-0.53 at% Fe ultrafine wires with a high working ratio of $\eta = 9.5$ (0.05 mm diameter). No significant differences microstrain ε of Cu matrix were observed, but α-Fe was detectable only when aging heat treatment was performed at 873 K prior to drawing.

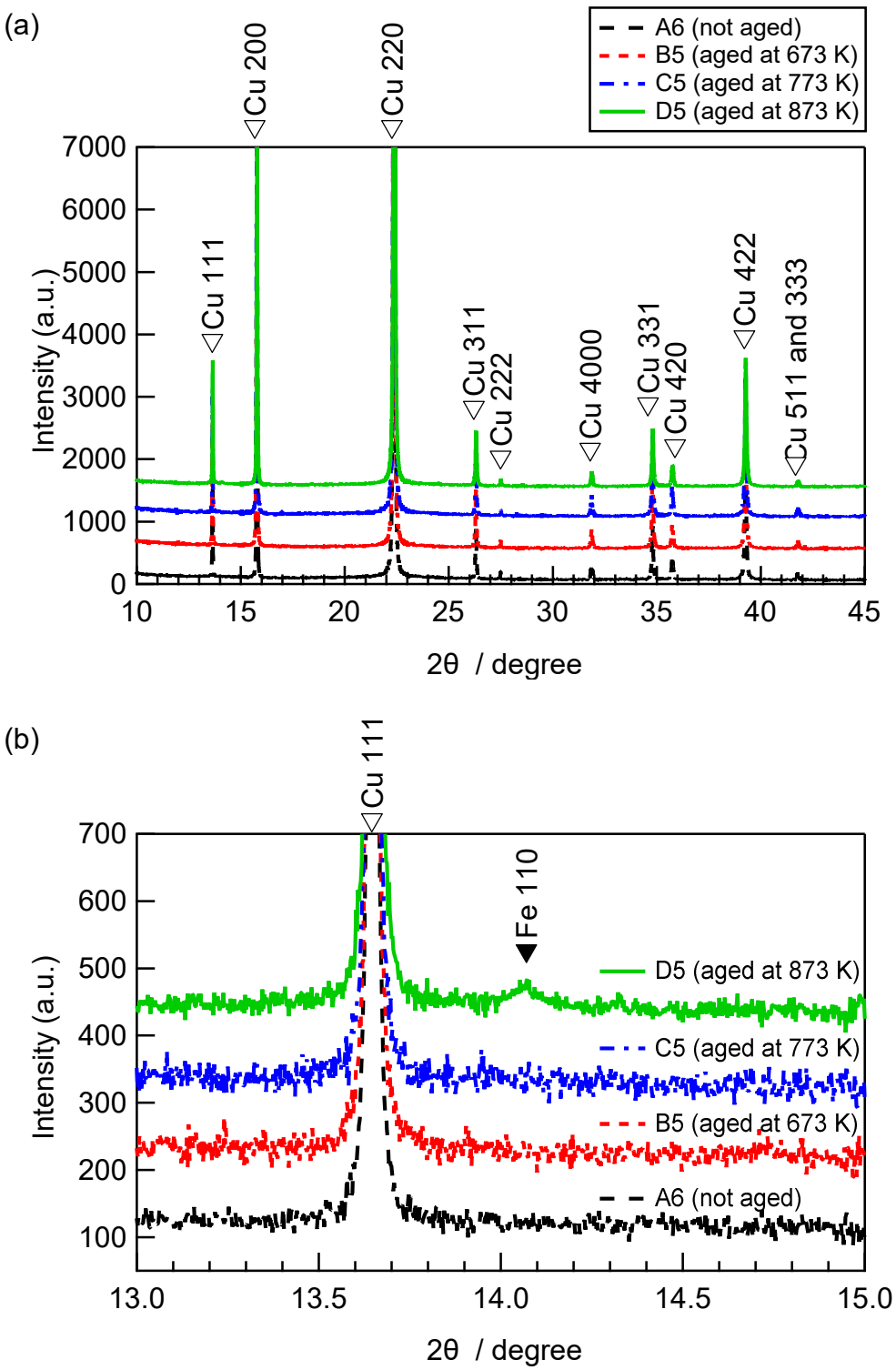

Figure 3.13 XRD profile of ultrafine wires (0.05 mm diameter).

(a) Profile in wide 2θ rage (10°~45°), showing the peaks of Cu matrix.

(b) Partially enlarged 2θ range (13°~15°), Fe 110 reflection observable.

Table 3.2 Lattice constant of Cu phase and Fe phase detected from each specimen.

Sample name	FCC-Cu phase	BCC-Fe phase (α-Fe)
A6	a = 0.3615(1) nm	- (not detected)
B5	a = 0.3616(1) nm	- (not detected)
C5	a = 0.3616(1) nm	- (not detected)
D5	a = 0.3615(1) nm	a = 0.2863 nm

Table 3.3 X-ray diffraction intensity ratio measured from the specimen A6 and calculated.

Miller indices hkl	Intensity ratio measured	Intensity ratio calculated
111	100	100
200	648	44
220	4665	21
311	112	20
222	8	7
400	52	4

Table 3.4 Result of XRD profile analysis.

The subscript numbers correspond to the Miller indices of corresponding lattice planes.

Sample name	$2\theta_{200}$	β_{200}	$2\theta_{400}$	β_{400}	Microstrain, ε
A6	15.781°	0.0638°	31.870°	0.1270°	0.187 %
B5	15.781°	0.0661°	31.872°	0.1280°	0.183 %
C5	15.779°	0.0635°	31.870°	0.1248°	0.182 %
D5	15.783°	0.0660°	31.878°	0.1298°	0.189 %

3.3.2 TEM observation of Fe precipitates in Cu-0.53 at% Fe ultrafine wire

In the previous section 3.3.1, XRD comparison of the four ultrafine wires showed that α-Fe was detected only at the aging temperature condition of 873 K (named D5). In this section, two of these, 873 K (D5) and 773 K (C5), were both compared by TEM observations.

Figure 3.14 (a) and (c) shows ABF-STEM images obtained from the ultrafine wires C5 and D5, respectively. Figure 3.14 (b) and (d) shows HAADF-STEM images of the same. Both of them show lamellar microstructures with thicknesses of approximately 100~600 nm, although it is difficult to determine exactly because of the overlap of multiple grain boundaries in the depth direction. The microstructure of Cu matrix was found to be very fine grained and was elongated along with the wire drawing direction.

Figure 3.15 shows the HAADF-STEM image and EDX elemental mapping of Cu and Fe. The intensity contrast in the HAADF-STEM image, which has the possibility to reflect the elemental contrast, was not affected by the Fe concentration by comparing with the EDX results. Although several areas with high Cu intensity were observed, the Fe intensity was also high in those locations, which was attributed to the non-uniform thickness of the thin TEM specimens generated during the FIB machining process. The change in brightness of the STEM image is thought to be due to dislocations and other crystal defects.

Figure 3.16 shows the BF-STEM image with different tilt angles for comparison. Tilting the thin TEM specimen by only 3 degrees drastically changed the appearance of dislocations, so dislocations are assumed to be uniformly distributed throughout the TEM specimen. This seems to be appropriate given that working ratio $\eta = 9.5$ is a very high value. Next, the same specimen's image observed at high magnification is shown in Figure 3.17. The intensity contrast of the STEM image alone could not identify Fe precipitates due to the large number of dislocations, but the EDX intensity distribution clearly showed that the Fe intensity was enhanced in areas where the Cu intensity was weak. Fe particles were found to be mainly spherical or elliptical in the Cu matrix. Some Fe particles found by EDX were scattered elongated along the direction of wire drawing, as indicated by the light blue square dotted lines in the Figure 3.17 (c). This suggests that the Fe particles produced by aging precipitation may have been stretched along with the wire drawing direction or may have been mixed with Cu atoms. The size of Fe particles, as far as can be discriminated by EDX elemental intensities, had been fractured into nanometer-sized. To find these fine particles, the field of view had to be narrowed to accommodate the high magnification required, and as shown in Figure 3.17, the field of view was only 850 nm square.

STEM-EDX observation succeeded in finding nanometer-sized Fe precipitates. However, since the image is a projection onto a two-dimensional surface, the three-dimensional shape elongated along the wire drawing direction is not known at all. The concentration profile at the interface between Cu and Fe cannot be clarified by EDX due to the sensitivity of the elements. In the following section, we discuss the results of an analysis using 3D-APT, which has spatial resolution equivalent to or better than STEM-EDX and much higher sensitivity in detecting elements, with the aim of visualizing such a distribution of Fe precipitates.

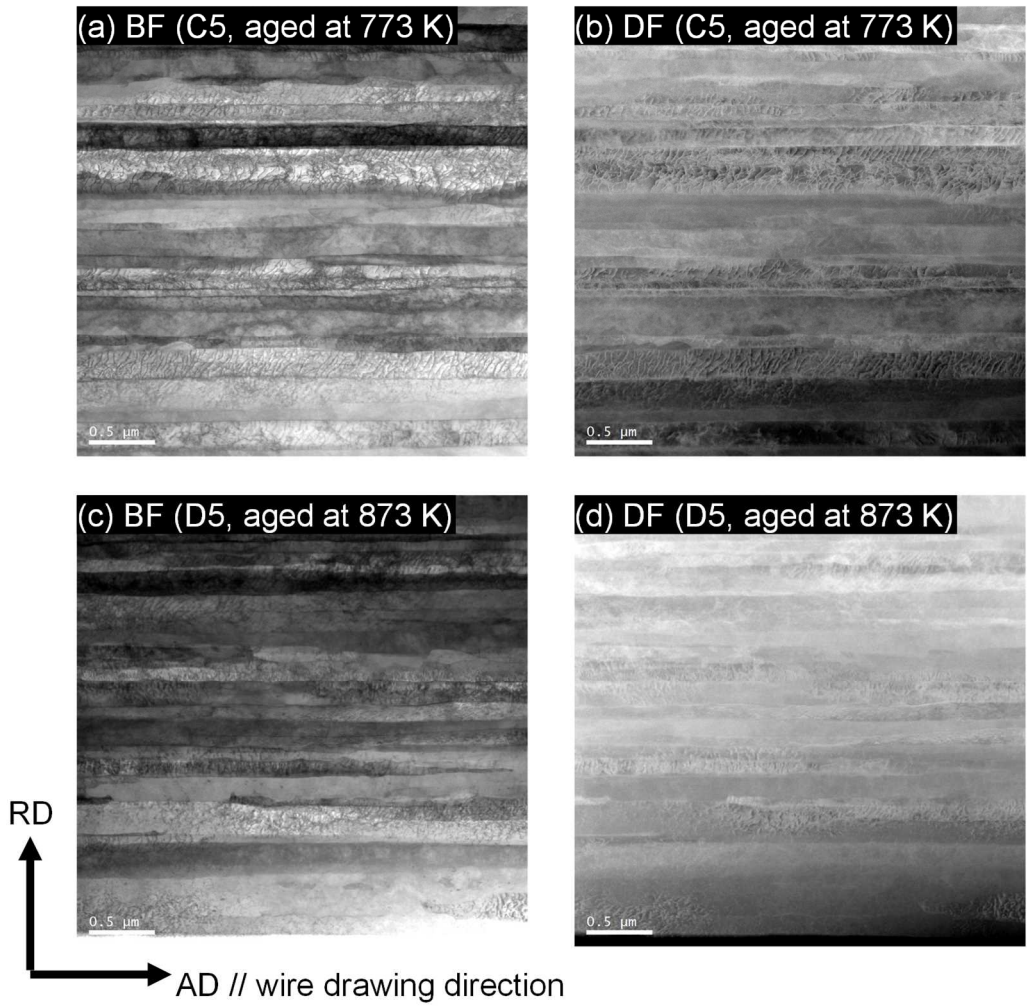

Figure 3.14 STEM images of ultrafine wire specimen of Cu-0.53 at% Fe.

(a) BF-STEM image of C5 (aged at 773 K followed by wire drawing).

(b) DF-STEM image of C5 (same as above).

(c) BF-STEM image of D5 (aged at 873 K followed by wire drawing).

(d) DF-STEM image of D5 (same as above).

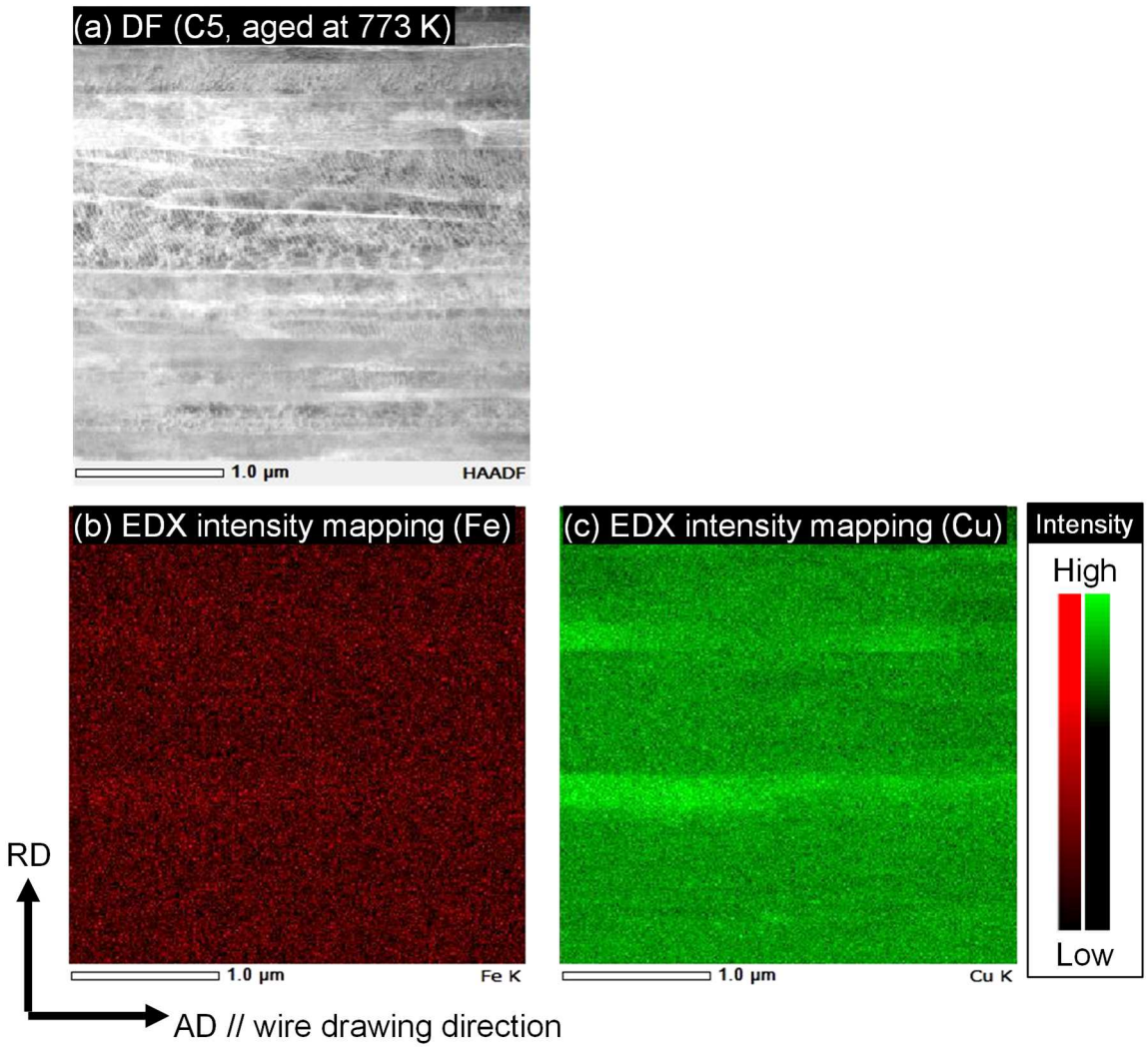

Figure 3.15 Images of STEM and EDX elemental mapping obtained from ultrafine wire C5 (aged at 773 K followed by wire drawing).

(a) DF-STEM image of C5 (aged at 773 K followed by wire drawing)

(b) EDX intensity mapping of Fe.

(c) EDX intensity mapping of Cu.

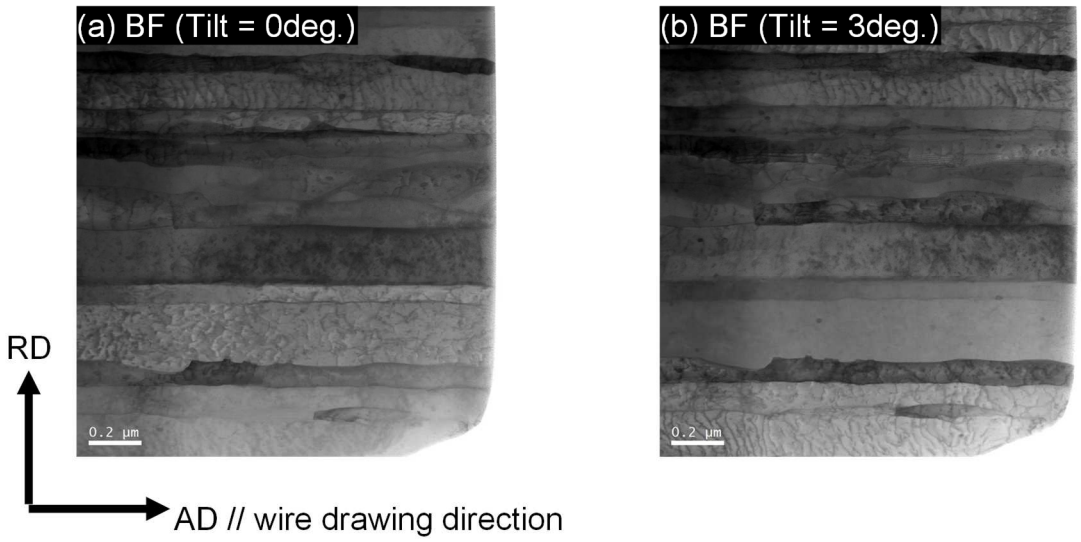

Figure 3.16 BF-STEM images of specimen D5 (aged at 873 K followed by wire drawing). Two images show different dislocations visible at different tilts.

(a) BF-STEM image of D5 at the tilt angle of 0 deg.

(b) BF-STEM image of D5 at the tilt angle of 3 deg.

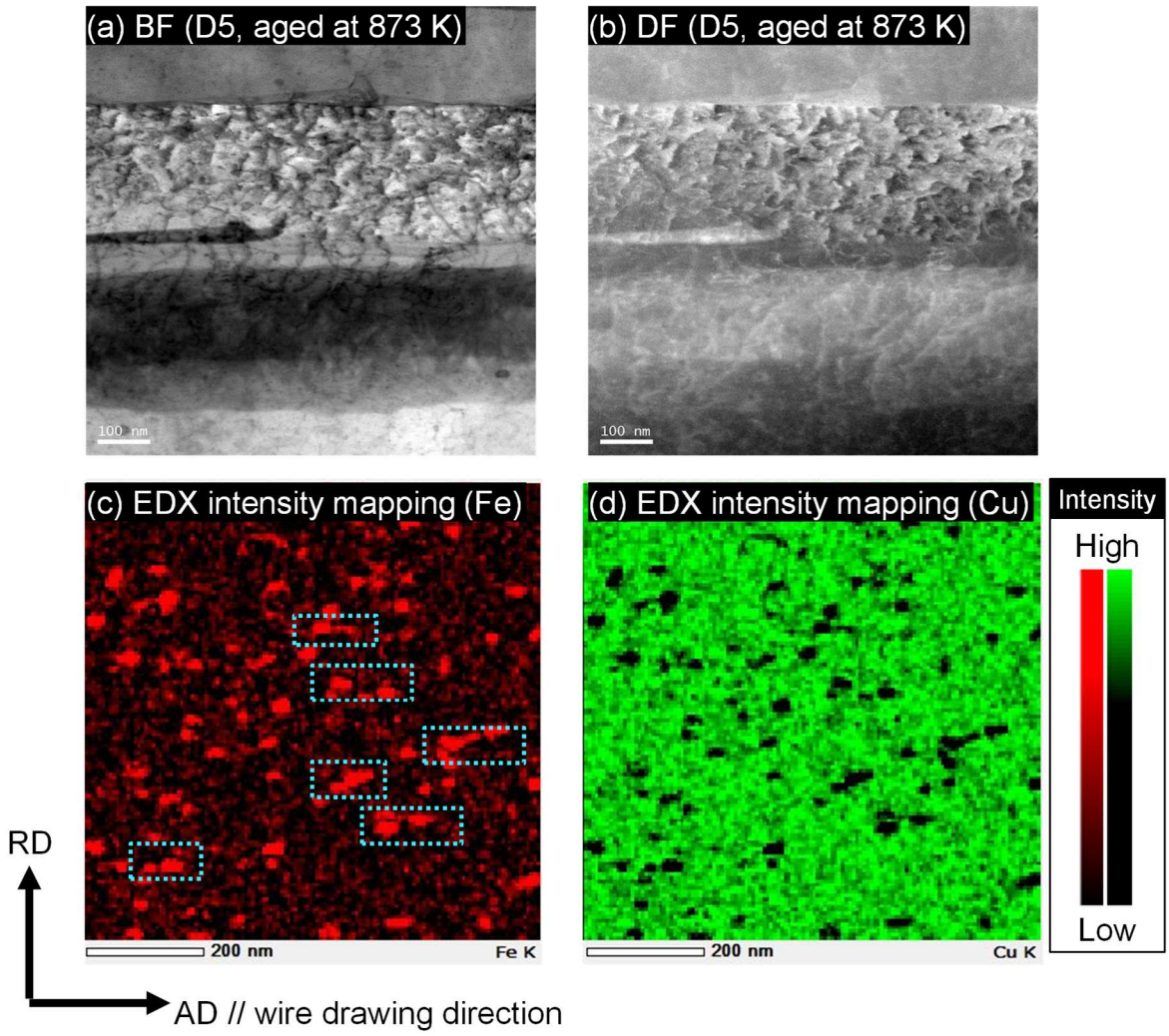

Figure 3.17 Images of STEM and EDX elemental mapping of ultrafine wire specimen D5 (aged at 873 K followed by wire drawing). (a) BF-STEM image of D5. (b) DF-STEM image of D5. (c) EDX intensity mapping of Fe. (d) EDX intensity mapping of Cu. The light blue dotted squares indicate Fe particles elongated along the AD direction.

3.3.3 3D-APT analysis of Cu-0.53 at% Fe ultrafine wire

Figure 3.18 and Figure 3.19 show the four atom maps obtained from two data sets from a ultrafine wire C5 (aged at 773 K) and two from the other wire D5 (aged at 873 K), respectively. The distribution of Fe atoms existing in the longitudinal direction was observed in C5, especially in dataset of C5_573 (Figure 3.18 (b)), indicating that aggregates containing Fe were aligned as dots in the longitudinal direction. In the ultrafine wire D5 (aged at 873 K), unlike C5 (773 K) described above, the Fe concentration distribution shows a unique form. Figure 3.19 shows 3D-APT results of D5 indicating that the Fe concentration distribution is not only arranged in a dot-like pattern, but also longitudinally connected to a certain extent. While these elongated fibrous Fe were estimated to be about 4 nm in diameter, their lengths were at least 100 nm or more, extending beyond the ends of the field of view (Figure 3.19 (a) and (b)). Considering that this ultrafine wire D5 had already been drawn to a working ratio of $\eta = 9.5$ (from 5.8 mm to 0.05 mm in diameter), it is quite natural to assume that these elongated Fe concentration distributions were mainly formed by the wire drawing. Comparing before and after drawing, the diameter was reduced by a factor of 100, suggesting that the aging precipitates, which were several tens of nm in size, may have been reduced to less than 1 nm in diameter. However, since the diameter appears on the atom map to be about 4 nm, the following analysis was performed on the isoconcentration surface. Table 3.5 shows the atomic composition ratios obtained from 3D-APT analysis, which are in good agreement with those obtained by inductively coupled plasma atomic emission spectroscopy already shown in Table2.2.

Figure 3.20 shows the isoconcentration surfaces of 4 at% Fe and 93 at% Cu. The figures upside are presented for ultrafine wire C5 (aged at 773 K) and downside for D5 (aged at 873 K). The pair of isoconcentration surfaces obtained from the same specimen show almost the same spatial distribution, suggesting that interdiffusion occurs at the interface between the Fe precipitates and the Cu matrix.

To examine the interface between the fibrous Fe phase and the Cu matrix, the interface concentration gradient was evaluated by proxigrams. Figure 3.21(b) shows the proxigram obtained from the analyzed region specified in Figure 3.21(a). Spherical isoconcentration surfaces were observed from the specimen of C5. For another specimen of D5, Figure 3.22(b) also shows the proxigram obtained from the analyzed region specified in Figure 3.22(a). Spherical isoconcentration surfaces were observed from D5. The isoconcentration surfaces of C5 and D5 were found to have completely different shapes. When an interface of Cu-4 at% Fe concentration was set as the reference interface for calculating the proxigram, at the interface

of Cu matrix and Fe precipitate found in both of the two ultrafine wires C5 and D5, the Fe concentration increases up to about 40 at% from the reference interface to 2 nm inward. The nm-order alloying of Cu and Fe could be considered to occur regardless of isoconcentration surface shapes. Since the amount of cold working imposed to these wires is the same, this result is consistent with the idea that the Fe precipitates were fragmented by the wire drawing after aging treatment. And the fact that a large discrepancy in electrical resistivity occurred between C5 and D5 (despite no significant difference in tensile strength) may be due to the difference in the degree of Fe particle fragmentation by the wire drawing process.

In the previous section, although nanometer-sized Fe particles of were found by TEM observation, the concentration profile at the interface between Cu and Fe could not be clarified by EDX. 3D-APT analysis can successfully find out the three-dimensional concentration distribution of Fe because of its high sensitivity to the elements. 3D-APT was a suitable analytical method in this case, because Cu and Fe hardly disturb each other's signals. For example, low concentration Fe cannot be detected in Al matrix due to the overlapping signals of the elements, which is as important as Cu for industrial electric wires, but low concentration Fe in Cu is easily detectable.

Since 3D-APT has the narrow analytical fields of view, an additional study about the coarsened Fe precipitates in thick Cu-Fe wires was performed by small-angle scattering using a neutron beam in the next section.

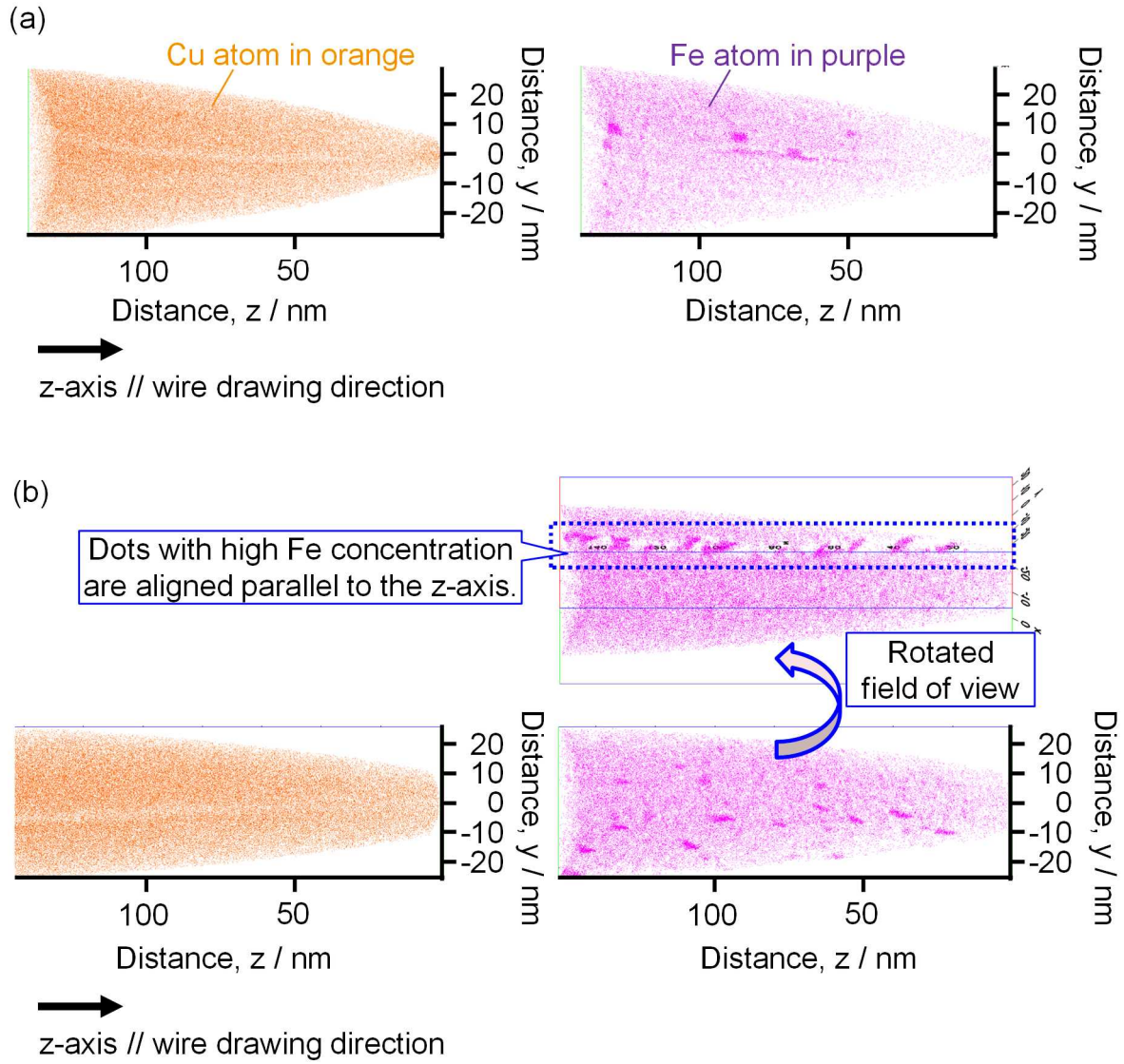

Figure 3.18 3D-APT results of ultrafine wire specimen C5.

C5 was aged at 773 K followed by wire drawing.

The Z direction is parallel to wire drawing direction.

(a) Atom map of C5_574 (one data obtained from C5).

(b) Atom map of C5_573 (the other data obtained from C5).

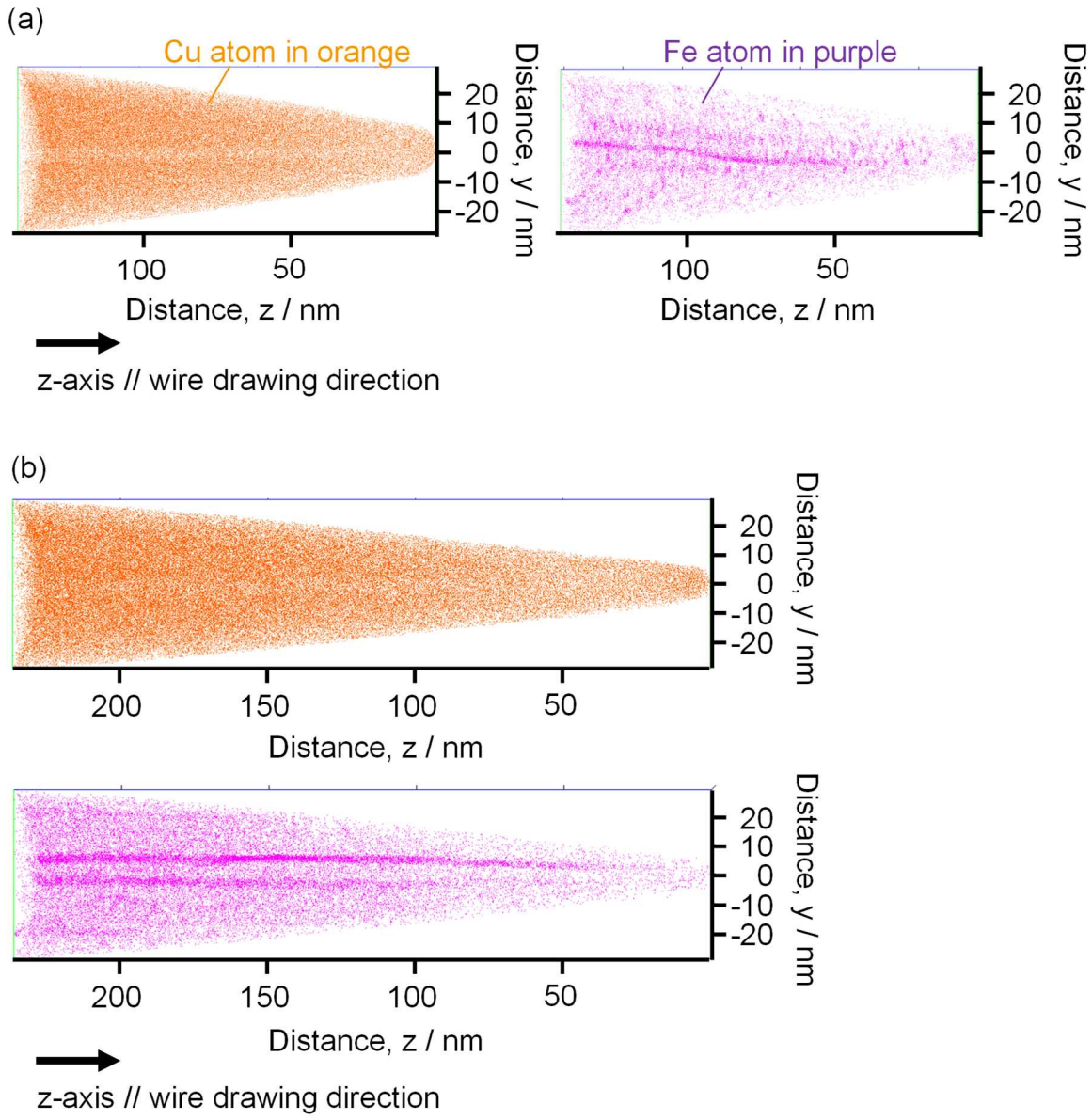

Figure 3.19 3D-APT results of ultrafine wire specimen D5.

D5 was aged at 873 K followed by wire drawing.

The Z direction is parallel to wire drawing direction.

(a) Atom map of D5_605 (one data obtained from D5).

(b) Atom map of D5_607 (the other data obtained from D5).

Table 3.5 Atomic composition ratios obtained by 3D-APT analysis.

Sample name and data number	Composition ratio (at%)				
	Fe	P	S	Cu	Ga
C5_574	0.38	- *	- *	99.61	0.01
C5_573	0.76	0.01	0.01	99.20	0.02
D5_605	0.62	- *	0.01	99.34	0.03
D5_607	0.35	- *	0.01	99.62	0.01

(* Below limit of quantification.)

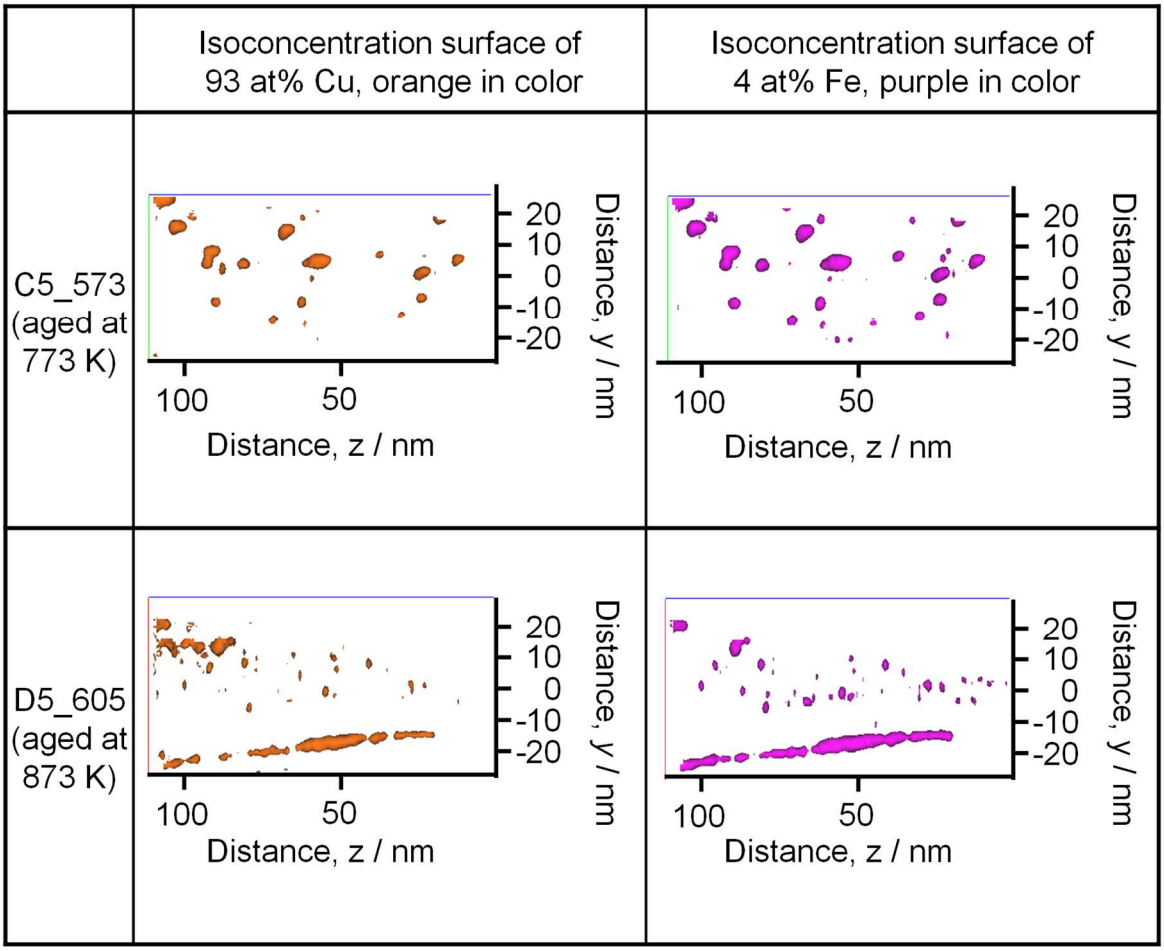

Figure 3.20 Isoconcentration surfaces of 93 at% Cu and 4 at% Fe obtained from Cu-Fe ultrafine wires aged at different temperatures followed by wire drawing.

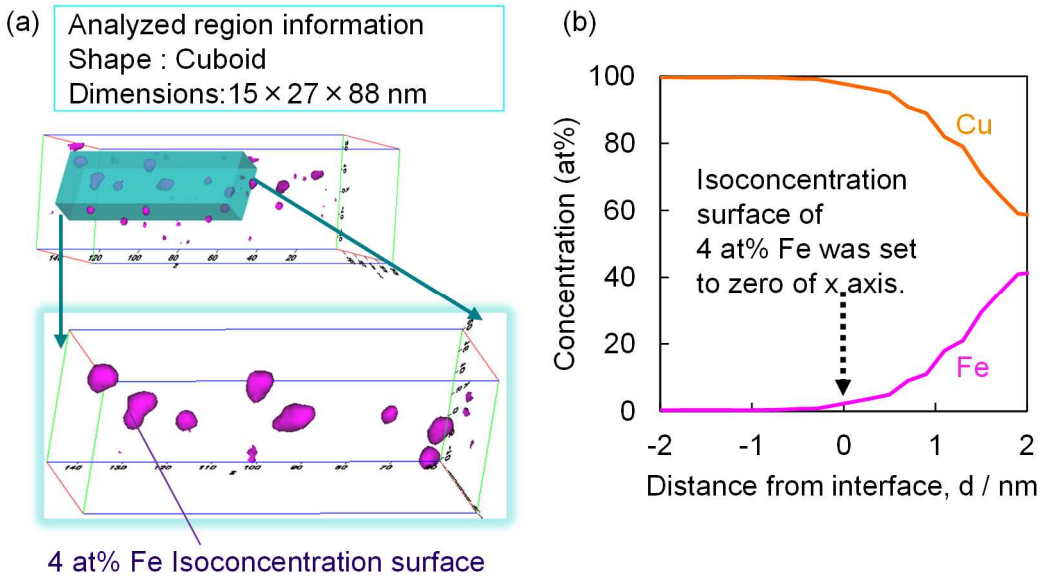

Figure 3.21 Isoconcentration surface and proxigram of C5_573 (aged at 773 K).

(a) Analyzed region and isoconcentration surface.

(b) 1-D average composition profile (proxigram) nearby Cu/Fe interface.

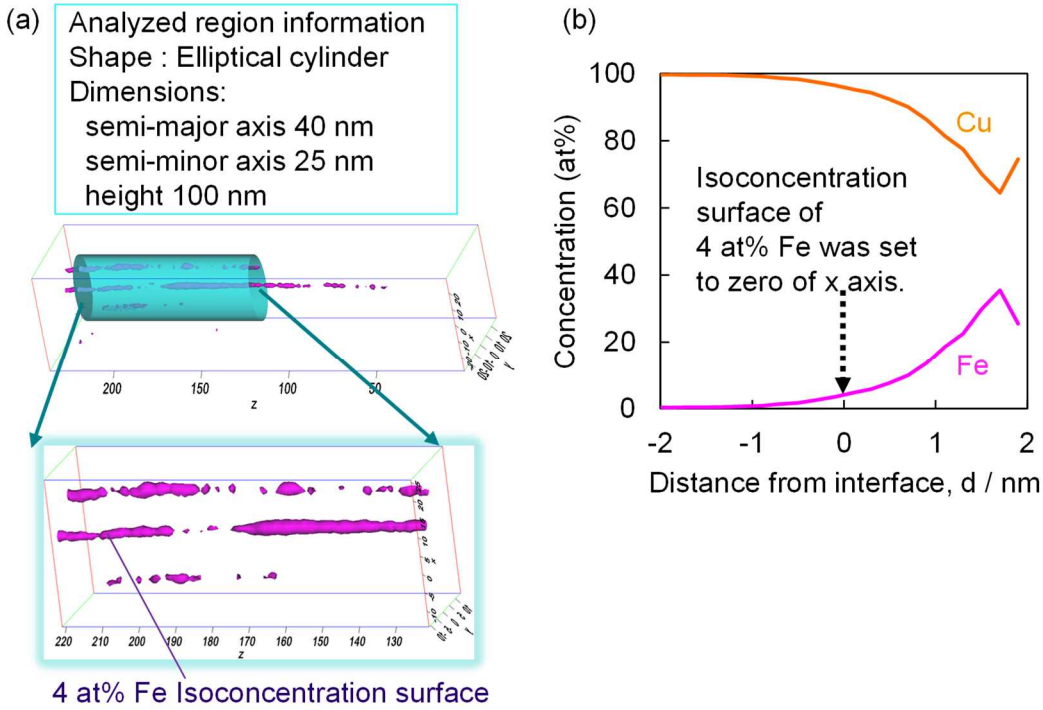

Figure 3.22 Isoconcentration surface and proxigram of D5_605 (aged at 873 K).

(a) Analyzed region and isoconcentration surface.

(b) 1-D average composition profile (proxigram) nearby Cu/Fe interface.

3.3.4 Analysis of Fe precipitates size by SANS and TEM

Figure 3.23 (a) shows SANS profiles obtained from a 5.8 mm diameter Cu-0.53 at% Fe wire (D0) aged at 873 K for 8h. The 1-D profiles were obtained in the wide q-range of 0.07 nm^{-1} to 43 nm^{-1}. The 1-D profiles integrated in the vertical and horizontal directions of the 2-D detector did not show significant difference. Figure 3.23 (b) is a partially enlarged profile of Figure 3.23(a), and the two sharp peaks in the range of 28 nm^{-1} to 35 nm^{-1} were corresponding to the bragg diffraction of the Cu matrix. The relationship between q (in nm^{-1}) and the d spacing (in nm) is expressed by the following equation (3.7), where the subscript hkl is the Miller indices.

$$q = \frac{2\pi}{d_{\mathrm{hkl}}} \qquad \text{Equation (3.7)}$$

The peak at q = 29.8 nm^{-1} corresponding to d_{hkl} = 0.21 nm which was assigned to Cu 111 reflection, and the other peak was also attributed to Cu 200 reflection.

Figure 3.24 shows a comparison among the Cu-0.53 at% Fe wires with 5.8mm diameter annealed at different aging temperatures. From the q-range of 0.07 to 0.2 nm^{-1}, each SANS profile has a straight line of the order of q^{-4} square. From the q-range of 0.2 to 0.7 nm^{-1}, the SANS profiles obtained from C0 (aged at 773 K) and D0 (aged at 873 K) show shoulders indicated by an arrow in Figure 3.24. From 673 K to 873 K, it is suggested that higher isothermal aging temperatures result in more precipitates. Higher aging temperatures indicate more precipitates, and an attempt was made to calculate the precipitates size and dispersion from the SANS profile for the highest temperature (D0, aged at 873 K). Figure 3.25 shows the STEM-EDX results for D0. The EDX intensity mapping results (Figure 3.25 (b, c)) indicate that the Fe precipitates are spherical in shape, and the manually counted histogram of the precipitate size distribution (Figure 3.25 (d)) indicates that the radius of the Fe precipitates is about 7.5 nm. Specifically, the Fe precipitates were counted from the obtained 380 nm square field of view image and EDX elemental mapping identified 37 round Fe precipitates with 15.1 nm in average diameter. This value of precipitate diameter was not so differ from the previous study about γ-Fe precipitate in Cu-0.4 at% Fe alloy [54]. The profile function obtained by fitting with an initial value of r = 7.5 nm is shown in Figure 3.26(a), along with a line proportional to the q^{-4} square and a background line. The shoulder indicated by the arrow in Figure 3.24(b), considered to be due to precipitation, corresponds to a radius of r = 4.8 nm (σ_r = 3.1). This result is not so differ from the STEM-EDX results given the large standard deviation. Figure 3.26(b) and (c) shows the SANS profiles of Cu-Fe wires aged at 873 K followed by wire drawing to 0.9 mm and 0.32 mm, respectively. The fitting function shows that r = 5.5 nm (σ_r = 0.3) for 0.9 mm diameter and r = 6.1 nm (σ_r = 0.7) for 0.32 mm diameter.

Although it is difficult to determine the size of Fe precipitates due to the large standard deviation, it can be said that the scattering intensity clearly increased after drawing. As shown in Figure 2.6, the magnetization of the Cu-Fe wire increased after drawing, suggesting that magnetic scattering by α-Fe contributed to the increase in this neutron intensity. In this measurement, it is difficult to distinguish exactly between magnetic and nuclear scattering because the measurements were made at room temperature under no external magnetic field. The precipitation of γ-Fe in Cu has been investigated by several reports [10, 55, 56, 57, 58], and the phenomenon of transformation to α-Fe after deformation has been observed by ex-situ and in-situ TEM studies [59, 60, 61, 62, 63], so the SANS results in this study were consistent with the previous studies.

The SANS profile also provided important insight into age-hardening of Cu-0.53 at% Fe wires, as already shown in Figure 2.5(a). In other words, Cu-0.53 at% Fe wires (D2 and D3) with aging temperature of 873 K followed by drawing became slightly high intense and the Fe precipitates were successfully detected from the SANS profiles. Its reasonable that the Cu-0.53 at% Fe wires of D2 and D3 showed very slightly higher tensile strength than others, because Cu-Fe alloys had been known to show less ability of age-hardening than other well-known alloys such as duralumin [64, 65, 66].

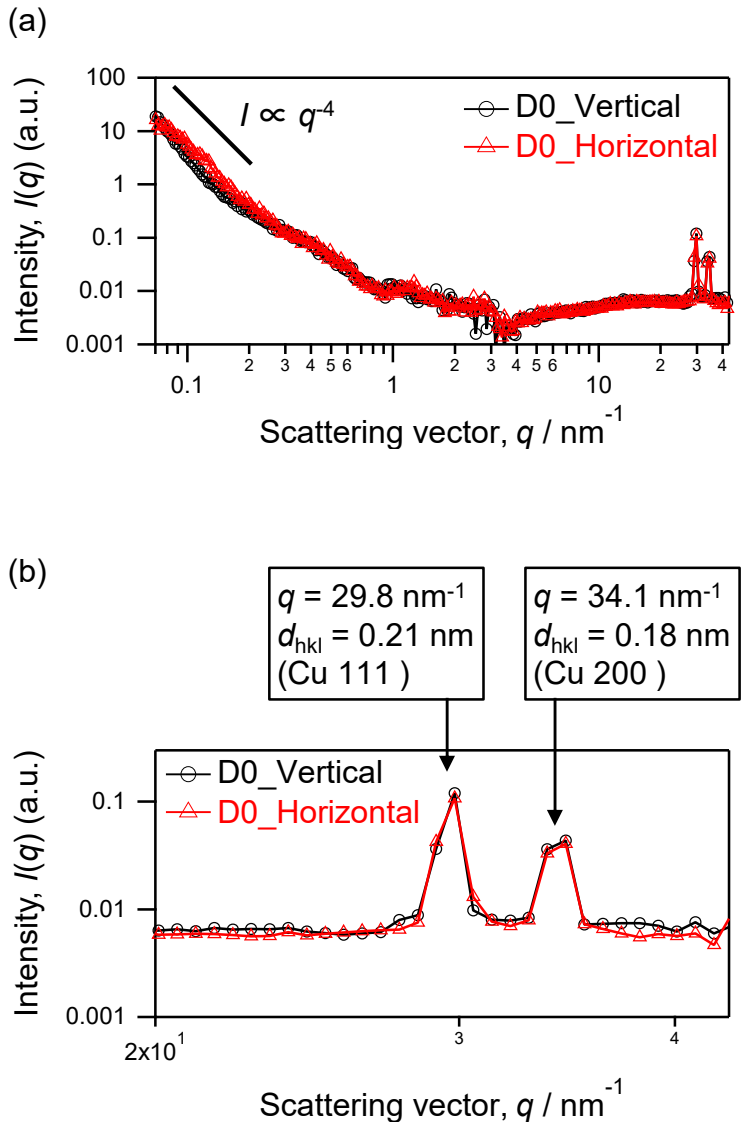

Figure 3.23 1-D SANS profile of Cu-0.53 at% Fe wire aged at 873 K, named D0. Horizontally (red) and vertically (black) integrated profiles are shown respectively.

(a) Wide q range from 0.07 to 43 nm^{-1}.

(b) Partially enlarged view with q range from 20 to 43 nm^{-1}.

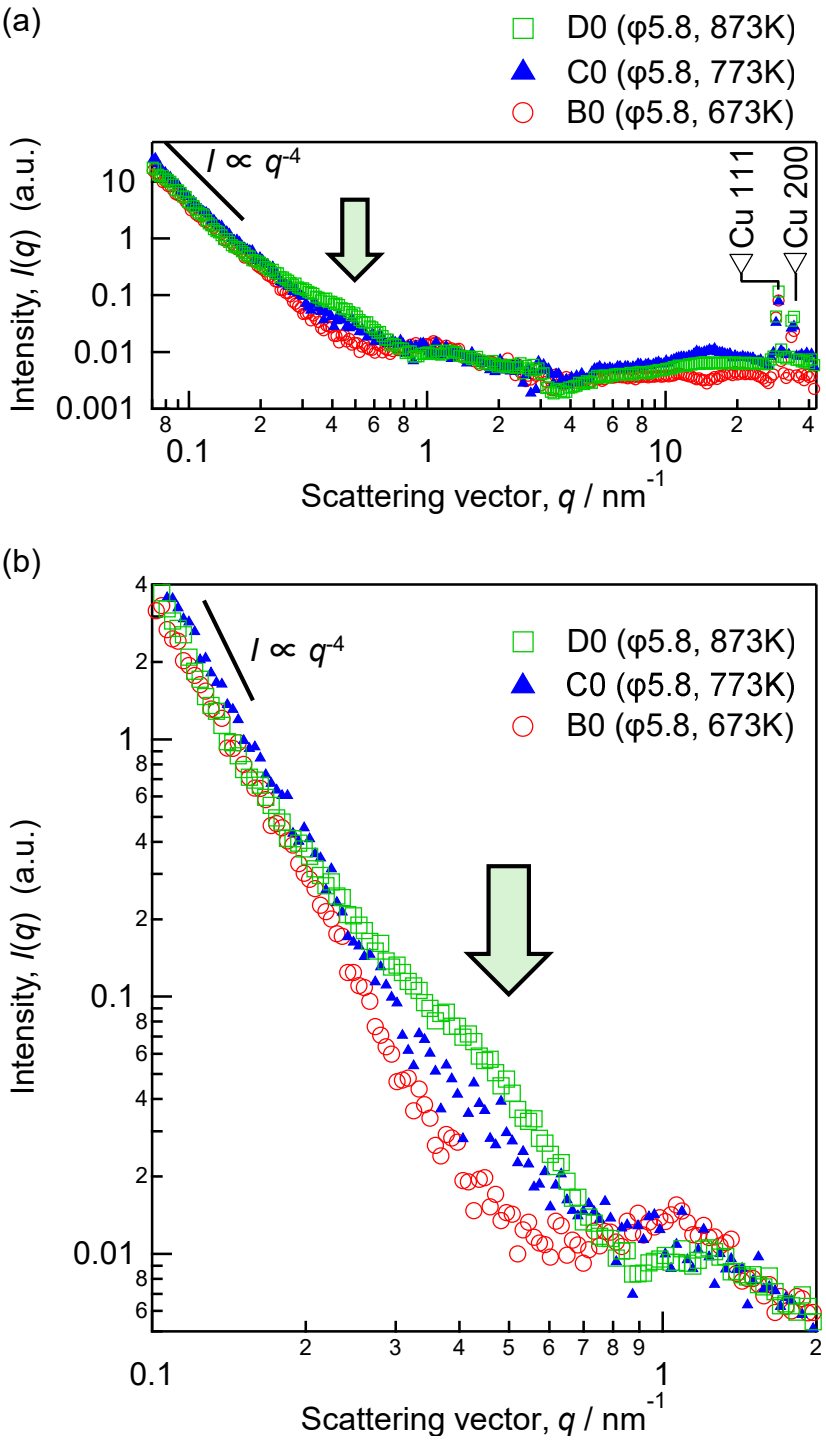

Figure 3.24 SANS profiles of Cu-0.53 at% Fe wires aged at different temperatures. Peak shoulder due to the Fe precipitates is highlighted by an arrow.

(a) Wide q range from 0.07 to 43 nm^{-1}.

(b) Partially enlarged q range from 0.1 to 2 nm^{-1}.

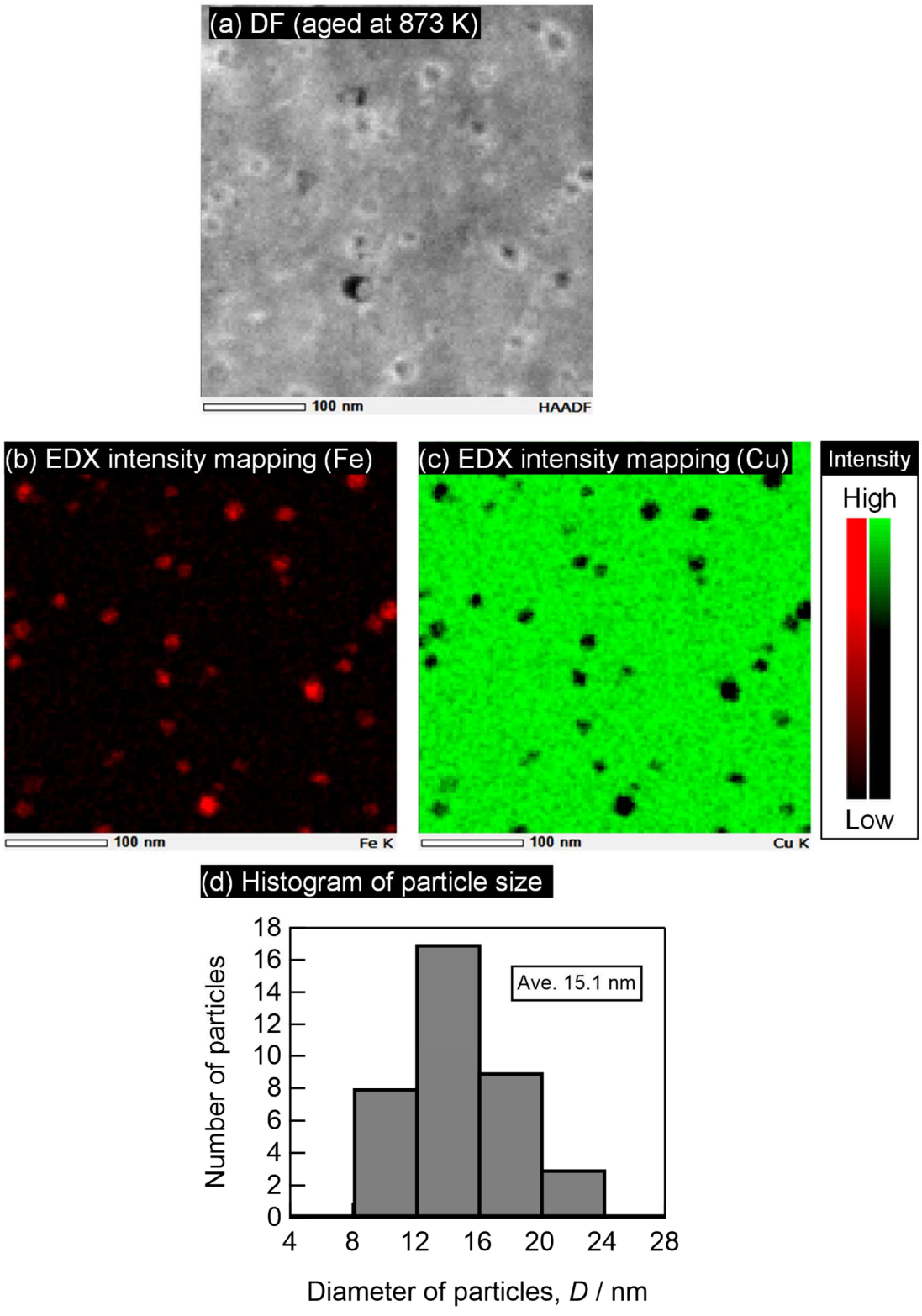

Figure 3.25 Images of STEM and EDX elemental mapping of aged Cu-Fe wire, D0.

(a) HAADF-STEM image.

(b) EDX elemental mapping of Cu

(c) EDX elemental mapping of Fe.

(d) Histogram of recognized particle sizes.

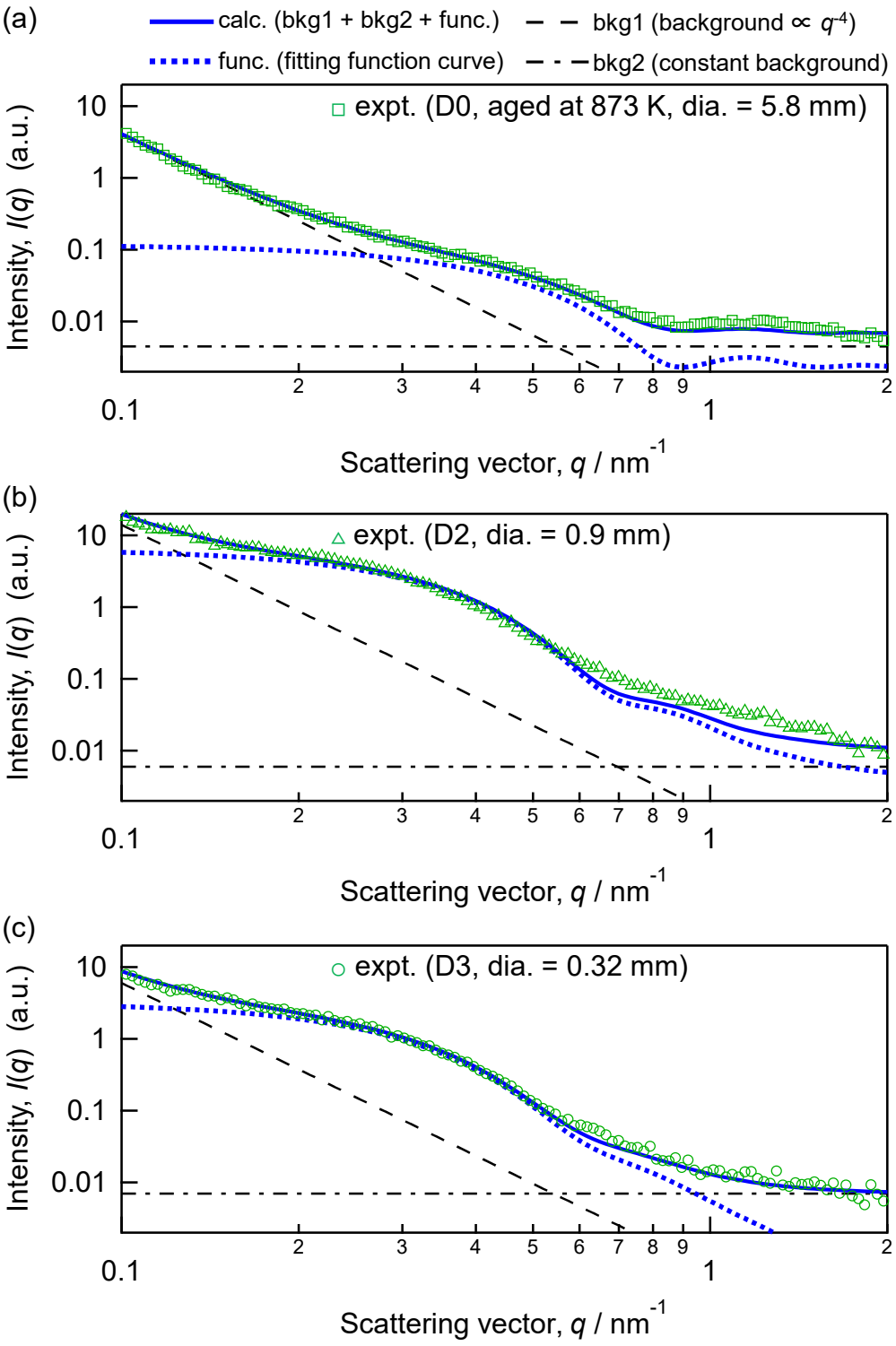

Figure 3.26 Experimental SANS profiles with fitting functions.

(a) D0 aged at 873 K and not drawn.

(b) D2 aged at 873 K followed by wire drawing from 5.8 mm to 0.9 mm.

(c) D3 aged at 873 K followed by wire drawing from 5.8 mm to 0.32 mm.

3.3.5 EXAFS and XANES analysis of Cu-0.53 at% Fe wires

The results of several analytical methods in Sections 3.3.1 through 3.3.4 provide insight into the presence of α-Fe and the changes of Fe concentration distribution. In this section, the local structure of Fe by Fe-K edge XAFS and the existence ratios of the three states, α-Fe, γ-Fe and Cu(Fe), are described and discussed.

Figure 3.27 (a) and (b) show k^2-weighted EXAFS and their Fourier transforms (FT) that corresponds to radial structure function (RSF), respectively. Local environment of Fe in Fe-37 at% Ni (FCC) and α-Fe (BCC) are clearly distinguished by the 2nd and 3rd nearest neighbor (NN) peaks in Figure 3.27 (b). Since both Fe atoms in Cu(Fe) and Fe-37 at% Ni (FCC) are in the FCC environment, it is natural that the RSF are similar to each other as in the case of EXAFS study on dense Cu-Fe powder [35] by Harris *et al*.

Figure 3.28 (a) and (b) show RSF obtained from Cu-Fe wires before and after wire drawing at different aging temperature of 673 K and 873 K, respectively. When the aging temperature is 673 K, the local environment of Fe before and after drawing remains similar to each other, indicating FCC. At an aging temperature of 873 K, the local environment of Fe clearly changed to a BCC-like structure if focusing on two peaks. One peak at r = 0.35 nm is higher in the wire D5 than D0, which corresponds to the 3rd NN of α-Fe. Another peak of interest is at r = 0.44, corresponding to the 4th and 5th NN of α-Fe. This changes in RSF is consistent with the fact that α-Fe was found by synchrotron XRD in the section3.3.1. Furthermore, as described in Section 2.3.4, the change of magnetization have suggested martensitic transformation from γ-Fe to α-Fe. This is consistent with the EXAFS results suggesting an increase of α-Fe from D0 to D5. It can be said that EXAFS is the one of the useful tool to observe martensitic transformation in Cu-Fe alloy, as has been done for Fe-Ni and other alloys [67, 68, 69].

Figure 3.29 shows Fe K-edge XANES of three specimens that correspond to the first 50 eV of the EXAFS which was shown in Figure 3.27. Peak positions were labeled by alphabets, A to H. As in EXAFS, XANES of Fe-37 at% Ni (FCC) and α-Fe (BCC) are clearly distinguishable. Although XANES of Cu-0.53 at% Fe and Fe-37 at% Ni alloys looks similar, they can be meaningfully distinguished by the LCF, as will be described later. Figure 3.29 (b) compares XANES of Fe-37 and 45 at% Ni alloys. Despite the enlarged view in Figure 3.29 (b), two spectra appear to be the same implying little dependence of the XANES on the Ni content. In this study, XANES of Fe-37 at% Ni will be hereafter used as an approximated XANES of γ-Fe.

To study the effect of the aging heat treatment, XAFS of two specimens annealed at 673 K and 873 K for 8 h were measured as shown in Figure 3.30 (a) and (b), respectively. Roughly

speaking, the spectral shapes of two XANES are not markedly different. However, careful inspection finds that the dip between peaks G and H is smaller in the 873 K-treated wire (D0). Figure 3.30 (c) shows other differences observed in the flattened spectra with the wide energy range including EXAFS region. LCF analysis were made to decompose the measured spectra to a few components. Firstly, they were decomposed into two components, i.e., experimental XANES of α-Fe and Cu(Fe). Figure 3.31 (a) and (c) shows the results of the 2-component analysis for 673 and 873 K-annealed Cu-Fe wires. As the residual spectra clearly shows, the results of LCF are rather poor and fail to reproduce the dip between peaks G and H. In order to improve the fitting, the approximated XANES of γ-Fe was added as the 3rd component. As can be seen in Figure 3.31 (b) and (d), the experimental XANES was much better reproduced by the 3-component analysis. This implies that it is meaningful to distinguish the XANES of the two FCC phases, i.e., Cu(Fe) and γ-Fe as separate components for LCF. Figure 3.32 (a) and (b) show the flattened spectra with wide energy range including EXAFS region of each specimen corresponding to Figure 3.31 (b) and (d), respectively. It can be seen that the intensity of the EXAFS region can also be approximately fitted.

According to the equilibrium Fe-Cu phase diagram [36], the solubility of Fe in Cu is 0.18 at% at 873 K and < 0.1 at% at 673 K. Precipitation of Fe is expected to occur by the annealing at 873 and 673 K. They were reported to be both α-Fe and γ-Fe [70, 71]. According to the 3-component analysis, the fraction of Cu(Fe) is 0.30 and 0.07 after aged at 873 and 673 K, respectively. The decrease of the fraction with the annealing temperature is consistent with the trend in the phase diagram.

The amounts of the three Fe species (Cu(Fe), α-Fe and γ-Fe) determined by LCF of XANES were calculated as follows, where the amount of additive Fe is 0.53 at% already determined in chapter 2, while $\mathrm{LCF}_{\mathrm{species}}$ is the existence ratio of each species obtained by LCF of XANES.

$$\begin{aligned} C_{\mathrm{Cu(Fe)}} &= 0.53 \times \mathrm{LCF}_{\mathrm{Cu(Fe)}} \\ C_{\alpha-\mathrm{Fe}} &= 0.53 \times \mathrm{LCF}_{\alpha-\mathrm{Fe}} \\ C_{\gamma-\mathrm{Fe}} &= 0.53 \times \mathrm{LCF}_{\gamma-\mathrm{Fe}} \end{aligned} \qquad \text{Equation (3.8)}$$

Figure 3.33 shows the amount of each species versus the working ratio η. After isothermal aging (η = 0.0), fitting was possible with three components as described above, and after drawing (η ≥ 1.6), $C_{\gamma\text{-Fe}}$ appeared to be extremely low. The decrease in $C_{\gamma\text{-Fe}}$ is considered to be due to plastic deformation, specifically described later.

Figure 3.34 shows the dependence of electrical resistivity on $C_{\mathrm{Cu(Fe)}}$. The ρ_{expt} (same as Table 2.3) is plotted with different colors and marks depending on the isothermal aging temperature.

The black line in Figure 3.34 is ρ_{calcup} which is calculated when $C_{sol} = C_{Cu(Fe)}$ in the equation (2.2) above meaning that Cu(Fe) is considered to be homogeneously distributed. ρ_{calcup} is described as the following equation (3.9), where the experimental constant parameter $\Delta\rho$ is identical to $\Delta\rho$ in the equation (2.2) [72].

$$\rho_{calcup} = \rho_0 + C_{Cu(Fe)} \cdot \Delta\rho \qquad \text{Equation (3.9)}$$

The red line in Figure 3.34 is ρ_{calcdn} which is calculated as the following equation (3.10) known as a typical rule of mixtures, where $V_{Cu(Fe)}$ is the volume fraction of Cu(Fe).

$$\frac{1}{\rho_{calcdn}} = \frac{1 - V_{Cu(Fe)}}{\rho_{Cu}} + \frac{V_{Cu(Fe)}}{\rho_{calcup}} \qquad \text{Equation (3.10)}$$

Electrical resistivity is typically in the range of upper limit ρ_{calcup} and lower limit ρ_{calcdn}, depending on the microstructure of each phase such as the precipitates, matrix and the others. When $V_{Cu(Fe)}$ is assumed to be 0.4, each plot of ρ_{expt} is found to be in the range of them. Hence, the changes of Fe precipitates that can be taken from the Figure 3.34, i.e., the changes by aging and the changes by wire drawing, are discussed below in consideration of several previous studies of dilute Cu-Fe alloys.

The obtained insights for Cu-0.53 at% Fe after aging and before drawing are as follows. It has been confirmed by previous studies using TEM and atom-probe observations that γ-Fe consistent with the Cu matrix [7, 10, 11, 54] is formed during isothermal aging. The transformation of γ-Fe to α-Fe after cooling from aging temperature to room temperature [58] has also been confirmed. The LCF results using XAFS in this study showed that both α-Fe and γ-Fe were present at room temperature after isothermal aging, and that the ratio of α-Fe and γ-Fe depended on the aging temperature. This is consistent with the magnetization measured by the VSM in chapter 2.

The findings by this XAFS study on the changes caused by wire drawing are as follows.

It was assumed by Matsuura *et al*. [73] and confirmed by Sato *et al*. [74] that small γ-Fe precipitates consistent with the matrix phase might be fractured by dislocation migration [58]. The XAFS analysis revealed that the $C_{\gamma\text{-Fe}}$ decreased by the wire drawing, indicating that small γ-Fe precipitates were fragmented by deformation and recognized as Cu(Fe). Furthermore, as η increased from 0 to 1.6, $C_{\alpha\text{-Fe}}$ also increased instead of $C_{\gamma\text{-Fe}}$ decreasing. This can be considered as an evidence of the martensitic transformation from γ-Fe to α-Fe, which is consistent with the increase in magnetization already described in Section 2.3.4.

Although no previous study has quantitatively examined the effect of working ratio η on the change of Fe precipitates, such changes revealed by XAFS in this study are discussed in terms of electrical resistivity as follows. When η was higher than 1.6, $C_{\alpha\text{-Fe}}$ decreased and $C_{Cu(Fe)}$

increased regardless of the isothermal aging temperature, as shown in the Figure 3.33. Since XAFS corresponds to the local environment of Fe, Cu(Fe) is expected to increase near the surface of α-Fe precipitates after wire drawing, considering that interdiffusion at the Cu/Fe interface was observed by 3D-APT. Unlike 3D-APT, XAFS results with the wider field of view are useful to discuss about the change in electrical resistivity, ρ_{expt} plotted in Figure 3.34. As the volume fraction of α-Fe and γ-Fe have relatively little influence on ρ_{expt}, here the correlation only with $C_{Cu(Fe)}$ was investigated as follows. The sample B1 drawn to $\eta = 1.6$ after aging at 673 K showed $\rho_{expt} = 3.5\times10^{-8}$ Ωm. After further drawing, ρ_{expt} of B2~B5 gradually approached to the point E which is marked as dotted square in Figure 3.34. This point E is equal to ρ_{calcup} when Fe atoms as Cu(Fe) are homogeneously distributed in the Cu matrix. Finally, the ρ_{expt} of sample B5 ($\eta = 9.5$) is almost equal to point E. This may be due to finely fragmented Fe precipitates in dilute Cu-Fe alloys [75, 76] as assumed in the early reports by Boltax. Similar behavior was observed after different isothermal aging at 773 K. The sample C1 drawn to $\eta = 1.6$ after aging at 773 K showed $\rho_{expt} = 2.7\times10^{-8}$ Ωm. Then, as η increases to 9, ρexpt becomes higher, and ρ_{expt} of C2~C5 gradually approached to the point E in Figure 3.34 just like ρ_{expt} of B2~B5. While aging temperatures of 673 K and 773 K yielded similar results for ρ_{expt}, the higher isothermal aging temperature of 873 K provided a distinctly different trend. The sample D1 was drawn to $\eta = 1.6$ after aging at 873 K, showing $\rho_{expt} = 3.1\times10^{-8}$ Ωm which is higher than C1. Despite the higher ρ_{expt} of D1 than C1 there is less $C_{Cu(Fe)}$, suggesting that the Cu(Fe) is distributed relatively homogeneously. In addition to this, the increase of ρ_{expt} by wire drawing was less likely to occur. Although ρ_{expt} of D1~D5 gradually approached toward the point E as η increased, ρ_{expt} of D5 ($\eta = 9.5$) was only 65% of that of C5 ($\eta = 9.5$). This means that α-Fe in these samples is unlikely to be transformed to Cu(Fe) by wire drawing, even with a high working ratio of $\eta = 9.5$. This is consistent with the detection of α-Fe by XRD and the confirmation of elongated and connected Fe by TEM & 3D-APT in this study. So, it was found that the α-Fe particles are unlikely to be fragmented by the dislocation migration as guessed by Boltax, when isothermal aging temperature was high enough. It can also be said that in order to prevent the deterioration of ρ_{expt} by wire drawing, the surface of Fe precipitates should designed to be not easily interdiffused. This is an important insight in designing wire materials for industrial use, and will help in selecting process conditions and the kinds or amounts of the third additive element.

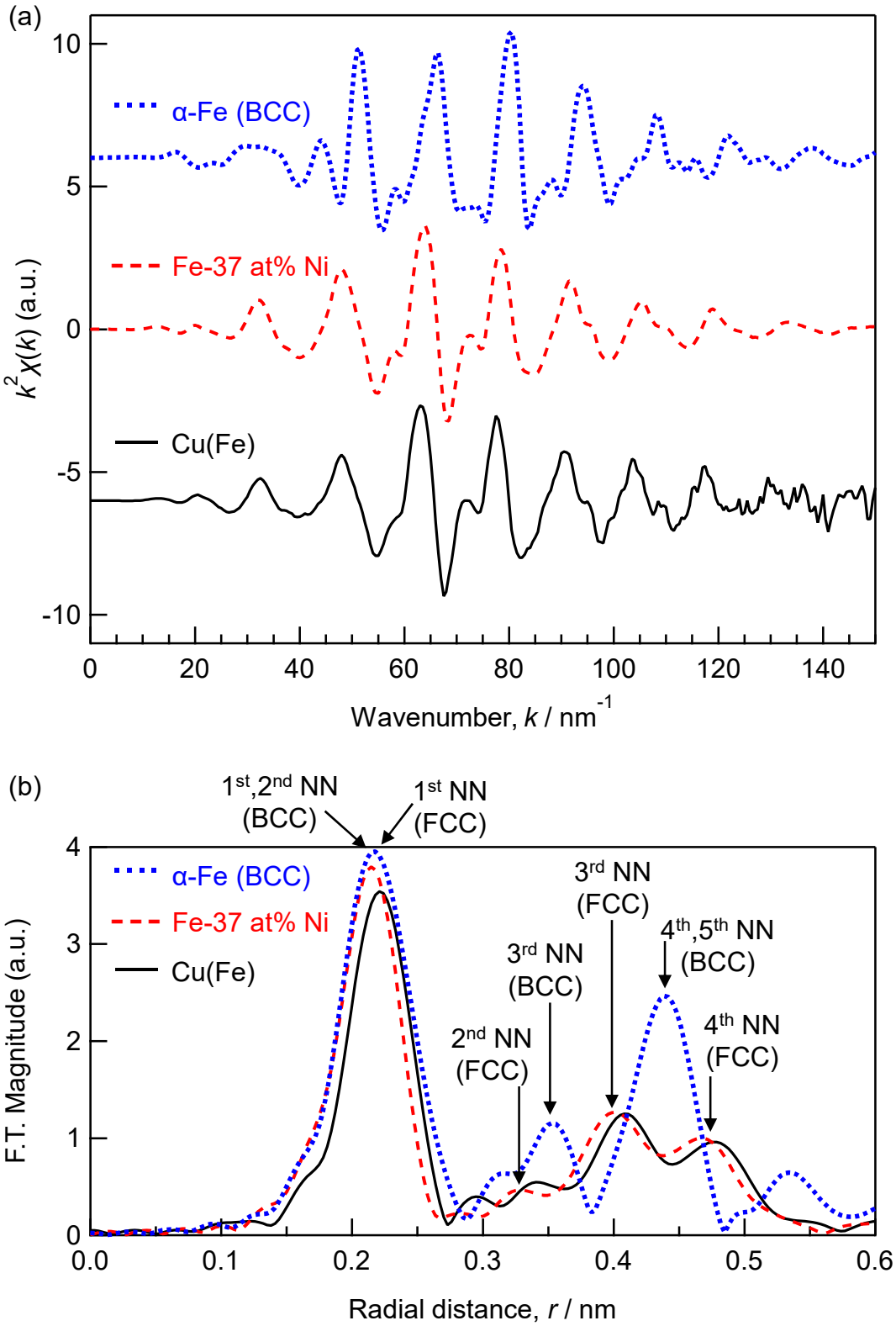

Figure 3.27 Comparison of k^2-weighted EXAFS and their Fourier transforms (F.T.) obtained from three specimens, α-Fe (BCC), Fe-37 at% Ni (FCC) and Cu(Fe).
(a) k^2-weighted EXAFS. (b) Radial Structure Function (RSF).

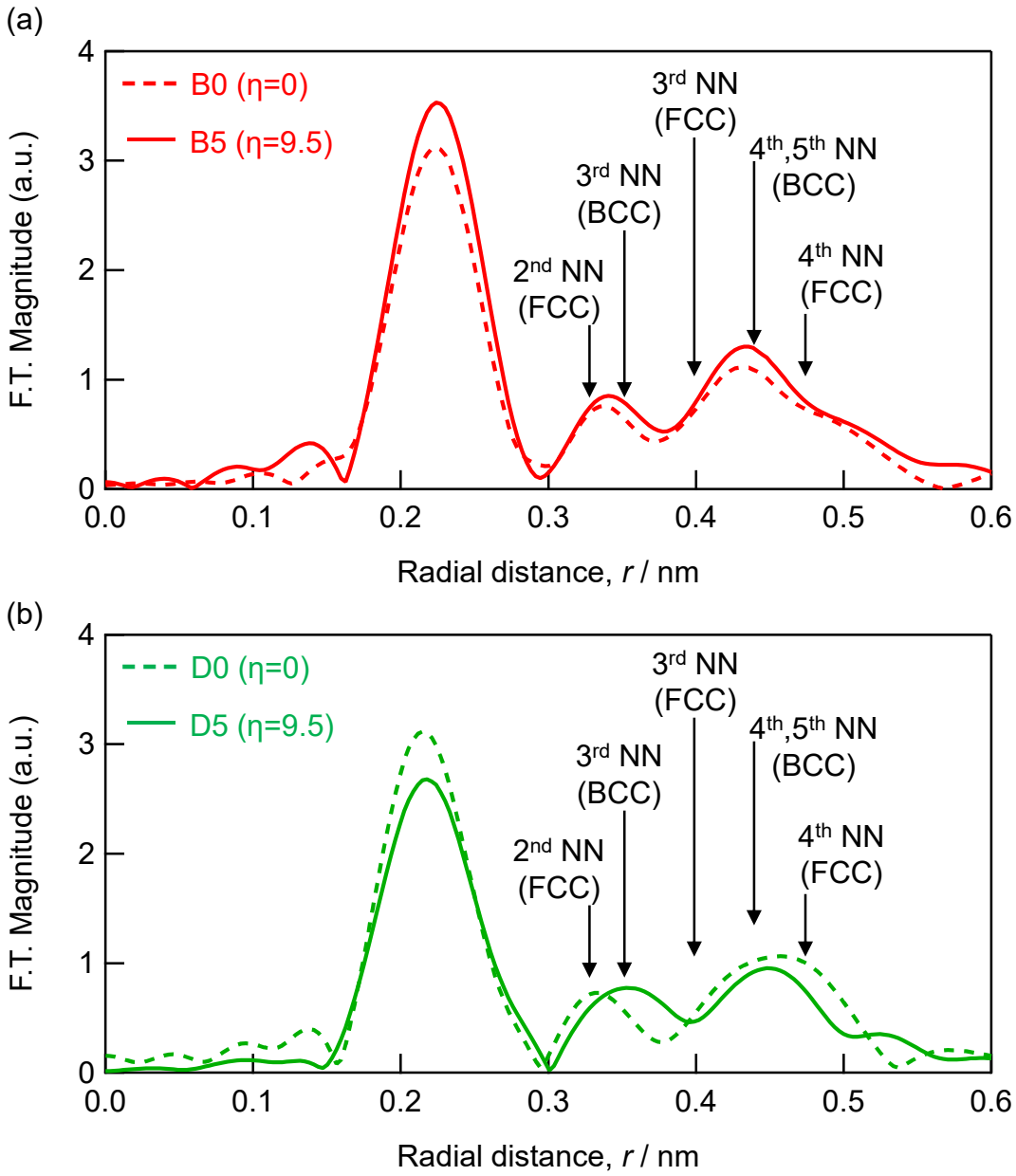

Figure 3.28 RSF obtained from k^2-weighted EXAFS of four kinds of Cu-Fe wires i.e. B0, B5, D0 and D5. Working ratio η is shown on each figure. (a) Comparison of B0 (aged at 673 K) and B5 (drawn to 0.05 mm in a diameter). (b) Comparison of D0 (aged at 873 K) and D5 (drawn to 0.05 mm in a diameter).

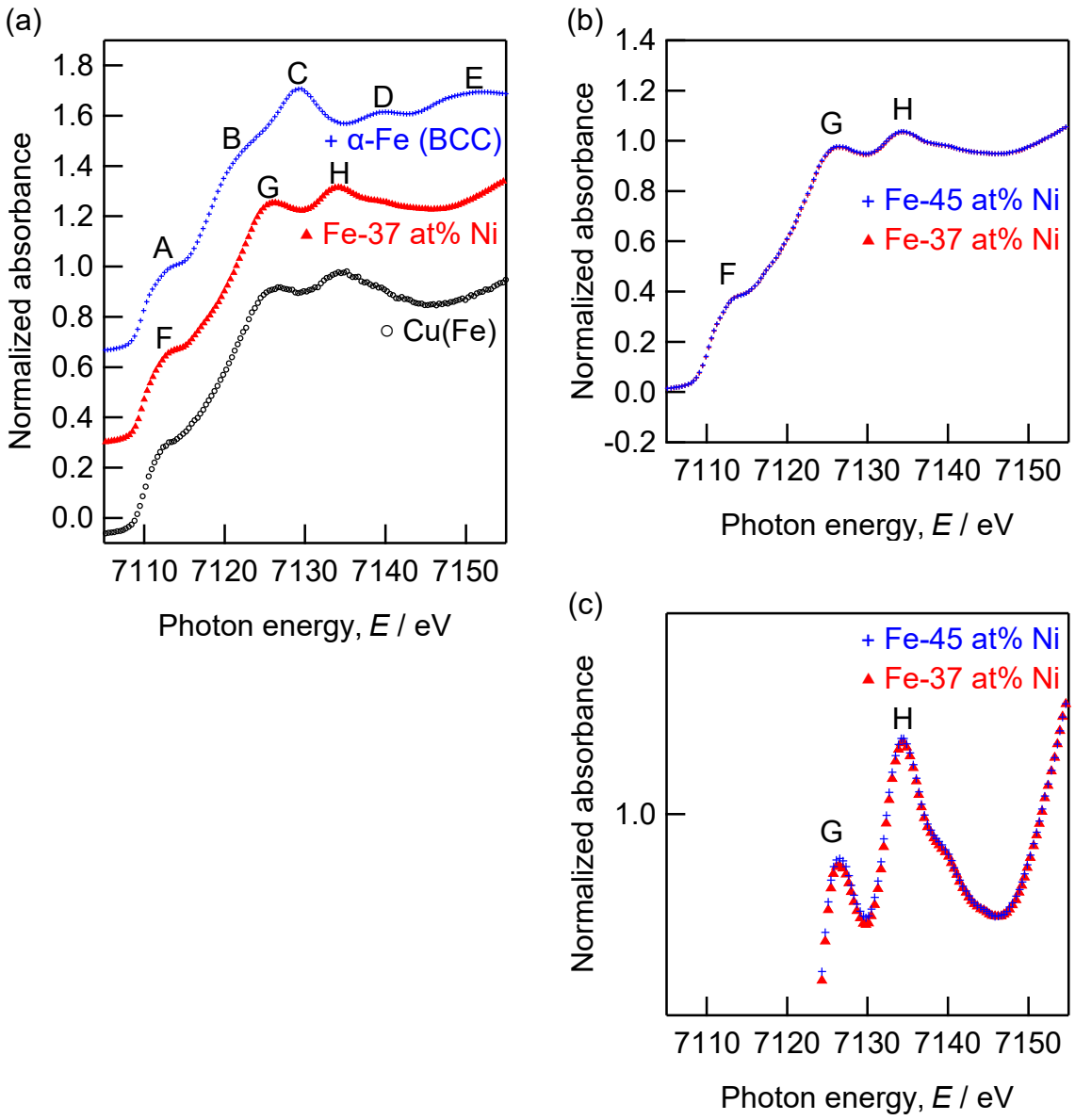

Figure 3.29 Experimental XANES of iron reference samples,
which can be recognized as α-Fe (BCC), γ-Fe (FCC) and Cu(Fe).
(a) Comparison of three specimens, α-Fe (BCC), Fe-37 at% Ni (FCC) and Cu(Fe).
(b) Comparison of two specimens Fe-37 at% Ni and Fe-45 at% Ni as γ-Fe.
(c) Enlarged view of (b), good agreement can be seen between them.

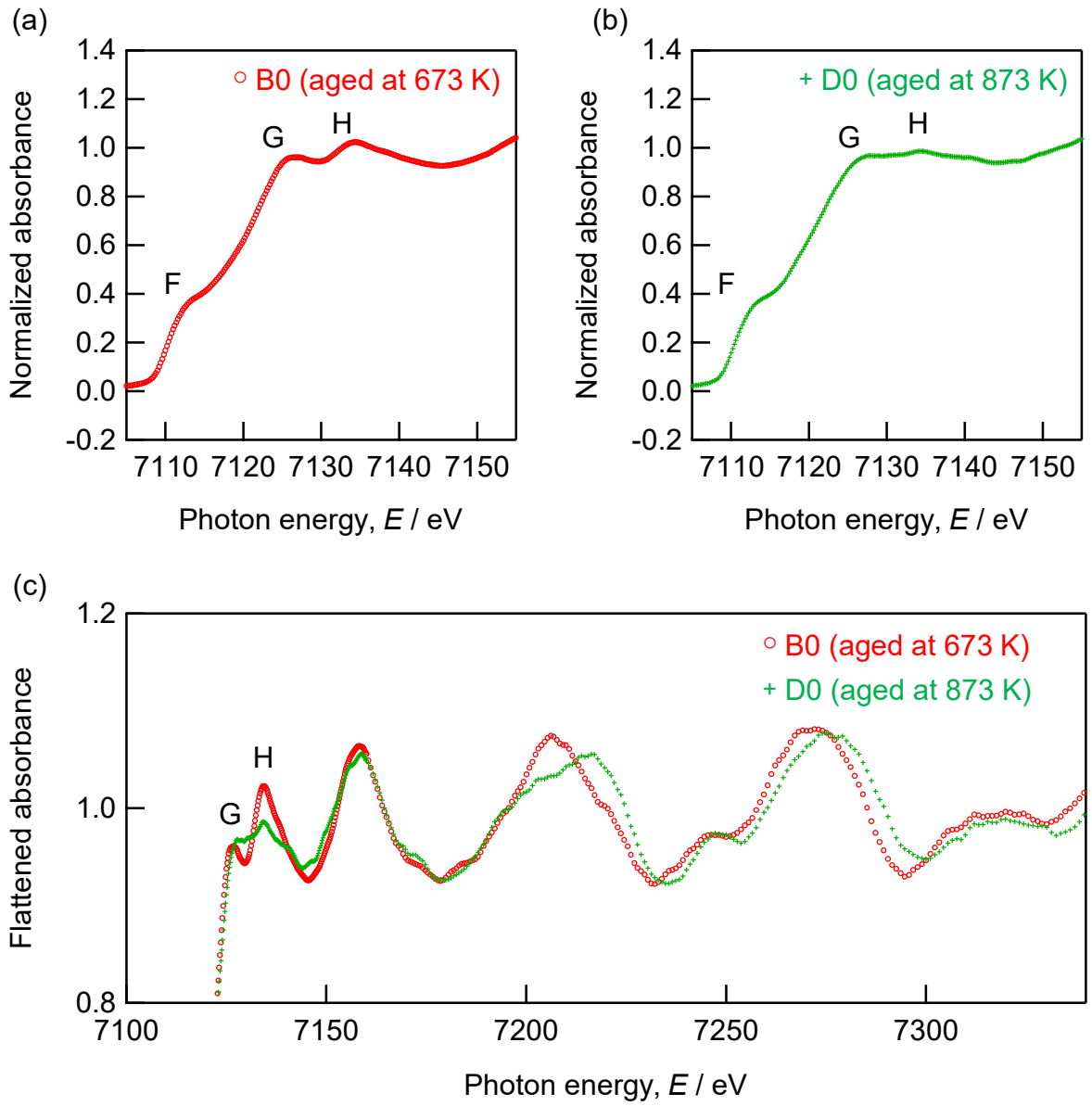

Figure 3.30 Experimental XANES and EXAFS of two specimens in 5.8 mm diameter.

(a) Normalized absorbance of Cu-Fe wire aged at 673 K for 8h.

(b) Normalized absorbance of Cu-Fe wire aged at 873 K for 8h.

(c) Flattened absorbance with wide energy range including EXAFS region.

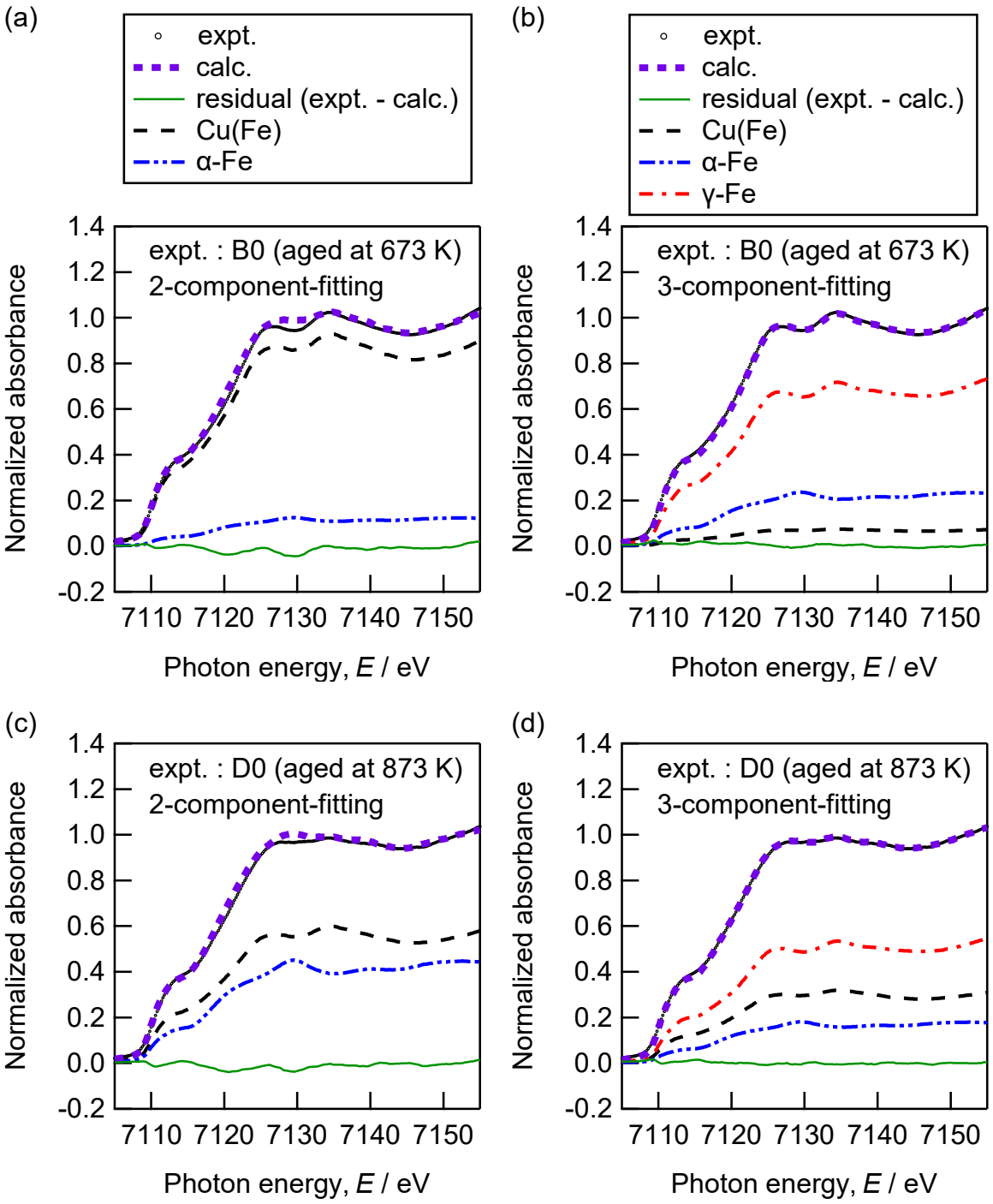

Figure 3.31 Experimental and simulated XANES by LCF analysis.

Simulated spectra are the sum of 2 or 3 components.

(a) Cu-Fe wire B0 (aged at 673 K) with 2 components.

(b) Cu-Fe wire B0 (aged at 673 K) with 3 components.

(c) Cu-Fe wire D0 (aged at 873 K) with 2 components.

(d) Cu-Fe wire D0 (aged at 873 K) with 3 components.

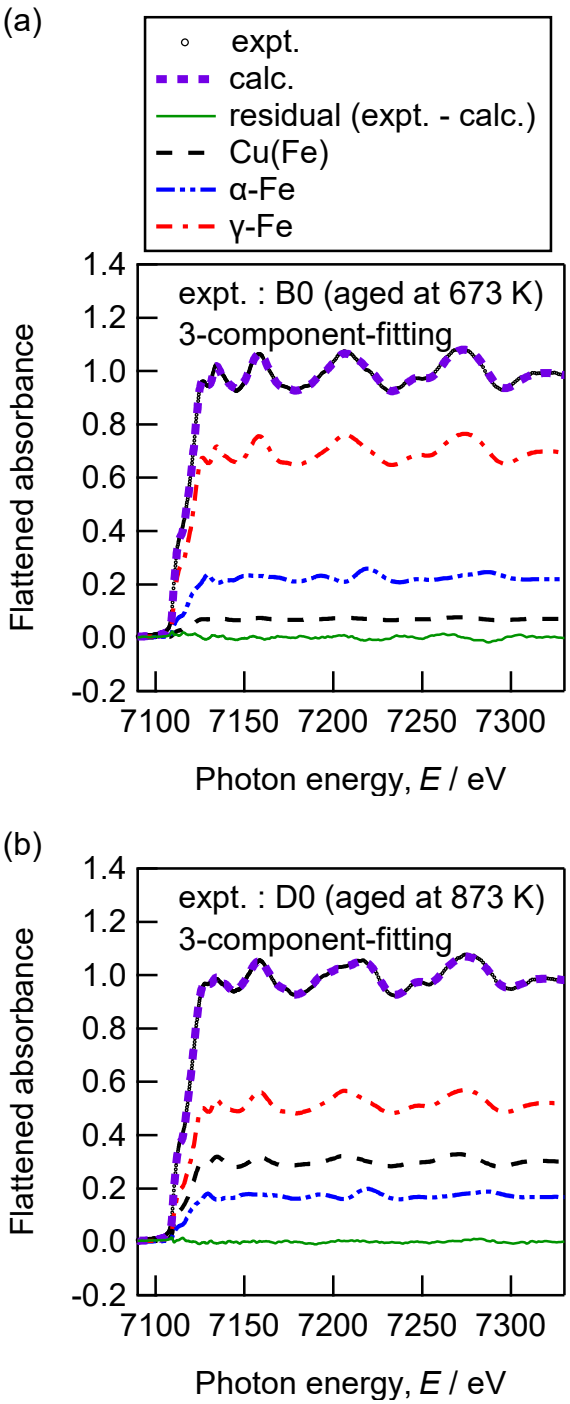

Figure 3.32 Experimental and simulated XANES by LCF analysis.

(a) Fitting result corresponding to Figure 3.31 (b).

(b) Fitting result corresponding to Figure 3.31 (d).

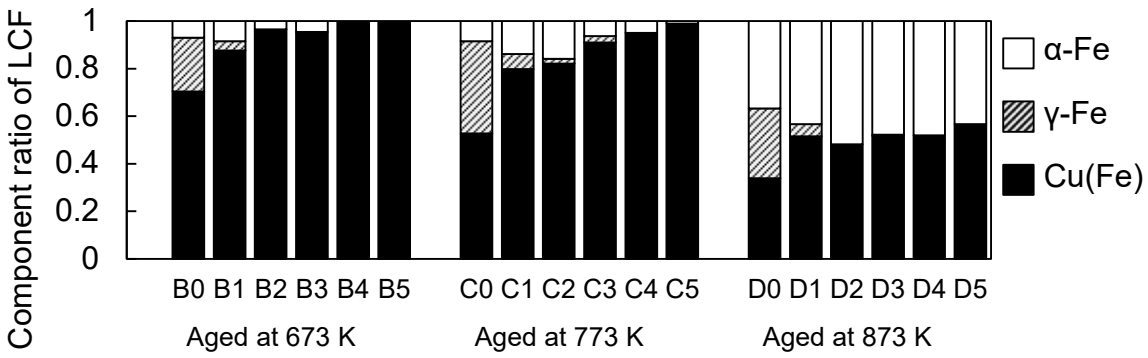

Figure 3.33 Component ratio of LCF by Fe-K XANES analysis, showing the existence ratios of the three states, α-Fe, γ-Fe and Cu(Fe).

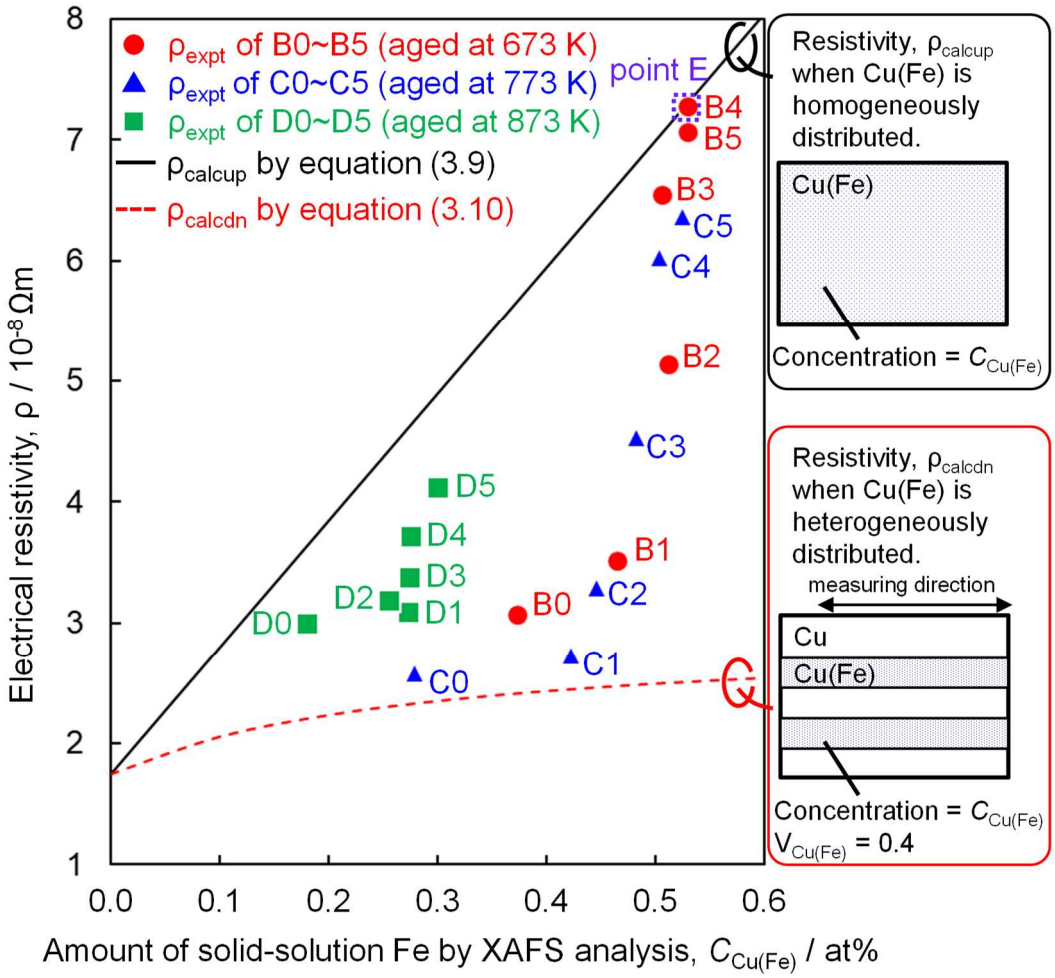

Figure 3.34 Relationship between electrical resistivity and the amount of Cu(Fe).
Each mark (circle, triangle and square) indicates ρ_{expt} by experiment.
The black line shows ρ_{calcup} when Cu(Fe) is homogeneously distributed.
The red line shows ρ_{calcdn} when Cu(Fe) is heterogeneously distributed.

3.4. Summary

Detailed changes of Fe precipitates by wire drawing in Cu-0.53 at% Fe alloys were revealed by a combination of several analytical methods.

First, the residual α-Fe precipitates which were made by aging heat treatment at 873 K and wire drawing were analyzed by conventional analytical methods, XRD and TEM. By using synchrotron X-rays of very high intensity, it was confirmed that a very small amount of α-Fe phase was detected only in the case of a sample with an aging temperature of 873 K. At the same time, it was found that for ultrafine wires of 0.05 mm diameter (working ratio $\eta = 9.5$), the microstrain ε of the Cu matrix makes no difference regardless of the isothermal aging temperature. TEM observation confirmed for the ultrafine wires that Cu grains were elongated parallel to the drawing direction, similar for the two aging temperature conditions, i.e., 773 K and 873 K. Although it was almost impossible to identify Fe precipitates from STEM images due to the large number of dislocations, EDX elemental mapping confirmed that the Fe precipitates were about 20 nm in size. And some Fe particles were suggested to be scattered in a line in the direction of wire drawing.

High sensitivity and high spatial resolution 3D-APT analysis was performed to clarify whether the three-dimensional distribution of Fe atoms is aligned in the drawing direction as estimated by TEM. Focusing on the isoconcentration surface of 4 at% Fe, it was confirmed that Fe atoms are longitudinally distributed along the drawing direction. Connected elongated isoconcentration surfaces were observed when the aging temperature was 873 K, while scattered isoconcentration surfaces were observed when the aging temperature was 773 K. Although α-Fe and γ-Fe cannot be distinguished, these results suggest that Fe precipitates coarsened by aging heat treatment was elongated and partially fractured by wire drawing. This is the first time that fragmentation of Fe precipitates due to wire drawing has been confirmed at the atomic level. Evaluation of the proxigram on the Cu/Fe interface revealed that interdiffusion near the precipitate surface varies by 40 at% Fe concentration at a distance of 2nm from the interface, regardless of the aging temperature.

In contrast to TEM and 3D-APT, SANS with its wide analytical field of view was also performed. The neutron beam was suitable for the analysis of thick materials due to its high transmission capability, which made it possible to collect data for a wide range of wire diameters (5.8~0.32 mm) with the same measurement system. As a result, it was found that the Fe precipitates could be observed in SANS profile and the mean size of the precipitates was not so differ from that obtained by TEM observation.

Fe-K edge XANES and EXAFS were analyzed to reveal the changes in terms of the local structure of Fe. Owing to the wide analytical field of view, the relationship between the electrical resistivity and the existence ratios of the three states, α-Fe, γ-Fe and Cu(Fe), were also investigated. XAFS was obtained regardless of the wire diameter (12.5~0.05 mm). As Cu-0.53 at% Fe wire annealed at 1173 K was found to be FCC structure by EXAFS, it was suitable for the reference sample as substitutional solute in Cu (FCC), namely Cu(Fe). Since XANES of Fe-37 and 45 at% Ni alloys appear to be the same implying little dependence on the Ni content, XANES of Fe-37 at% Ni was found to be suitable as an approximated XANES of γ-Fe in this study. Although BCC and FCC phases were clearly identified, EXAFS did not succeed in identifying Cu(Fe) and γ-Fe phases. Unlike EXAFS, Fe-K XANES of Cu(Fe) and γ-Fe were slightly different. The LCF analysis of XANES showed that inclusion of two components for FCC phases significantly improve the fitting, which implies that XANES of Cu(Fe) and γ-Fe can be meaningfully distinguished by the LCF. Accordingly, the proportion of Fe atoms in the three states, i.e., α-Fe, γ-Fe and Cu(Fe) was quantified.

The result of the LCF analysis of XANES showed good agreement with many previous studies and other measurements in this thesis. The LCF results that γ-Fe decreases and α-Fe increases after low degrees of wire drawing were consistent with martensitic transformation of Fe in dilute Cu-Fe alloys. The change in the amount of α-Fe showed the same trend as the magnetization measurement. The estimated amount of Cu(Fe) and the electrical resistivity were compared. Since XAFS reflects the local structure at the atomic level, the consideration changes depending on whether Cu(Fe) is homogeneously distributed in the matrix or not. Electrical resistivity after isothermal aging suggested that Cu(Fe) was heterogeneous, while it gradually became homogeneous after wire drawing. Specifically, after aging at 673 K, when the wire was drawn from 5.8 mm to 0.05 mm ($\eta = 9.5$ as the working ratio), Cu(Fe) tended to distribute more homogeneously as η increased, resulting in a large increase in the electrical resistivity of this dilute Cu-Fe wire.

While aging temperatures of 673 K and 773 K yielded similar results through XAFS study, the higher isothermal aging temperature of 873 K provided a distinctly different trend. The α-Fe precipitates produced by isothermal aging at 873 K or martensitic transformation were unlikely to decrease by wire drawing up to a high working ratio of $\eta = 9.5$. This is consistent with the existence of α-Fe confirmed by XRD and the elongated Fe concentration distribution by TEM & 3D-APT in this thesis. Therefore, if the isothermal aging temperature is sufficiently high, the fragmentation of α-Fe precipitates by dislocation migration, as proposed by Boltax [68], is unlikely to occur.

While XAFS has been widely applied in a number of fields in materials science and technology, its use for solute atoms in metallic materials has thus far been limited. The reason is probably that the electronic states of simple metals are often overly simplified and considered as free electron-like. XANES are therefore thought to be insensitive to local environment. But as revealed in this study, the structural changes of Fe in FCC and BCC can be clearly distinguished by either XANES or EXAFS. Moreover, two FCC states, Cu(Fe) and γ-Fe can be distinguished by XANES. EXAFS analysis combination with XANES can be useful not only for Cu-Fe binary alloys, but also for the various industrially developed Cu alloys containing multiple elements. Nevertheless, the application of XAFS to precipitate analysis is still limited, and theoretical support as well as experimental data is important. Since first principles methods for reproducing and interpreting XANES have already been established in early 2000s as reviewed by Tanaka *et al*. [77], an additional comparison of experimental spectra with calculation performed by calculating the electronic structure of Fe in Cu is discussed in the following chapter 4.

References

[1] G. Wasserma *et al., Arch. Eisenheuuenw.,* **29**, 310 (1958).

[2] E. Hornbogen and R. C. Glenn, *Trans. Met. Soc. AIME,* **218**, 1064 (1960).

[3] S. R. Goodman *et al., Metall. Trans.,* **4**, 2363 (1973).

[4] E. Hornbogen*, Trans. ASM,* **57**, 120 (1964).

[5] K. Yuge *et al., Mater. Trans.,* **45** (5), 1473 (2004).

[6] A. Seko *et al., Mater. Trans.,* **45** (7), 1978 (2004).

[7] P. J. Othen *et al., Philos. Mag. Lett.,* **64** (6), 383 (1991).

[8] R. Monzen *et al., Philos. Mag. A,* **80** (3), 711 (2000).

[9] A. Deschamps *et al., ISIJ Int.,* **41** (2), 196 (2001).

[10] M. Wada *et al., Acta Metall.,* **36** (2), 333 (1988).

[11] K. Hono *et al., Scr. Mater.,* **22** (6), 881 (1988).

[12] K. Hono *et al., Appl. Surf. Sci.,* **35** (3), 327 (1989).

[13] M. K. Miller *et al., Mater. Charact.,* **44**, 235 (2000).

[14] B. Stumphy *et al., J. Nucl.Mater.,* **453** (1-3), 66 (2014).

[15] K. Osamura *et al., Mater. Trans., JIM*, **34** (4), 305 (1993).

[16] K. Osamura *et al., ISIJ Int.,* **34** (4), 359 (1994).

[17] S. Pizzini *et al., Philos. Mag. Lett.,* **61** (4), 223 (1990).

[18] F. Maury *et al., J. Phys. Condens.,* **6**, 569 (1994).

[19] H. Yaguchi *et al., TETSU TO HAGANE,* **94** (3), 86 (2008).

[20] K. Osamura *et al., Journal de Physique IV,* **3**, 317 (1993).

[21] H. Okuda, *Journal of the Crystallographic Society of Japan*, **41**, 327 (1999).

[22] P. Debye and P. Sherrer*, Physikal. Zeitschrift,* **17**, 271 (1916).

[23] P. Debye and P. Sherrer*, Physikal. Zeitschrift,* **18**, 291 (1917).

[24] A. W. Hull, *Phys. Rev*., **10**, 661 (1917).

[25] K. Osaka *et al., AIP Conference Proceedings,* **2054**, 050008 (2019).

[26] S. Hirosawa *et al., J. JILM,* **64** (11) 542 (2014).

[27] A. Serizawa *et al., Mater. Sci.,* **519-521**, 245 (2006).

[28] S. Esmaeili *et al., Philos. Mag.,* **87** (25), 3797 (2007).

[29] M. Torsæter *et al., J. Appl. Phys*., **108**, 073527 (2010).

[30] B. Gault *et al., J. Phys. Conf. Ser.,* **59**, 132 (2007).

[31] H. Sasaki *et al., J. J. Inst. Copper,* **60** (1), 309 (2021).

[32] M. Ohnuma *et al., Acta Mater.,* **57**, 5571 (2009).

[33] L. Rayleigh*, Proc. Roy. Soc. (London),* **A90** , 219 (1914).

[34] A. Guinier and G. Fournet*, Small-Angle Scattering of X-Rays (Wiley, New York),* (1955).

[35] V. G. Harris *et al., Phys. Rev. B,* **54** (10), 6929 (1996).

[36] G. Salje and M. F. Kniepmeier*, J. Appl. Phys*., **49**, 229 (1978).

[37] B. Ravel and M. Newville*, J. Synchrotron Rad.,* **12**, 537 (2005).

[38] T. Uchiyama *et al., SPring-8/SACLA Res. Rep*., **5** (2), 74 (2017).

[39] P. A. Lee *et al., Rev. Mod. Phys.,* **53**, 769 (1981).

[40] J. H. Hubbell and S. M. Seltzer*, NIST Standard Reference Database,* **126** (Last update: July 2004).

[41] J. H. Hubbell, *Appl. Radiat. Isot.,* **33** (11), 1269 (1982).

[42] S. M. Seltzer, *Radiat. Res*., **136** (2), 147 (1993).

[43] J. B. Nelson and D. P. Riley, *Proc. Phys. Soc.,* **57**, 160 (1945).

[44] W. E. Krull and R. W. Newman*, J. Appl. Cryst*., **3**, 519 (1970).

[45] A. Yousif *et al., Hyperfine Interact*., **156**, 213 (2004).

[46] A. Sutton and W. Hume-Rothery*, Philos. Mag*., **46**, 1295 (1955).

[47] K. Sumiyama *et al., J. Phys. Soc. Jpn.,* **53**, 3160 (1984).

[48] K. Uenishi *et al., Z. Metallkd.,* **83**, 132 (1992).

[49] A. R. Stokes and A. J. C. Wilson, *Proc. Cambridge Philos. Soc.,* **40**, 197 (1944).

[50] A. R. Stokes and A. J. C. Wilson, *Proc. Phys. Soc*., **56**, 174 (1944).

[51] W. H. Hall, *Proc. Phys. Soc*. *A,* **62**, 741 (1949).

[52] G. K. Williamson and W. H. Hall, *Acta Metall*., **1**, 22 (1953).

[53] H. Adachi, *Materia Japan,* **61** (12), 864 (2022).

[54] K. Matsuura *et al., J. Japan Inst. Metals,* **41** (12), 1285 (1977).

[55] J. M. Denney, *Acta Metall.*, **4** (6), 586 (1956).

[56] S. Nishikawa *et al., Seisan-kenkyuu,* **18** (11), 312 (1966).

[57] H. Wendt and R. Wagner, *Acta Metall.,* **30** (8), 1561 (1982).

[58] Y. Watanabe, *Materia Japan*, **34** (7), 905 (1995).

[59] K. E. Easterling and H. M. Miekk-Oja, *Acta Metall.,* **15** (7), 1133 (1967).

[60] K. E. Easterling and G. C. Weatherly, *Acta Metall.,* **17** (7), 845 (1969).

[61] K. E. Easterling and P. R. Swann, *Acta Metall.,* **19** (2), 117 (1971).

[62] N. Ishikawa and A. Sato, *Philos. Mag. A*, **64** (2), 387 (1991).

[63] V. M. H. Lopez and K. Hirano, *J. Mater. Sci.*, **29**, 4802 (1994).

[64] M. Cohen, *Trans. AIME,* **95**, 133 (1939).

[65] R. B. Gorden and M. Cohen*, ASM Symposium on Age Hardening of Metals*, 161 (1940).

[66] C. S. Smith, *Progress in Metal Physics,* **1**, 175 (1949).

[67] K. J. Rutsky and P. Georgopoulos*, Scr. Metall.,* **20** (3), 419 (1986).

[68] T. Girardeau *et al., J. Phys. F: Met. Phys.,* **18**, 575 (1988).

[69] H. Maruyama *et al., JPSJ,* **56** (12), 4377 (1987).

[70] F. Bitter and A. R. Kaufmann, *Phys. Rev*., **56**, 1044 (1939).

[71] J. Reekie *et al., Proc. Phys. Soc. B,* **66**, 1101 (1953).

[72] J. O. Linde, *Ann. D. Phys.,* **407** (2), 219 (1931).

[73] K. Matsuura *et al., Acta Mettall.,* **21** (8), 1033 (1973).

[74] A. Sato *et al., Trans. JIM,* **25** (12), 863 (1984).

[75] A. Boltax, *Trans. Met. Soc. AIME,* **218**, 812 (1960).

[76] A. Boltax, *Trans. Met. Soc. AIME,* **224**, 281 (1962).

[77] I. Tanaka *et al., J. Am. Ceram. Soc.,* **88**, 2013 (2005).

Chapter 4 First principles calculations of XANES

4.1. Introduction

In this chapter, Fe-K edge XANES of Cu-Fe binary alloy is compared with experimental data obtained in the previous chapter 3 by contrasting with theoretical calculations. XANES provides information on local environment of a selected element, in this case iron. Theoretical XANES can be obtained either by the calculation based on the multiple scattering theory [1], and the DFT calculation [2, 3, 4]. They can be used as theoretical fingerprints to interpret the experimental XANES. In this study, we adopted DFT calculations using the WIEN2k package [5] which is an all-electron method with basis-functions of augmented plane-wave + local orbitals. As the same states as those that had been prepared as for the experimental reference spectra as already shown in Figure 3.29 (a), three models, Cu(Fe), γ-Fe and α-Fe models, were constructed. Next, we systematically investigated the extent of the discrepancy between the measured photon energies and the calculated transition energies. The transition energy is expressed as the difference between the excited state and the ground state [6, 7]. In the case of Fe-K edge calculation, excited states are those in which one electron is removed from an Fe-1s orbital.

4.2. Calculation methods

Three models, Cu(Fe), γ-Fe and α-Fe models, were constructed as follows. For Cu(Fe) model, a 32-atom supercell was made by expanding the cubic unit cell of FCC-Cu by 2×2×2, and a Cu atom was replaced by an Fe atom. The atomic positions were fixed with the lattice parameter fixed to twice the experimental lattice parameter of Cu (0.3615 nm). The dependence of the theoretical XANES on the cell-size was examined using a 3×3×3 (108-atom) model. As shown in Figure 4.1, the cell-size dependence was not sensible. We will hereafter use the 2×2×2 (32-atom) model. Calculations were also made for γ-Fe using the 2×2×2 supercell (32-atom) with the experimental lattice parameter extrapolated to room temperature (0.3576 nm) [8] , and α-Fe using the 2×2×2 supercell (16-atom) with experimental lattice parameter (0.2856 nm) [9]. The matrix elements of the electric dipole transition were calculated using XSPEC [10] program included in WIEN2k package, which were used as theoretical XANES. The theoretical transition energy was calculated as the difference in the total energies between the ground and core-hole states. In the case of calculating the core-hole states, one electron was removed from the Fe-1s orbital and another electron was added to the conduction band. The exchange correlation term was GGA-PBE [11], the muffin-tin radius R_{MT} was set to 0.11 nm for both Cu and Fe, and the basis size was determined by $R_{MT}K_{max} = 8.0$. Spin polarization was taken into account assuming ferromagnetic structures for all models.

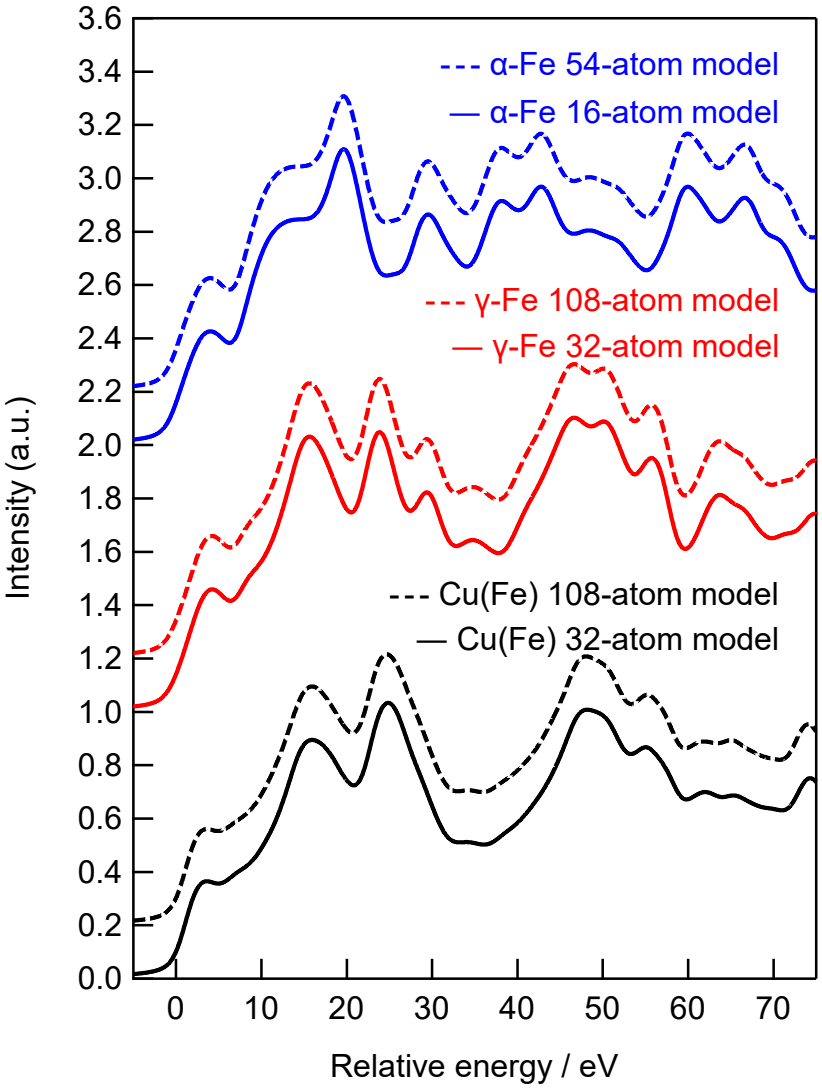

Figure 4.1 The dependence of the theoretical XANES on the cell-size.

4.3. Results and discussion

Figure 4.2 (a) shows theoretical XANES of Cu(Fe), γ-Fe and α-Fe. The theoretical transition energy was found to overestimate the experimental photon energy by 26 eV, i.e., 0.4% of the transition energy. Such an error is within an acceptable range by this type of DFT calculations [12]. By translating the three theoretical spectra by the same amount of 26 eV, they can be compared with the experimental spectra. Peak positions were labeled by alphabets, in the same way as in the experimental XANES. Reasonable agreements for spectral shapes and peak positions between theoretical and experimental can be seen. Like the case of experimental XANES, γ-Fe and α-Fe were clearly distinguished. The theoretical XANES of the two FCC models for Cu(Fe) and γ-Fe were found to be similar. However, the onset of the absorption of Cu(Fe) is slightly lower than that of γ-Fe. In the both of theoretical and experimental spectra shown in Figure 4.2, the onset is similarly lower for Cu(Fe) than the γ-Fe model. The result supports the idea to use two FCC components to get better fitting by the LCF for aging heat treated Cu-Fe specimens, as was attempted in the section 3.3.5.

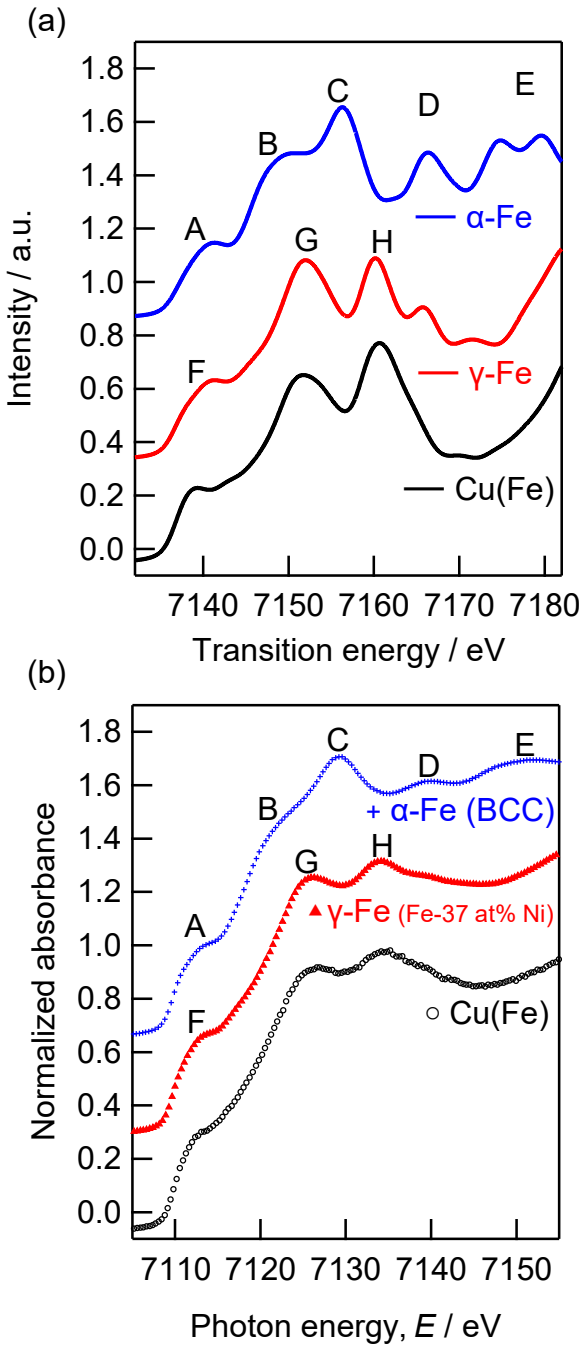

Figure 4.2 Theoretical and experimental XANES of Cu(Fe), γ-Fe and α-Fe.

(a) Theoretical XANES, alphabets are labelled with the same rule as Figure 3.29 (a).

(b) Experimental XANES, which is identical to Figure 3.29 (a).

4.4. Summary

Theoretical XANES were obtained by the DFT calculations to reinforce the interpretation by the LCF which has already performed in Chapter 3 above. They showed reasonable agreement with the experimental XANES and supported the use two FCC components to get better fitting by the LCF for two annealed specimens.

The difference between theoretical XANES and experimental XANES was examined, and it was shown that the transition energy was systematically estimated to be 0.4% larger than the photon energy.

References

[1] J. J. Rehr and R. C. Albers*, Rev. Mod. Phys.,* **72**, 621 (2000).

[2] W. Kohn and L. J. Sham*, Phys. Rev*., **140**, A1133 (1965).

[3] J. C. Slater, *Phys. Rev*., **51**, 840 (1937).

[4] O. K. Andersen, *Phys. Rev. B,* **12**, 3060 (1975).

[5] P. Blaha *et al., J. Chem. Phys.,* **152**, 074101 (2020).

[6] I. Tanaka and T. Mizoguchi*, J. Phys.: Condens. Matter,* **21**, 104201 (2009).

[7] T. Mizoguchi *et al., J. Phys.: Condens. Matter,* **21**, 104204 (2009).

[8] G. Salje and M. F. Kniepmeier*, J. Appl. Phys*., **49**, 229 (1978).

[9] W. P. Davey, *Phys. Rev*., **25**, 753 (1925).

[10] A. Neckel *et al., Microchim. Acta Suppl.,* **6**, 257 (1975).

[11] J. P. Perdew *et al., Phys. Rev. Lett*., **77**, 3865 (1996).

[12] I. Tanaka *et al., J. Am. Ceram. Soc.,* **88**, 2013 (2005).

Chapter 5 Conclusion

In this study, the author investigated the formation of Fe precipitates by aging heat treatment of dilute Cu-Fe alloys, followed by changes in the Fe precipitates and material properties when the alloys subjected to wire drawing.

In Chapter 1, as a background of this study, requirements of fine copper wires, for which demand is currently accelerating, are described, and previous studies on aging precipitation of Cu-Fe alloys since the 1930s are also presented. It was stated that industrial demand for thinner wires made it essential to use alloys with higher strength than pure copper; Cu-Fe alloys could have a large electrical resistivity increase when subjected to the unavoidable wire drawing process when mass-produced. To optimize material and process design, it was necessary to understand the causes of property changes due to wire drawing. Previously, the relationship between the increase in electrical resistivity due to wire drawing and changes in Fe precipitates had not been clarified. In particular, there were only a few studies on the relationship between the amount of solid solution Fe and electrical resistivity, so we undertook this research project to clarify them.

In Chapter 2, Cu-0.53 at% Fe alloy was melt-cast and drawn to ultrafine wire; it was found that the wire drawability was equal to or better than pure copper to the extent that it could be drawn from 12.5 mm to 0.05 mm without being fragmented in the wire drawing process, and higher strength than pure copper was easily obtained. It was also found that the electrical resistivity increased by wire drawing, but the higher the aging temperature, the harder it was to increase the electrical resistivity. The magnetization of the Cu-Fe alloy increased when the diameter was reduced from 5.8 mm to 2.6 mm by wire drawing, suggesting that martensitic transformation from γ-Fe to α-Fe occurs significantly, especially when the aging condition is 8 hours at 873 K. These properties are similar to the trends of cold-worked Cu-Fe alloys reported previously.

In Chapter 3, five analytical methods were attempted and the information obtained from each method was analyzed in a complementary manner. X-ray crystallography and high spatial resolution analysis were performed for the ultrafine wires, 0.05 mm in diameter. Neutron and synchrotron radiation analyses were performed on almost all wires up to 12.5 mm in diameter. XRD measurements using synchrotron radiation as a high intensity X-ray source showed that a small amount of α-Fe was detected after drawing to 0.05 mm only when the aging temperature applied before drawing was 873 K. STEM-EDX showed that the Cu matrix grains were elongated along the drawing direction and that Fe was scattered at aging temperatures of 873 K. 3D-APT revealed that the isoconcentration surfaces of Fe are anisotropically distributed

along the drawing direction. Specifically, in samples where α-Fe was not detected by XRD, the 4 at% Fe isoconcentration surfaces were found to be dotted. On the other hand, in samples where α-Fe was detected by XRD, the 4 at% Fe isoconcentration surfaces were found to be elongated longitudinally and interconnected. Additional analysis was performed by SANS in combination with STEM-EDX, including thicker wires from 5.8 mm to 0.32 mm. The scattered Fe precipitates appeared after isothermal aging at 873 K and were shown to be about 15 nm in diameter. The scattering contrast due to Fe precipitates became stronger after wire drawing, which was reasonable considering the effect of magnetic scattering as a result of martensitic transformation from γ-Fe to α-Fe. XAFS measurements using synchrotron radiation facilities were used to comprehensively analyze the samples from 12.5 mm to 0.05 mm in diameter. Standard spectra of α-Fe, γ-Fe, and substitutional solute, i.e., Cu(Fe), as the three types of Fe present in copper, and spectra obtained from Cu-Fe wires were analyzed. The component ratios were calculated by reproducing the spectra of the Cu-Fe wires by adding the three standard components. The amount of solid solution Fe obtained by multiplying the Cu(Fe) component ratio by the Fe content of 0.53 at% showed the same trend as the increase in electrical resistivity caused by the wire drawing. From these results, it is concluded that the main cause of the increase in electrical resistivity due to wire drawing is the change in Fe precipitates, meaning that the Fe precipitates have partially transformed to Cu substitutable solutes.

In Chapter 4, the theoretical fingerprints of XANES by first principles calculations was investigated. It was confirmed that the calculated spectrum agrees with the experimental spectrum by fingerprint matching. The calculated transition energies were found to be estimated to be 0.4% larger than the measured photon energies.

In this thesis, the author investigated the phenomenon in which a change of Fe precipitates could cause a large increase in the electrical resistivity by wire drawing in dilute Cu-Fe alloys by combining the high spatial resolution laboratory instruments and quantum beam analysis. In addition, the experimental XANES as electronic structure of Fe in Cu was supported by theoretical calculation. Since wire drawing is an essential process for wire manufacturing and electrical resistivity is one of the most important index of electric wire products, understanding the increase in resistivity due to wire drawing is essential for the establishment of fine wire manufacturing technology, which will be in high demand in the future. Until now, only local environmental changes of Fe precipitates have been discussed by macroscopic evaluation of mechanical, electrical, and magnetic properties or by microscopic observation with a narrow field of view, since it was difficult to observe nanometer-size changes with a wide analytical

field of view. And the causal relationship between the amount of substituted solute Fe in Cu and the degree of wire drawing had not been investigated. In this study, in addition to the conventional microscopic observation, the distribution of Fe isoconcentration surface was confirmed at the atomic level by atom probe tomography, which provides three-dimensional information, and the presence of Fe precipitates deformed in the longitudinal direction along the wire drawing direction was confirmed. Using quantum beams, a wide range of wire diameters from a maximum of 12.5 mm to a minimum of 0.05 mm have been successfully analyzed for the size of Fe precipitates and the local structure of Fe atoms. XAFS analysis using synchrotron radiation confirmed that the amount of substitutional solute in the Cu-Fe alloy increased by wire drawing, and the electrical resistivity also increased at that time. Thus, in addition to direct observation with high spatial resolution, XAFS is considered to be effective in understanding the effects of minor additives on physical properties by providing information on atomic bonding with a wide analytical field of view. I believe that the same technique can be applied to understand how the Fe state and the electrical resistivity change when a different manufacturing process is employed, or to understand the mechanism of a large increase in the electrical resistivity by deforming process for other dilute Cu alloys.

Acknowledgements

I would like to express my sincere gratitude to Professor Isao Tanaka for giving me the opportunity to write my doctoral thesis. I would like to sincerely thank you for your involvement in this paper, your patience, guidance, and checking the manuscript.

I would like to express my gratitude to Professors Hiroshi Okuda and Hiroyuki Yasuda for critical reading of the manuscript.

The synchrotron radiation experiments of XRD described in section 3.2.1 were performed at BL19B2 in SPring-8 with the approval of JASRI (Proposal No. 2022A2026).

The neutron experiments of SANS described in section 3.2.4 were performed at the iMATERIA instrument (BL20) of the Materials and Life Science Experimental Facility (MLF) in the J-PARC (Proposal No. 2018AM0028, 2018BM0026). Special thanks to Professor Koizumi and Assistant Professor Maeda for their guidance in sample preparation and measurement methods.

The synchrotron radiation experiments of XAFS described in section 3.2.5 were performed at BL16B2 in SPring-8 with the approval of the Japan Synchrotron Radiation Research Institute, JASRI (Proposal No. 2017B5330, 2018A5330, 2019B5331 and 2020A5330).

The synchrotron radiation experiments of XAFS described in section 3.2.6 were performed at the Sumitomo Electric Beamline (BL16) in the SAGA Light Source (Proposal No. SEI2020B-005, SEI2021B-005 and SEI2022A-005).

It is hereby acknowledged that the analytical data processing of 3D-APT was carried out with the help of Dr. Jogo and Dr. Mayama of Toshiba Nanoanalysis Corporation.

I would like to thank Dr. Tetsuya Kuwabara of Sumitomo Electric Industries, Ltd. Energy and Electronics Materials Laboratory for giving me the opportunity to focus on this research and for providing the materials and discussing the results.

I would like to thank all of my work colleagues, i.e., those belonging to Sumitomo Electric Industries, Ltd. Analysis Technology Research Center, for sharing the workload with me. I would like to thank you again for your consideration, especially from Dr. Atsushi Kimura, the general manager of our center.

Finally, I would like to express my deepest gratitude to my family for their constant support.